UNIVERSITAT DE BARCELONA

Synaptic and non-synaptic propagation of slow waves and their modulation by endogenous electric fields

Beatriz Rebollo González

SYNAPTIC AND NON-SYNAPTIC PROPAGATION OF SLOW WAVES AND THEIR MODULATION BY ENDOGENOUS ELECTRIC FIELDS

Doctoral Thesis by **Beatriz Rebollo González**

PhD Supervisor: María Victoria Sánchez Vives

2017

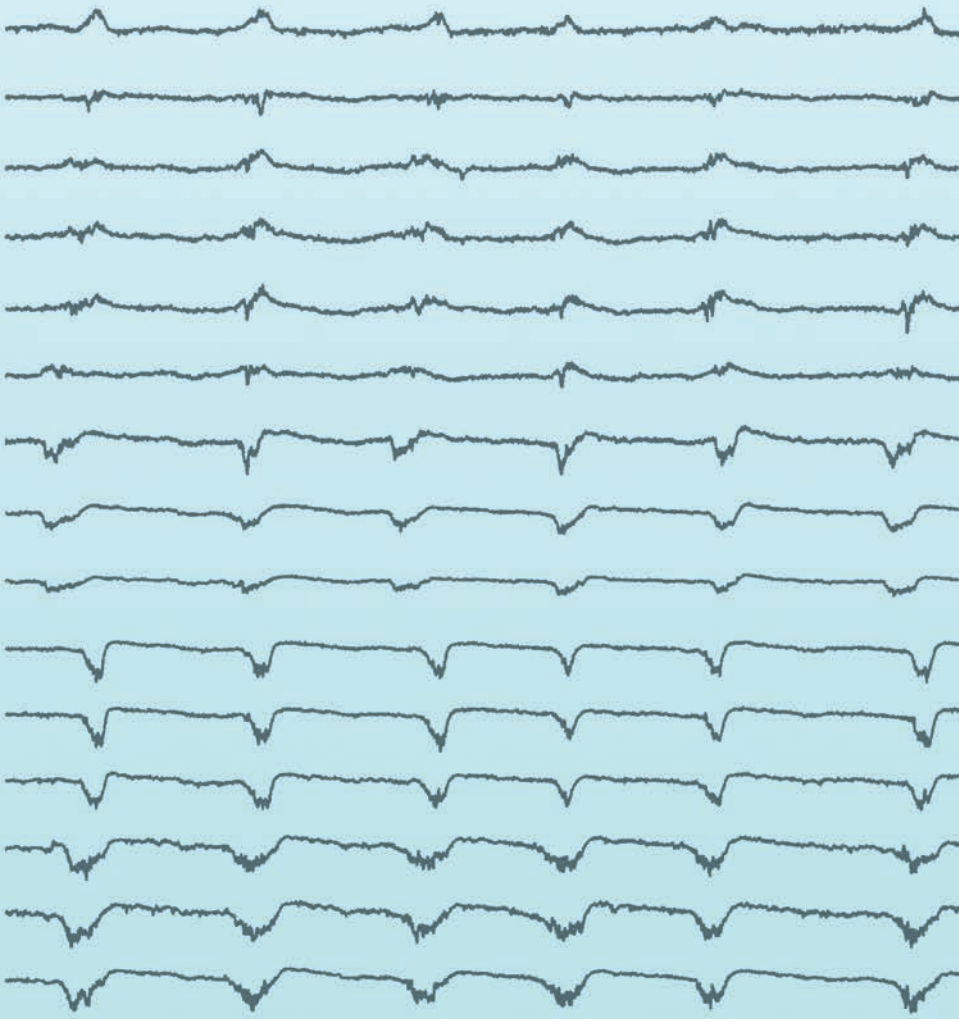

IDIBAPS Institut d'Investigacions Biomèdiques August Pi i Sunyer

UNIVERSITAT DE BARCELONA

UNIVERSITAT DE BARCELONA

INSTITUT D'INVESTIGACIONS BIOMEDIQUES AUGUST PI I SUNYER
UNIVERSITY OF BARCELONA

THESIS FOR DOCTORAL DEGREE IN BIOMEDICINE

Synaptic and non-synaptic propagation of slow waves and their modulation by endogenous electric fields

Author:
Beatriz Rebollo González

Supervisor:
Dra. María V. Sánchez Vives

Systems Neuroscience
Cortical Networks

2017

A mis padres

"They did not know it was impossible so they did it. "

Mark Twain

Abstract

Doctoral degree in Biomedicine

Synaptic and non-synaptic propagation of slow waves and their modulation by endogenous electric fields

by **Beatriz Rebollo González**

During deep sleep stage, neurons synchronize leading to a pattern of activity manifested as slow oscillations (< 1 Hz rhythm). This recurrent synaptic activity is organized eliciting a wave that propagates in the cortex. In this thesis I explore the spatiotemporal dynamics of the slow oscillations in the local cortical network, as well as the electric fields generated by these slow waves. Using an *in vitro* preparation of cortical visual slices, we unraveled that the propagation of slow oscillations is determined by the laminar cortical structure and that the endogenous electric fields that they generate are able to modulate the occurrence of these slow waves.

This work was partially funded by the projects BFU-2011-27094 and BFU-2014-52467-R from Spanish Ministry of Economy and Competitiveness (MINECO); the European Union's Horizon 2020 Research and Innovation Programme under Grant Agreement No. 720270 (HBP SGA1); Slow-Dyn PCIN-2015-162-C02-01 [FLAG ERA]. Beatriz Rebollo González was supported by a predoctoral fellowship from Spanish Ministry of Economy and Competitiveness (FPI, BES-2012-053122).

Publications by the author

1. Mattia D'Andola, **Beatriz Rebollo**, Adenauer G. Casali, Julia F. Weinert, Andrea Pigorini, Rosa Villa, Marcello Massimini and Maria V. Sanchez-Vives. Bistability, causality and complexity in cortical networks: an in vitro perturbational study. *Cerebral Cortex*, 1-10 (2017).

2. Sancristóbal, B., **Rebollo, B.**, Boada, P., Sanchez-Vives, M. V., & Garcia-Ojalvo, J. Collective stochastic coherence in recurrent neuronal networks. *Nature Physics* 12, 881 - 887 (2016).

3. Gemma Gabriel, Xavi Illa, Anton Guimera, **Beatriz Rebollo,** Javier Hernández-Ferrer, Iñigo Martin-Fernandez, Ma. Teresa Martínez, Philippe Godignon, Mavi Sánchez-Vives and Rosa Villa. Chapter title: Carbon nanotubes as suitable interface for improving neural recordings. Book title: Recent Progress in Carbon Nanotube Research / Book 2 (ISBN 980- 953-307-485-1). *INTECH Open Access Publisher*(2013).

4. C. Capone, **B. Rebollo**, A. Muñoz-Céspedes, P. Del Giudice, M. V. Sanchez-Vives, M. Mattia. Slow-waves in cortical slices: how spontaneous activity is shaped by laminar structure. *Under review in Cerebral Cortex*.

5. S.L. Gonzalez Andino*, R. Grave de Peralta Menendez*, **B. Rebollo**, X. Villa and M. V. Sanchez-Vives. Ohmic quasistatic models fail to describe the electrodynamic propagation of slow oscillations in the cortical network. *Under review in Scientific Reports*.

6. **B. Rebollo**, M. Perez-Zabalza, M. Ruiz-Mejias, MV. Sanchez-Vives. Increased high frequency oscillatory activity in the prefrontal cortex in an in vitro model of schizophrenia. *In preparation*.

7. **B. Rebollo** et la., Modulation of Slow Waves by Endogenous Electric Fields: an experimental and theoretical study. *In preparation*.

Acknowledgements

Before getting into scientific details, let me introduce the people who have supported and given me guidance during these years at Sanchez-Vives lab.

First and foremost, I would like to introduce my supervisor Dr. Sanchez Vives. **Mavi**, a scientist woman who has kept on going at the top of science despite the scarce amount of national funding in current times. I specially thank her for giving me the opportunity to pursue a PhD, and for her guidance and advice to open doors for my future career.
I also thank **Vanessa**, the lab manager, who has been the mother of the lab, always taking care of all resources needed, and making sure that everything goes smoothly both on bureaucracy and experimental logistics.

I am very grateful to have worked in collaboration with **Maurizio Mattia** and **Jordi García-Ojalvo** with whom I discovered the computational modeling research. And **Sara González**, thanks to who I expanded my knowledge in physics.

It has been a real pleasure to start and finish the period of my thesis with **Núria**, a person who has always been willing to overcome challenges no matter how difficult they are, what have made her a great researcher.
Marcel and María, I would like to express my gratitude for their immense patience to teach me most of what I know about slow oscillations. Thanks to **Marcel** I have got my experience to keep the brain alive even with bubbles. Thanks to **María** I learned to interpret the Matlab analysis, something completely new to me at that time. The combination of both of them has contributed significantly to my progress as electrophysiologist.
Julia, the efficient German with whom I have shared infinite hours at the *in vitro* set ups, working through sleepless night that transformed the pump sound in the music of a *Brunch Electronik*. Also infinite hours have been shared with **Mattia**, looking for *complexity* within a piece of cortex, although he is a person not at all complex; I have always admired his ability to distinguish between work and friendship. To both of them I would like to thank for teaching me how to use the key that detects Up/Down states.
Thanks to **Pol** for his plots, it was a pleasure to *stochastically* coincide at the lab.

Others who were not so close to my work but equally important at the lab, **Juan** who gave me useful advices at the beginning of my career that I only have got to understand later during my PhD.
Lorena, the second mother in the lab, has always been ready to analyze, and re-analyze data, and assist with informatics issues... she has always been there to appreciate our experimental work.
Patricia, a little girl full of essence, I hold in high regard her broad knowledge and planning capacity.
An unique character was **Thomas**, with his long talks and sense of humor he taught me a lot about how to enjoy science.
The most singular who has passed by the lab: **Diego**, with him I learned a lot about happiness and love; and by the way, talking about happiness and love I need to mention also **Marta Cosín** from the *Cuqui group*. I am grateful for their invitations to *Amasa la Masa*, meetings where together with **María Jesús** and others from the lab we have enjoyed delicious dishes and talks, a great epoch during my PhD.
Another person I would like to thank for sharing her happiness is **Melody**, with her infinite kindness she has managed to comb my craziness.
I also feel really happy to have had the opportunity to share the last year of my thesis with Miguel, Pedro, Almudena, Àlex, Cristina and Álvaro. People with an amazing sense of humor making every day more pleasant. Thanks to all of them for bringing new perspectives to the lab: to **Miguel** and **Pedro** for sharing their valuable expertise as postdocs, to **Almudena** and **Àlex** for their fresh inquietudes. Thanks to **Cristina** for improving our English. And special thanks to **Álvaro** for making much more easier the ending of my thesis analyzing huge amount of data keeping the good mood.

Fuera del lab ha estado Barcelona, una ciudad que no para si te rodeas de las personas adecuadas. Personas como **Itsaso**, icono del bien hacer vasco, quiero darle las gracias por el diseño de la portada, y sobre todo por haber estado siempre pendiente de si disfrutaba el momento. Personas como **Marta**, de un valor incalculable, gracias por haber construido un hogar donde sentirme en paz durante las distintas fases de la tesis.

Cáceres ha resultado el lugar perfecto de desconexión donde familiares y amigas, me han dado oxígeno para seguir adelante. A todos ellos quiero agradecerles por encontrar siempre un momento entre mis efímeras visitas para verme y ponernos al día mientras disfrutábamos de la buena

gastronomía extremeña. Dentro de este maravilloso grupo se incluyen **mis padres**, a quienes quiero agradecer por ayudarme a descubrir mi vocación por la ciencia, por respetar mi decisión de querer avanzar en mi carrera aunque eso suponga seguir lejos, por estar siempre dispuestos a un encuentro en Madrid con obra de teatro y gin-tonics. Son simplemente geniales.

Finalmente, a pessoa mais próxima a esta aventura tem sido **Marco**, que, apesar da distância conseguiu repor minhas energias e me guiar para manter o curso em uma viagem que acaba de começar.

Thanks to all! Gracias a todos! Obrigado!

Contents

List of Figures

List of Abbreviations

ACSF	**A**rtificial **C**erebro-**S**pinal **F**luid
AHP	**A**fter**h**yper**p**olarization
BMI	**B**icuculline **M**ethiodide
CV	**C**oefficient of **V**ariation
CSD	**C**urrent **S**ource **D**ensity
DC	**D**irect **C**urrent
EEG	**E**lectr**e**ncephalo**g**rams
EF	**E**lectric **F**ield
EPS	**E**rly **P**ropagation **S**trip
EPSP	**E**xcitatory **P**ost**s**ynaptic **P**otential
GABA	**G**amma-**A**mino**b**utyric **Acid**
IG	**I**nfra**g**ranular
LFP	**L**ocal **F**ield **P**otential
MEG	**M**agneto**e**ncephalo**g**ram
MUA	**M**ulti **U**nit **A**ctivity
NMDA	**N**-**M**ethyl-**D**-**A**spartate
ND	**N**ormalized **D**ifference
PC	**P**eak **C**ompression
PFC	**Pref**rontal **C**ortex
PLV	**P**hase **L**ocking **V**alue
REM	**R**apid **E**ye **M**ovement
SE	**S**tandard**E**rror
SG	**S**upra**g**ranular
SO	**S**low **O**scillations
TTX	**Te**trodoto**x**in

Chapter 1

Introduction

The cerebral cortex is organized in complex circuits of neurons strongly interconnected in a conductive medium. During deep sleep stage, this neuronal connectivity generates recurrent synchronized synaptic activity leading to transition states where periods of activity are interspersed with periods of silence. This stereotyped pattern of alternate states is manifested as slow oscillations (SO), <1 Hz rhythm that dominates the cortical network during slow wave sleep (Steriade et al., 1993b) becoming important for memory consolidation (Marshall et al., 2006), plasticity (Reig et al., 2006; Reig and Sanchez-Vives, 2007) and metabolic homeostasis (Xie et al., 2013). The spatiotemporal dynamic of the SO is more complex than the simultaneous activation of neurons in a local network. The SO travels with a pattern of propagation in the cortical network, with a preference in the anterior to posterior direction (Massimini et al., 2004; Ruiz-Mejias et al., 2011).
This oscillatory rhythm, which can be observed at single neuronal level and at the population level, generates extracellular fields that are prominent enough to be measured extracellularly on the conductive medium (local field potentials, LFP) or even from the skull surface (electroencephalograms, EEG). Many excellent studies have raised awareness of the mechanisms involved in these extracellular signals generated by neuronal populations (Kajikawa and Schroeder, 2011; Buzsáki et al., 2012; Herreras, 2016; Teleńczuk et al., 2017). Moreover, in the last years it has been proved how the electric fields (EFs) generated by neuronal activity, in turn, induce changes in such activity of neurons (Fröhlich and McCormick, 2010; Anastassiou et al., 2011). In other words, the electric environment generated by neuronal activity has a feedback effect on the synaptic activity. In this manner, exogenous electric fields used in non-invasive brain stimulation provide a broad scope of therapeutic applications by modulating brain activity.

In this thesis, I will explore how the synaptic and non-synaptic components modulate each other during the propagation of SO. For this purpose, I will describe the propagation pattern of SO across the cerebral cortex; then I will investigate the endogenous EFs generated by slow waves dissecting it from the synaptic components to further investigate the modulation that they may induce on the cortical SO.

1.1 The slow oscillation: a rhythmic pattern

Interconnected neuronal networks within the brain have the capacity to maintain and process information, leading to different temporal dynamics which vary as a function of brain states. A clear example of this phenomenon appears during non-REM sleep, an unconscious state period during which different rhythms such as spindles (7-14 Hz) arise during the early state of non-REM sleep, and delta (1-4Hz) and SO (<1 Hz) during later stages.

The SO occurring during slow wave sleep represents one of the intrinsic dynamics of the brain network (Sanchez-Vives and Mattia, 2014). Generated and maintained by neuronal activity synchronization, SO consists in a pattern of recurrent activity in which active periods of neural activity (Up states) intersperse with relative silence (Down states). Such synchronized transitions were first described in striatum (Wilson and Groves, 1981) to later be characterized in the cortex and thalamus (Steriade et al., 1993b,a). Pioneer studies in anesthetized cats have shown that SO are associated with spindle and delta rhythms in the corticothalmocortical network. While spindles are generated in the thalamus, independently of the slow rhythms, delta frequency appears to be associated with the SO and is generated in both thalamus and cortex (Steriade et al., 1993c).
Moreover, SO elicits fast oscillatory rhythms during Up states, similar to those observed during awake states (Steriade et al., 1996; Destexhe et al., 1999; Hasenstaub et al., 2005; Compte et al., 2008). The presence of these fast rhythms might induce synaptic plasticity by increasing the number of connections in the cortex, and therefore suggest an important role in memory consolidation (Marshall et al., 2006). On the other hand, synchronous silences during Down states have been associated with beneficial effects in preventing cellular damage and maintaining cellular processes (Vyazovskiy and Harris,

2013).

1.1.1 How does the slow oscillation emerge?

There has been a great interest in understanding the mechanisms that drive SO and their functional outcomes (Sanchez-Vives and McCormick, 2000; Timofeev et al., 2000; Bazhenov et al., 2002; Volgushev et al., 2006; Neske, 2015). Although some SO features remain unexplored, many network and cellular mechanisms have already been established.

Regarding network mechanisms, already in 1993 Steriade and collaborators described how the SO emerges as a local cortical phenomenon which results from the orchestration of excitatory and inhibitory components. With experiments performed under thalamic lesions they revealed the cortical origin of SO. Later studies proved how such slow oscillatory pattern can be spontaneously sustained in limited circuits for long periods of time (Fig. 1.1), allowing a better exploration of the cellular and network mechanistic details involved (Sanchez-Vives and McCormick, 2000; Timofeev et al., 2000). However, certain controversy has arisen about the contribution of the thalamus in the origin of SO, which through its inputs to layer 4 might influence the initiation of slow wave activity (David et al., 2013; Fiáth et al., 2016). Recent studies justified the thalamocortical circuit as a unique functional network where the thalamus also generates the SO (Crunelli and Hughes, 2010; Crunelli et al., 2015).

Regarding cellular mechanisms, experiments in cortical slices (Sanchez-Vives and McCormick, 2000) or deafferented cortical slabs (Timofeev et al., 2000) disclosed how the SO emerges as a cortical network phenomenon where most neurons are involved. Excitatory pyramidal neurons seem to be responsible for the electrical synchronization in cortical networks (Steriade et al., 1993b). This synchronization persists thanks to the synaptic excitation/inhibition balance which maintains active states over hundreds of milliseconds (Compte et al., 2009; Neske, 2015). Excitation at infragranular (IG) layers (see *"Propagation of slow oscillations within a cortical structure"* section) causes the onset of Up states while K^+ currents lead to their offset (Sanchez-Vives and McCormick, 2000; Compte et al., 2003). Recently, a combination of voltage-sensitive dye with extracellular multielectrode recordings allowed specifying the temporal

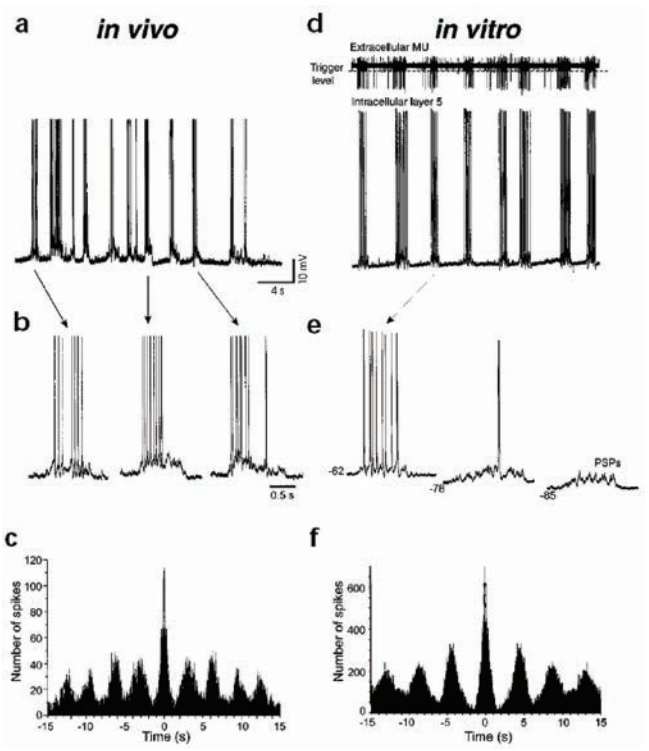

FIGURE 1.1: **SO *in vivo* and *in vitro*** A. Intracellular recording showing depolarization and hyperoplarization of a single neuron in the anesthetized cat. B. Depolarizations examples from A. C. Autocorrelograms of the intracellular recordings representing the periodicity of the oscillation. D-F. Same as A-C in a cortical ferret slice. (D, top) extracellular multiunit-activity. Reproduced from *Nature Neuroscience* (Sanchez-Vives and McCormick, 2000).

spike sequences during SO, revealing a larger contribution of inhibitory cells during Up states than during Down states on the barrel cortex of anesthetized rats (Reyes-Puerta et al., 2016). Besides the neural components, it has been proposed that astrocytes can also be involved in Up state generation by controlling extracellular glutamate in the cortical network (Poskanzer and Yuste, 2011).

At the molecular level, a role of persistent Na^+ currents and N-Methyl-D-Aspartate (NMDA)-mediated excitatory postsynaptic potential (EPSP) have been suggested in the initiation of active states (Steriade et al.,

1993b; Sanchez-Vives and McCormick, 2000). Likewise Ca^{+}-dependent K^{+} currents on the long lasting hyperpolarization seem to be involved in the Up states offset (Steriade et al., 1993b; Compte et al., 2003). These assumptions were reinforced in the slab studies (Timofeev et al., 2000) and slice preparations, where the blockade of non-NMDA glutamatergic receptors abolished SO occurrence, and slow afterhyperpolarization (AHP) reversal potentials suggested an increase in K^{+} conductances (Sanchez-Vives and McCormick, 2000). Moreover, blockade of $GABA_A$ led to shorter Up states with increased AHP, concurring with the proposed mechanisms of K^{+} channels as the candidates for Up state termination (Sanchez-Vives et al., 2010).

1.1.2 Slow oscillations within the cortical structure

A large number of studies have focused on the anatomical organization of neural networks in an attempt to infer functions from structures (Thomson and Lamy, 2007; Stetter et al., 2013; Markram et al., 2015; Pielecka-Fortuna et al., 2015; Lee et al., 2016).
Regarding the SO previously described, recent work on mouse prefrontal cortex (PFC) slices postulates that intrinsic properties of neurons, which are critical to generate delta oscillatory rhythms, occasionally synchronize small cluster of neurons; and this synchronization arises due to the network structure that tends to connect proximal neurons (Blaeser et al., 2017).
In addition, slow waves have been described as traveling waves within the whole brain (Massimini et al., 2004; Ruiz-Mejias et al., 2011; Stroh et al., 2013). In anesthetized and sleeping humans and mice, SO can be originated at any cortical area and propagate in any direction, however there is preference to be originated in anterior regions to propagate to posterior areas.
It is thus of interest to study to what extent the network structure determines the origin and propagation of SO.

The neocortex is shaped by columnar and laminar structures that arise due to the anatomical and physiological arrangement of thousands of neurons, a layout that is conserved across different species. Many neuronal classifications can be done based on morphology, electrophysiological properties, protein expression and connectivity (McCormick et al., 1985; Douglas and Martin, 2004; Thomson and Lamy, 2007; Ascoli et al., 2008; Markram et al., 2015). Briefly, the massive cortical circuitry configuration can be simplified in

two main populations of neurons identified as pyramidal (excitatory) and interneurons (inhibitory) neurons. Those are distributed heterogeneously within six layers (supragranular, SG: layer 1-3; granular: layer 4; IG: layer 5-6) that result from the neuronal migration during development (Arion et al., 2007). Under this structure neurons communicate through vertical and horizontal connections in the cortex (Lorente de Nó, 1934; Cajal, 1952; Bannister, 2005).

In a generalized view of the neocortical circuit, pyramidal cells mainly conform the excitatory flow between layers: starting within layer 4 which receives input from the thalamus to further communicate with layer 2/3; then layer 2/3 projects to layer 5, which projects to layer 6, and has a feedback connection to layer 2/3. This feedback loop between layer 2/3 and layer 5 seems to overcome the inhibition that superficial layers may cause to the cortex. At the same time, layer 6 returns the information to layer 4 closing the loop (Fig. 1.2). Also, intralaminar excitatory communication is present within layer 2/3 and layer 5, being stronger in the latter (Douglas and Martin, 2004; Thomson and Lamy, 2007; Wester and Contreras, 2012).

Whereas excitatory neurons establish most of their connections between layers; inhibitory neurons mainly form synapses within their local layer (Douglas and Martin, 2004; Thomson and Lamy, 2007). Regarding inhibitory circuitry, layer 1 which is composed primarily of interneurons together with apical dendrites and axon terminals, seems to confine the communication between neurons. This layer seizes feedback projections from other areas as well as receives subcortical inputs (Douglas and Martin, 2004). To the greatest extent, inhibitory circuits within the entire cortex regulate excitatory circuits, although recent studies point to a direct role of inhibition in contributing to functional networks (Ascoli et al., 2008; Maffei, 2017).

Considering the previously described massively interconnected wiring network, many studies have explored how such cortical structure takes part on the origin and spreading of SO (Sanchez-Vives and McCormick, 2000; Wester and Contreras, 2012; Beltramo et al., 2013; Reyes-Puerta et al., 2016). A recent *in vivo* study (Fiáth et al., 2016) reported the contribution of different layers on this rhythmic activity. Briefly, the authors explored the spatial distribution of synaptic/transmembrane currents and spiking activity along the laminar cortex during SO. As a result, current source density

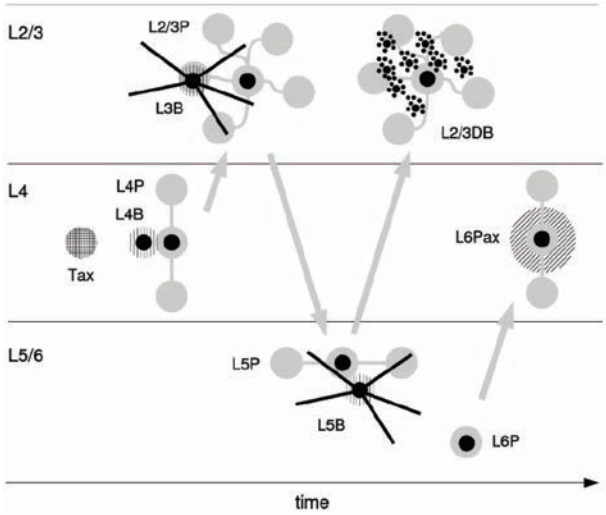

FIGURE 1.2: **Laminar-temporal interactions between main neurons in the cortex** Time towards the right displaying 5 consecutive synaptic crossing. Gray circles, pyramidal cells. Black circles, interneurons. P: pyramidal cells. B: basket cells. Tax: thalamic afferents. L6Pax: Layer 6 pyramidal arbors projecting to layer 4. Reproduced from *Annual Review of Neuroscience* (Douglas and Martin, 2004).

(CSD) analysis revealed the longer source on superficial layers, while a sink appeared in the middle layers during Up states. Layer 4 displayed the higher depolarization on LFP recording while the multiunit activity (MUA) was maximal at layer 5, exhibiting more frequent firing at the onset of Up states, and suggesting a possible initiating role of layer 4 and a major contribution of layer 5 on Up state generation (Fiáth et al., 2016).

Regarding layer 2/3 the probability of connection between neurons is higher if they allocate a common input, nevertheless connectivity in this layer is weaker than in layer 5 in cortical slice preparations (Wester and Contreras, 2012). It has been proved how layer 5, which communicates columns with larger EPSPs than layer 2/3 (Douglas and Martin, 2004), resulted to be more efficient to transfer excitation to other nearby cells under optogenetic activation of pyramidal cells in *in vivo* mice (Beltramo et al., 2013); what is more, layer 5 that depolarizes layer 2/3 during SO propagation, also receives feedback propagation from layer 2/3 to later spread the activity within the cortical columns (Wester and Contreras, 2012). In addition, simultaneous

recordings performed with voltage sensitive dye imaging and multielectrodes showed shorter latencies between spike firing and Up state onset at IG layer than at SG layers, confirming the upward propagation of SO from deep to superficial layers (Sanchez-Vives and McCormick, 2000; Reyes-Puerta et al., 2016). Thus, once the activity is recruited, the propagation occurs radially and homogeneously from deep to superficial layers without preference for the direction (Reyes-Puerta et al., 2016).
In spite of this combined neural activity between IG and SG layers, which can induce spontaneous transmitter release in any neuron leading to depolarized states (Chauvette et al., 2010), the large amount of synapses arriving to layer 5, as well as the presence of a subtype of pyramidal cells (low-frequency bursting) in this layer which might drive the Up states onsets (Lőrincz et al., 2015), indicate that layer 5 mediates transitions from Down to Up states. Moreover, activity within layer 5 is able to hold and spread horizontally the cortical rhythm without the contribution of layer 2/3 (Sanchez-Vives and McCormick, 2000; Wester and Contreras, 2012). Hence, a large amount of evidence points to layer 5 as crucial for the generation and propagation of SO (Sanchez-Vives and McCormick, 2000; Wester and Contreras, 2012; Beltramo et al., 2013; Fiáth et al., 2016; Reyes-Puerta et al., 2016; Blaeser et al., 2017).

Overall, it seems that SO start in layer 5 and spread radially to superficial layers. The feedback projections from superficial layers to deep layers, together with the horizontal projection within layer 5 drive the propagation across columns in the cortical network (Sakata and Harris, 2009; Okun and Lampl, 2008). However, it has not yet been studied to what extent the spatiotemporal pattern of the SO is determined by the cortical structure, and how the global excitability of the neuronal population can modulate its spatiotemporal dynamics.

1.2 From synaptic activity to electric fields

Synaptic activity is considered the most important component for a dynamic interaction between neural networks. However, the electrical phenomenon that arises when different charges move across neuronal membranes generating currents should not be dismissed. EEG measurements at the scalp surface indicate that synaptic and electric fields (EFs) coexist in neural

tissue, and what is more they propagate within it (Buzsáki et al., 2012). Thus, synapses, together with other active mechanisms, contribute to extracellular electric currents that, when superimposed at a specific position, generate field potentials (Kajikawa and Schroeder, 2011; Herreras, 2016). In this manner, it remains a challenge to separate synaptic from non-synaptic components when measuring neural activity.
LFP is the low-pass component of the extracellular currents, and it is widely used as an extracellular measure of brain activity. As long as the LFP is a remote rather than a local measurement (Kajikawa and Schroeder, 2011), there is a strong possibility that it reflects activity of structures far from the recording point (Herreras, 2016). Thus, many studies have explored its origin in order to better understand the activity that it mirrors (Weiss and Faber, 2010; Kajikawa and Schroeder, 2011; Buzsáki et al., 2012; Anastassiou et al., 2015; Herreras, 2016).

1.2.1 How do electric fields emerge?

By and large, pyramidal cells are considered the major contributors to extracellular fields as a result of their shape (their long somatodendritic axis generates strong dipoles) and abundance in the cortex. In addition, their spatial distribution and temporal synchrony determine the magnitude of extracellular currents (Fig. 1.3A) (Weiss and Faber, 2010; Buzsáki et al., 2012). Current sources with neuronal origin present a dipolar structure (Herreras, 2016); in addition, the large current fluctuations at the pyramidal somas occurring when activity is synchronized leads to distinct polarity zones (positive and negative) (Buzsáki et al., 2012). This way, an extracellular dipole is formed between IG and SG layers in the cortical network; the parallel distribution of pyramidal cells causes a current flow perpendicular to their axis that when superimposed generates the active dipole. An outcome of this is the polarity inversion observed at SG layers in the LFP when recording SO across cortical layers (Fiáth et al., 2016)(Fig. 4.1). Thus, the fact that both SG and IG layers reflect depolarization of neuronal populations during Up states with different polarities on the LFP (positive and negative, respectively), is in line with the idea that LFP polarity does not mirror the active currents of synapses (Kajikawa and Schroeder, 2011; Herreras, 2016).

Those current flows along the vertical axis of pyramidal neurons, which result

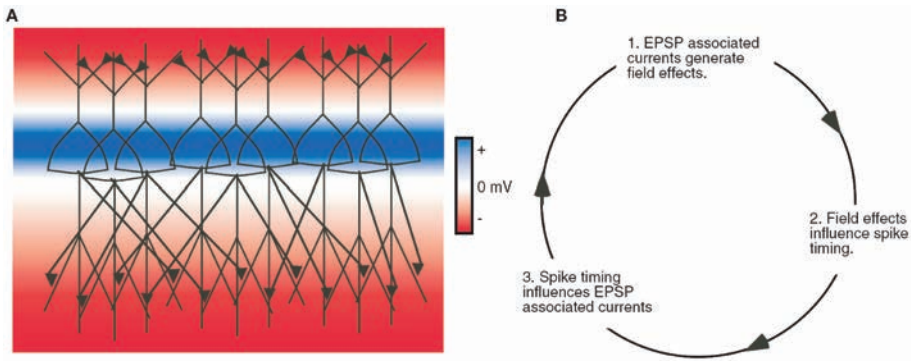

FIGURE 1.3: **Amplification of EF by chemical synapses on pyramidal cells** A, Schematic of pyramidal cells arranged in a parallel orientation. Color code indicate the extracellular potential. B. Feedback effect between synaptic activity and its EF. Reproduced from *Frontiers in Neural Circuits* (Weiss and Faber, 2010).

in a dipole on the cortical network, illustrate the variation along time of the EFs, in other words, they illustrate EF propagation (Buzsáki et al., 2012). The transmission of EF through biological tissue from a source to a measurement sensor defines the term *volume conduction* (Rutkove, 2007). The expansion of the volume conduction will be determined by the current dipole, already described, and the conductivity of the medium (Buzsáki et al., 2012).

1.2.2 Electric fields within the brain tissue

Regarding the conductivity in the brain tissue, there is controversy about whether we should consider the brain as a homogeneous or a non-homogeneous medium. On one hand, cortical impedances measured in the visual cortex of *in vivo* monkeys described the tissue as a homogeneous medium where the EF propagation is isotropic and permits an equitable propagation of any frequency, meaning that tissue impedance is frequency independent. According to this, LFP dimension will be determined by the size of the signal rather than by tissue properties (Logothetis et al., 2007). On the other hand, frequency attenuation is observed when measuring extracellular potentials, leading to higher spacial coherence in SO than in high frequency oscillations (Destexhe et al., 1999). The homogeneous isotropic medium does not reflect the frequency dependent attenuation, so it is not adequate for

modeling LFP signals. A non-homogeneous extracellular conductivity results in a low pass filter that makes the low frequency events attenuate less with distance, generating the LFP/EEG signals. These frequency filtering properties of the tissue are determined by the structural composition of the medium, which requires considering the extracellular medium non-homogeneous and anisotropic (Bédard et al., 2004). This debate remains open the question whether the tissue has any influence on the EF propagation.

Considering the above, greater attention has been focused on the role of volume conduction and EF propagation in the brain tissue, as they are also reflected on extracellular signals toghether with the spiking activity.
Good evidence that emphases the need to pay heed to non-synaptic mechanisms when measuring LFP was reported in the study of Kajikawa and Schroeder, where sources (positive charges traveling to the extracellular space) and sinks (positive charges traveling to the intracellular space) obtained with current source density analysis (CSD) could not reproduce the observed LFP. Besides, responses to different tones recorded at two different sites elicited different spatial propagation of LFP, CSD and MUA. While CSD and MUA disappeared when moving the frequency tone from the best frequency tone, LFP measurement remained (the order of the spatial spread differences were: LFP $>$CSD $>$MUA) (Kajikawa and Schroeder, 2011). Therefore, volume conduction may exert a greater impact on LFP than on MUA (or CSD). Hence, the neural activity reflected on LFP signals propagate not only through synaptic events, but also through non-synaptic mechanisms.

Indeed, recent work on an unfolded hippocampus preparation showed how epileptiform activity propagates by EFs at surprisingly low speed ($\sim$0.1 m/s) independently of synaptic activity (Zhang et al., 2014). To further investigate the role of the extracellular medium on this propagation, osmolarity was increased in order to enlarge the distances between neurons and widen the extracellular space (Traynelis and Dingledine, 1989). The result was a reduction of 46.8 % in speed propagation (Shahar et al., 2009; Qiu et al., 2015) revealing that extracellular space has an influence on EF propagation, particularly decreasing its velocity when increasing the space.

1.3 Synaptic activity and electric field dialogue

Under this scenario where synaptic and non-synaptic mechanisms coexist, there is a feedback effect between the structural neural activity and the endogenous EFs which shape and modulate the final network activity (Fig. 1.3B) (Jefferys, 1995; Fröhlich and McCormick, 2010; Weiss and Faber, 2010; Anastassiou et al., 2011; Schmidt et al., 2014; Anastassiou and Koch, 2015).
The interactions of EF are shaped by the temporal dynamics of synaptic activity (Weiss and Faber, 2010). When these interactions lead to changes in the membrane potential of neurons, and consequently in spiking, it can yield a non-synaptic mechanism known as *ephaptic coupling* (Anastassiou and Koch, 2015). Ephaptic coupling mainly affects population activity under hypersynchronous states (Buzsáki et al., 2012); it can induce small but coherent changes in the firing timing of neuronal populations, thus implying that field effects can modulate oscillatory activity (Reato et al., 2010).

The three main components of neural activity (synapses, neurons and networks) are sensitive to extracellular EF (Anastassiou and Koch, 2015). EF can alter the presynaptic membrane potential by inducing changes in the ionic flows. Also, EF can influence chemical synaptic transmission in a network by clearing negative glutamatergic charges or through changes in voltage gated channels, as well as by mediating neurotransmission and collaborating in fast rhythmogenesis (Weiss and Faber, 2010).

Researchers that have tried to address the effect of endogenous EF on neuronal activity by applying exogenous EF through two parallel electrodes outside the tissue preparation (Radman et al., 2007; Fröhlich and McCormick, 2010; Reato et al., 2010; Schmidt et al., 2014), report a critical effect of weak EF stimulation on spiking neural activity due to its impact on membrane voltage. Besides, in a 12 pipette set up, where electrical stimulation was applied inside and outside individual cells while recording extracellular fields at different specific locations next to an active neuron, elicited ephaptic coupling at the level of single cells. Extracellular EF was not able to induce any action potential, but it did entrain subthreshold activity and spike trains when it oscillated at slow rhythms (1 Hz) (Anastassiou et al., 2011).
These results reinforce the idea that EF effects can be strong enough to be magnified on the network dynamics. In particular, *in vitro* experiments on hippocampal slices, together with an *in silico* model supported that weak

applied EFs influenced oscillatory activity (Reato et al., 2010); in this manner, ephaptic coupling synchronizes networks with a stronger feedback effect on oscillatory patterns, specially on SO (Fröhlich and McCormick, 2010; Anastassiou et al., 2011; Anastassiou and Koch, 2015).

It was the pioneering work of Fröhlich and McCormick in 2010 which clearly exhibited the effect of an endogenous (and not exogenous) EF on spontaneous oscillatory activity. In cortical ferret slices eliciting SO, they applied weak external EF stimulation (2-4 V/m) through two parallel electrodes that mimicked the endogenous *in vivo* field activity recorded in anesthetized ferrets. This EF stimulation was able to modulated the oscillatory network activity (Fig. 1.4), supporting the idea that endogenous EFs are not a mere idling of the neural activity (Weiss and Faber, 2010). Further exploration of the feedback between EF and synaptic activity demonstrated that the state of the targeted network is critical for the effect that EF might induce; so, only weak EF stimulations with frequencies similar to the ongoing oscillation induced changes in the endogenous activity (Schmidt et al., 2014).

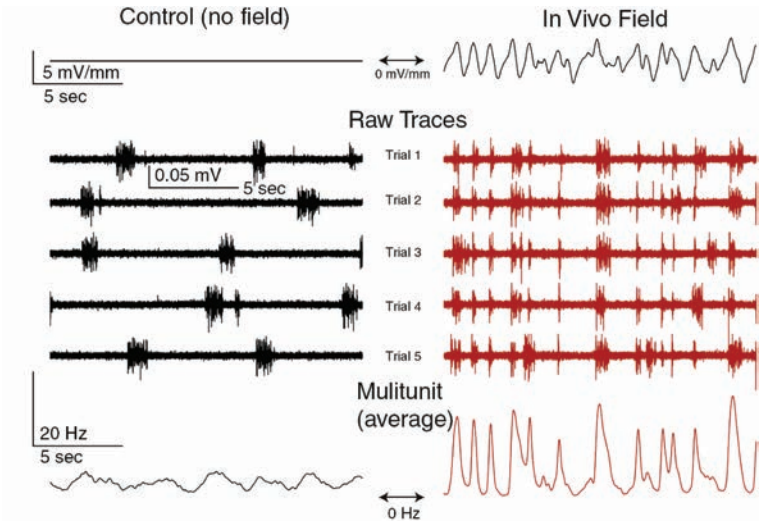

FIGURE 1.4: ***In vivo* EF modulates *In vitro* SO** Left: no field applied (control). Right: *in vivo* field applied. Top: applied *in vivo* field. Middle: multiunit activity recorded in cortical slices. Bottom: multiunit activity averaged from 20-30 trials. Adapted from *Neuron* (Fröhlich and McCormick, 2010).

Despite these experiments demonstrated the feedback interaction between EFs and synaptic activity, they did not address the modulation of synaptic activity by its authentic endogenous EF.

1.3.1 The slow oscillation as the key player

Considering the above, the SO represents a suitable testbed to study the synaptic and non-synaptic propagation, as well as the interaction between both components. First, the SO reflects an emergent property of the network where the neural activity is synchronized in active and silent states (Steriade et al., 1993b). Second, it can be spontaneously generated (and also induced) *in vitro* preserving its fundamental properties (Sanchez-Vives and McCormick, 2000) while easing specific manipulations (see *Materials and Methods* chapter) to better control the local cortical circuit, and thus explore its dynamics along the cortical structure. Third, as emergent property of the network, it is more sensitive to the field effects than single neurons activity (Anastassiou and Koch, 2015); and at the same time, as oscillatory pattern, it will reveal better the effect of endogenous EF in the neuronal activity (Weiss and Faber, 2010). Fourth, SO has been proved to be the oscillatory rhythm producing the greatest effect on ephaptic coupling (Anastassiou et al., 2011).

Moreover, the SO seems to be the default mode activity of the cortical mantle during deep sleep, anesthesia, or even in cortical slices preparation (Sanchez-Vives and Mattia, 2014; Sanchez-Vives et al., 2017b). Such synchronized cortical activity occurs during functional and anatomical disconnection from other inputs and is associated to a broad range of different functions, from metabolic homeostasis (Xie et al., 2013) and cellular maintenance (Vyazovskiy and Harris, 2013), to plasticity recalibration (Reig et al., 2006; Reig and Sanchez-Vives, 2007) and memory consolidation (Marshall et al., 2006). Additionally, the SO has been suspected to be the basal frequency needed to group other higher frequencies (spindle and delta) contributing to the reorganization of distant networks (Neske, 2015). Thus, elucidating the SO mechanisms will give information about the properties of the underlying network, and can be useful to develop mechanistic investigations for neurological disease were the functions just mentioned are imbalanced (Ruiz-Mejias et al., 2016; Castano-Prat et al., 2017).

Chapter 2

Objectives

The principal aim of this thesis is to determine the role of synaptic and non-synaptic (endogenous electric fields) components in the generation and propagation of slow waves.

Regarding the propagation of slow waves, the objectives are:

1. To explore the spatiotemporal patterns of slow wave propagation across cortical columns and layers.
2. To determine how excitability modulates the spatiotemporal regularity of the slow oscillatory activity in the cortical network.

Regarding the non-synaptic propagation of slow waves, the objectives are:

1. To explore the propagation of endogenous electric fields induced by slow waves in the cortical tissue, dissecting them from the synaptic components.
2. To study the influence that the laminar structure and the size of the extracellular space may exert on the electric field propagation of slow waves.
3. To investigate the modulation that endogenous electric fields may induce on cortical slow waves.

Chapter 3

Materials and Methods

3.1 Experimental procedure

The main methods used during this doctoral thesis consisted of *in vitro* experiments performed in 98 visual cortical slices from ferrets (*Mustela putorius furo*) (Sanchez-Vives and McCormick, 2000). Cortical slice preparation allows us to explore and manipulate the local cortical microcircuit easily accessing all cortical layers. In addition, this preparation is well known for eliciting robust spontaneous slow oscillations (SO) (Sanchez-Vives and McCormick, 2000; Compte et al., 2008; Sanchez-Vives, 2012) similar to the ones observed during slow-wave sleep (Steriade et al., 1993b). These advantages made the *in vitro* preparation ideal to achieve the objectives mentioned above.
Two different sets of experiments were done to study synaptic and non-synaptic propagation of an active cortical circuit. Preparation and maintenance of slices, as well as extracellular local field recordings were common along all experiments. Different protocols and analysis were performed, mainly for the non-synaptic propagation experiments, which will be described in detail.

3.1.1 Preparation and maintenance of slices

Ferrets (4-10 months old, both sex) were anesthetized with sodium pentobarbital (40 mg/kg) and decapitated. The entire forebrain was rapidly removed to oxygenated cold (4-10°C) bathing medium (Sanchez-Vives, 2012). Ferrets were treated in accordance with the European Union guidelines on protection of vertebrates used for experimentation (Strasbourg 3/18/1986). All experiments were approved by the local ethical committee.
Coronal slices (0.4 mm thick) from visual cortex (areas 17, 18 and 19) were

used. A modification of the sucrose-substitution technique (Aghajanian and Rasmussen, 1989) was used to increase tissue viability. During slice preparation, the tissue was placed in a solution in which NaCl was replaced with sucrose while maintaining osmolarity. After preparation, the slices were placed in an interface style recording chamber (Fine Sciences Tools, Foster City, CA), where they were superfused with an equal mixture in volume of the normal bathing medium, artificial cerebral spinal fluid (ACSF) and the sucrose-substituted solution, for 15 minutes. Following this, normal bathing medium was switched into the recording chamber and the slices were superfused for 1 hour and 20 minutes; the normal bathing medium contained (in mM): NaCl, 126; KCl, 2.5; $MgSO_4$, 2; Na_2HPO_4, 1; $CaCl_2$, 2; $NaHCO_3$, 26; dextrose, 10; and was aerated with 95 % O_2, 5 % CO_2 to a final pH of 7.4. Then, a modified slice solution was used throughout the rest of the experiment; it was similar to the normal bathing medium except for different levels of the following (in mM): KCl, 4; $MgSO_4$, 1; and $CaCl_2$, 1 (Sanchez-Vives and McCormick, 2000; Sanchez-Vives, 2012). Bath temperature was maintained at 34-36°C.

Complete cut of the slice

In order to separate the synaptic from the electric fields (EF) (non-synaptic) activity, I performed a complete cut of the slice perpendicular to white matter with a scalpel blade on 73 out of the 98 slices. The cut was done while the slices were in the interface chamber, which allows the two sides to remaine tightly in contact, without discontinuity between them, as could be seen through the microscope (Fig. 3.1). The slices remained mechanically stable and firmly adhered at the bottom of the chamber formed by filter paper (Fig. 3.3). At the end of every experiment, we removed the two sections of the slice from the filter paper, confirming that they were indeed completely separated, which was the case in all the experiments.

3.1.2 Extracellular recordings

Extracellular local field potential (LFP) recordings were obtained with 16 gold electrodes plated with platinum black disposed on a recording grid (Fig. 3.1). The recording array was placed on top of the slices and 16 simultaneous recordings were obtained. In the sectioned slices 10 electrodes recorded at the left side of the cut and 6 electrodes at the right side (Fig. 3.1).

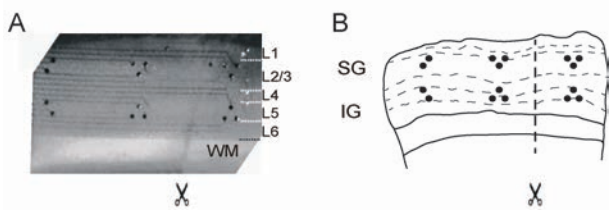

FIGURE 3.1: **Sectioned cortical slice.** A. Sectioned cortical slice picture with a 16 channel array positioned on the surface. Notice the tenuous line at the scissors level showing the cut without discontinuity between the resulting slice pieces. B. Schematic of the sectioned cortical slice with 10 electrodes recording at the left side and 6 electrodes recording at the right side. WM: white matter; L1-6: layers 1 to 6.

The grid including an array of holes was designed and fabricated using SU-8 negative photoresist or polyamide (Fig. 3.2). The holes allowed oxygenation of the slices, they were used to provide mechanical stability and to allow pipettes to reach the slice for local drug applications (Fig. 3.3).
In each of the recording points, there were 2-3 electrodes (separated by 200 μm) (diodes or triodes, respectively). They were positioned such that half of them would record from supragranular (SG) and the other half would record from infragranular (IG) layers (diodes / triodes were 750 μm apart in the vertical axis), as well as from 3 different cortical columns (1.5 mm apart in the horizontal axis) (Fig. 3.1 and 3.2A).
The electrodes were 50 μm in diameter, resulting in an impedance values of $|Z| \sim 10M\Omega$ at 1 kHz. The impedance was decreased 2-fold by electrochemically coating the electrodes with a layer of black platinum, what enhanced the electrode behavior, resulting in electrode impedance values being two orders of magnitude below the amplifiers input impedance over the whole frequency range. Electrode impedances and phases were tested with known signals prior to the recordings for each array (Fig. 3.2B); this way we excluded the possibility of phase delays or distortion that differences in electrode coating could induce.

Neural activity was referenced to an electrode placed at the bottom of the chamber in contact with the ACSF. Unfiltered signals were acquired with Multichannel System amplifier and digitized at 10 KHz with a Power1401

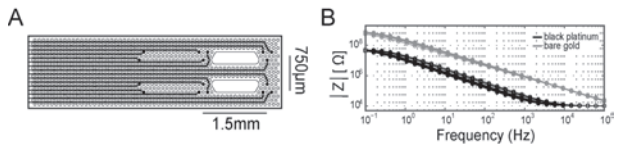

FIGURE 3.2: **16 electrodes array.** A. Customized recording grid with 16 electrodes (black dots) organized in 2 or 3 groups with holes (white dots) between them. B. Impedance characterization before (gray line) and after (black line) coating with black platinum for the whole frequency range.

interface and Spike2 software (CED, Cambridge, UK). No filters were added during the recording stage to avoid signal distortion.

3.1.3 Experimental protocols

To study different excitability levels on the propagation of slow waves, the ionic composition of the ACSF was modified on 13 slices by varying the K^+ concentration from 1 mM to 7 mM (Sancristóbal et al., 2016), these values are located at the same level as the one found *in vivo* (Amzica et al., 2002; Bazhenov et al., 2004). That modification changes the extracellular K^+ concentration leading to variations in the excitatory network level.

To explore the influence of structure and extracellular space on the non-synaptic propagation of slow waves, as well as the modulation between both disconnected networks, different protocols and manipulations were performed on the sectioned slices, they are described below.

Drug applications

Different pharmacological agents were used: glutamic acid (glutamate) from RBI, tetrodotoxin (TTX) from Tocris, bicuculline methiodide (BMI) from Sigma and saccharose from Scharlau. Applications were either local or bathed depending on the purpose to achieve (explained below).

Glutamate (0.5 mM) and TTX (30 μM) were delivered locally through a glass micropipette. In both cases, borosilicate glass capillaries were pulled on a Sutter Instrument P-97, their tips were broken (1-4 μm diameter) and later filled with the drug. Brief pulses of pressure (ranging from 4 to 150 ms, and 5 to 30 psi; adjusted depending on the response to evoke) were applied. Such

local applications were delivered at different positions within the slice.

Glutamic acid. Local applications of glutamate are widely known to evoke highly stable responses by activating glutamate receptors and recruiting local network activity (Sanchez-Vives and McCormick, 1997; Sanchez-Vives et al., 1997, 2008). Such applications allow us to better control the time and location where the Up states (or glutamate response) are originated to study their non-synaptic propagation. They were used, not only to study the EF propagation across the cut, but also to investigate modulation between the two disconnected networks by: (1) inducing small responses in one side to increase excitability and see if endogenous EF could trigger spontaneous Up states in a more depolarized network; and (2) inducing suprathreshold responses at different frequencies to be able to entrain the disconnected network in a desired frequency.
Tetrodotoxin. TTX, selective inhibitor of Na^+ channel conductance that abolishes spontaneous multiunit activity. It was applied to rule out interactions between synaptic and non-synaptic activity.

BMI (2.4 - 3 μM) and saccharose (40 mM) were bath applied. It should be noted that in the interface chamber used it takes around 20 minutes to get a stable concentration in the bath, so all measurements were taken after this period.

Bicuculline methiodide. BMI is a $GABA_A$ receptor blocker that acts as a competitive inhibitor of GABA. It was used to transform the spontaneous SO in epileptiform activity (Sanchez-Vives et al., 2010), generating large responses strongly evident across the cut.
Saccharose. Saccharose 40 mM was used to increase osmolarity and with it the extracellular space. A concentration of 40 mM saccharose causes an increase of 40 mOsm (from 328 mOsm on control condition, to 368 mOsm under hyperosmolar condition), that involves a 12% increment, what has been proved to have an effect on the propagation of epileptiform activity (Shahar et al., 2009; Qiu et al., 2015).

Inverted slices

To further explore the influence of the laminar cortical structure in the non-synaptic propagation of slow waves, one side of the cut slices was

overturned, such that IG layers were next to SG layers and vice versa. This manipulation was done consecutively to the cut in the interface style recording chamber, the bath flow was increased while gently rotating the right side of the slice with the forceps tips. The result was a sectioned cortical slice where one side had an inverted laminar structure (Fig. 3.3).

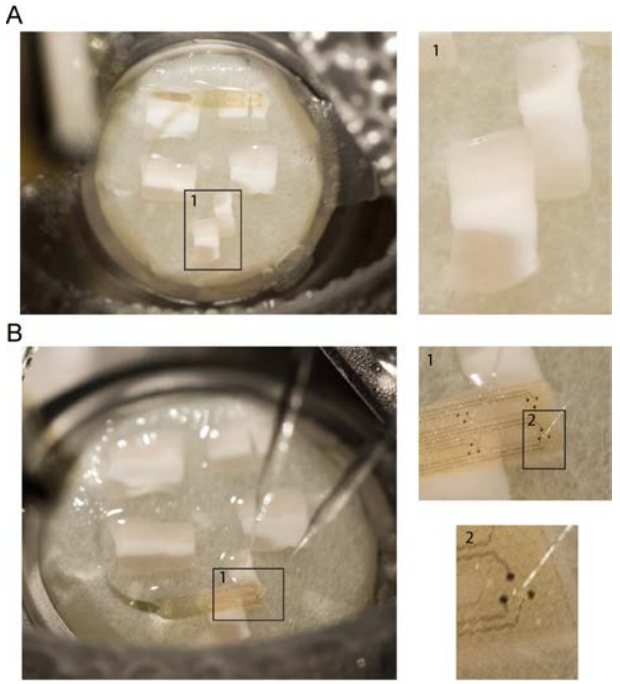

FIGURE 3.3: **Sectioned visual cortical slices adhered at the filter paper in the interface chamber.** A. Magnification of an inverted slice. B. Same preparation with the array on top of the inverted slice and two glass pipettes used for local applications passing through the array holes.

Electric field stimulation

In order to achieve synchronization between both disconnected networks, the excitability of the whole slice was increased by means of external EF manipulations. Thus, direct current (DC) stimulation was applied as described in Fröhlich and McCormick, 2010 and Sanchez-Vives et al., 2017a. Briefly, two customized AgCl electrodes (1 mm diameter, 10 mm length) were placed parallel to the cortical surface, this arrangement allowed us to generate a

uniform EF parallel to the apical - dendrite axis of pyramidal cells. Thus, positive fields (oriented from IG layers to SG layers) depolarized pyramidal cells leading to an increase in the network excitability; while, negative fields (oriented from SG layers to IG layers) decreased the network excitability by hyperpolarizing pyramidal cells (Fig. 3.4). The different EF applied (±1-4 V/m) were calibrated before every experiment. The current to generate the field was produced with a stimulus isolator (360A, WPI, Aston, UK).

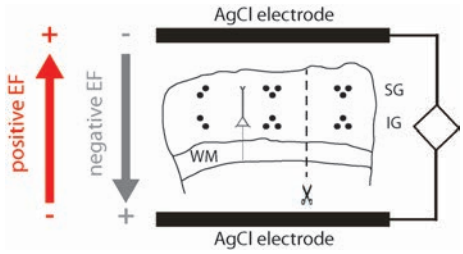

FIGURE 3.4: **Scheme of the recording configuration under EF stimulation.** Stimulation electrodes parallel to white matter (WM). Positive/negative EF parallel to the pyramidal neurons axis (red/gray, respectively). 16 electrodes recording from supragranular (SG) and infragranular (IG) layers.

3.1.4 Histology

Nissl staining was used for visualizing lamination of the cortex and studying slow wave propagation across columns and layers. After recording, 9 slices were marked where the array was positioned and fixed in paraformaldehyde (4%) for later Nissl staining. Slices 400 μm were washed during 4-5 days in 0.1 M PB containing 30% saccharose. Then 50 μm thick slices were cut in a Thermo Scientific MICROM HM 450 microtome and placed on gelatin-coated glass slides. After drying overnight, slices were incubated 2 hours in ethanol 70% for the subsequent double toluidine staining: first, nuclei were stained by an incubation of 15 minutes on toluidine blue and afterward dehydrate with ascending alcohol series, 5 minutes incubation on xylene was done to clarify the tissue for the second staining. Second, similar incubations, 10-15 minutes toluidine and different increasing alcohols, finishing with two xylene incubations were used to stain cytoplasm. Finally, slices were mounted in DePeX medium. Images were visualized and taken with a confocal laser

microscope.
Layers were limited according to density and size of the observed cells (Homman-Ludiye et al., 2010) (Fig. 3.5).

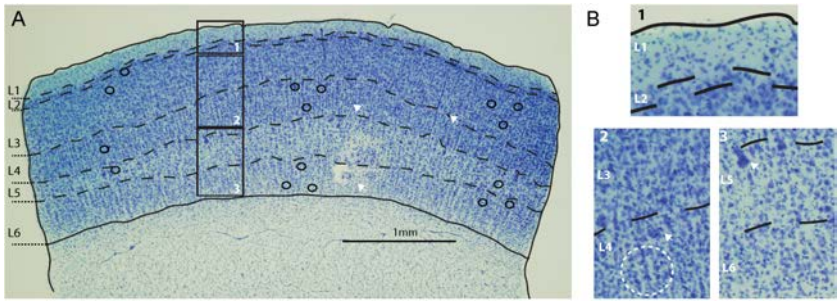

FIGURE 3.5: **Nissl stained visual cortical slice.** A. Complete visual cortical slice Nissl stained with the 16 channels electrode array superimposed (black circles) according to the observed marks (white arrows). Layer limits displayed with dashed lines. B. Amplifications of A displaying differences between layers. L1:the less dense layer, L2: the thinnest layer with mainly bulky cells, L3: the thickest layer with mixture of small and bulky cells; L4: layer with big pyramidal neurons (top arrow) mixed with smaller cells displaying a clearer columnar pattern (dash circle); L5: layer less dense than L4 and L6 with big pyramidal cells (arrow); L6: mixture of small and big cells.

Nissl staining was performed in collaboration with Alberto Muñoz Céspedes at Javier de Felipe laboratory (Instituto Cajal, Madrid).

3.2 Data analysis

All analysis were performed offline with either custom-written or Matlab toolbox scripts (The MathWorks Inc. Natick, MA). Spike2 software was used for offline analysis when stated. All average values are presented as mean $\pm$ SE.

3.2.1 Multiunit Activity and Up/Down state detection

From all of the recordings multiunit activity (MUA) was estimated to further detect Up and Down states from the SO as described in previous works

(Compte et al., 2008, 2009; Reig et al., 2010; Sanchez-Vives et al., 2010; Ruiz-Mejias et al., 2011; Mattia and Sanchez-Vives, 2012; D'Andola et al., 2017). Briefly, MUA was estimated as the change in power of the Fourier high frequency components from the LFP signal. Later, population firing rate was obtained from the MUA (Mattia and Del Giudice, 2002). To detect Up states a threshold was set in the log(MUA) as described in Reig et al., 2010 and Ruiz-Mejias et al., 2011 (Fig. 4.2).
From the transformed log(MUA) signal different parameters were quantified: frequency of the SO, Up and Down state durations, mean and maximum firing rates in the Up states. Coefficients of variation (CV)(standard deviation/mean) were used to measure variability.

3.2.2 Slow wave propagation analysis

To study slow wave propagation within the slice the analysis was based in the Up/Down detection already described. Thus, times at which each electrode crossed the threshold in the log(MUA) were taken and transformed into time lags. Next, these time lags were interpolated such that a wave-front could be draw (Fig. 4.4) (Capone et al., *under review*; Sancristóbal et al., 2016).
Waves that propagated through every columns were considered and clustered by Principal Component Analysis based on the origin, speed and direction to differentiate types of propagation.
These clustered waves allowed us to compute an early propagation strip (EPS) from the points where the wavefront tip occurred earlier. EPS plots were overlapped with their respective Nissl stained slice pictures to measure the portion of the EPS area included in each layer (Capone et al., *in preparation*).
Also, for each clustered wave, percentages of correlations between them were computed for spatial consistency (SC) quantification to explore regularity patterns under different excitability levels (Sancristóbal et al., 2016).

Analysis in the propagation of slow waves were performed in collaboration with Maurizio Mattia (Instituto Superiore di Sanitá, Rome, Italy). Specifically, EPS analysis were performed by Cristiano Capone and spatial consistency analysis by Pol Boada.

3.2.3 Analysis of non-synaptic propagation of slow waves

To explore the propagation of slow waves in the absence of synaptic activity the first step was to detect the EF waves in a synaptic disconnected network. With that purpose mean responses were obtained by averaging the signal across repetitions of spontaneous (or evoked) Up states, triggered glutamate responses or epileptiform responses, and tested for significant differences from baseline values.
Cases where the studied response on one side of the slice overlapped on time with the spontaneous Up states (or epileptiform responses) of the other side were discarded from the averages.

To characterize the damping, distortion and delays on the endogenous EF waves a curve fitting was computed in a time window of 2.5 seconds on the glutamate responses. Delays were quantified from the latency between the waves peaks at both sides of the cut. Widening and compression were measured with respect to the original wave to evaluate the distortion. Thus, peak compression (PC) was defined as the duration difference between the waves at both side of the cut (the wave reference -Dr -, where the waves are originated; and the waves recorded on electrodes at the other side - De -) divided by the reference duration (Gonzalez-Andino et al., *under review*).

$$PC = \frac{Dr - De}{Dr} \tag{3.1}$$

Analysis to characterize the propagation of slow waves in the absence of synaptic activity were performed in collaboration with Sara L. González Andino and Rolando Grave de Peralta Menendez (Electrical Neuroimaging Group, Geneva, Switzerland).

Once we were able to asses the presence of the EF responses, we proceeded to study the modulation of SO by endogenous EF with different analysis depending on the protocol performed (detailed below). In all the cases frequency of Up/Down cycle was quantified at both sides of the cut based on the log(MUA) detection, as described at the beginning of this section.

Correlations. On the slices where DC stimulation was applied we computed correlations between both sides of the cut to look for synchrony. Cross-covariation coefficients were computed on the log(MUA) signal with

Matlab toolbox.
Also, phase locking values (PLV) (Lachaux et al., 1999) for SO were quantified between two different channels from both sides.

Exponential fitting. On the slices where glutamate puffers were delivered at different frequencies to entrain the rhythmicity of the disconnected network the analysis was as follows.
First, Up/Down detection was computed to obtained the SO frequency at both sides. The frequency change of the glutamate release, was considered the reference time from which an exponential fit was adjusted on the frequency increase/decrease of the side where no glutamate was applied.

$$y = a(1 - e^{-\frac{1}{b}t}) \tag{3.2}$$

$$y = a(e^{-\frac{1}{b}t}) \tag{3.3}$$

Being b the time constant τ (63.2 %) that represents the time needed for the non stimulated side to be modulated and to change its frequency. Cases where τ reached values higher than 120 seconds (time period analyzed after the frequency change) were discarded as outliers.

Then, normalized differences of frequencies (ND) were computed to better compare the frequency variation between both sides.

$$ND = \left| \frac{F_2 - F_1}{\frac{F_2 + F_1}{2}} \right| \tag{3.4}$$

For the side where the frequency was induced, F_1 and F_2 were determined by the local application glutamate periodicity. For the modulated side, F_1 is the median obtained in the 90 seconds previous to the frequency change, and F_2 is the asymptotic value of the exponential.

Analysis to study the modulation of SO by endogenous EF were performed in collaboration with Lorena Perez and Álvaro Navarro from our laboratory.

3.2.4 Statistics

Values are presented as mean ± SE. Either parametric (Student's t-test) or non parametric (Mann-Whitney U test or Wilconson sign-rank test) were used depending on the properties of the samples to be compared.

Chapter 4

Results

Results reported in this thesis show the spatiotemporal dynamics of the slow oscillations (SO) in an *in vitro* preparation of ferret visual cortex. Specifically, spontaneous SO were recorded with 16-channel array (see *Materials and Methods*) covering different columns and layers within the cortical slices (Fig. 4.1A). This is the first time that, to our knowledge, these 2D recordings are from a slice. A total of 98 slices spontaneously generating SO in most electrodes in the array were used. Figure 4.1B displays a representative case eliciting the spontaneous rhythmic pattern in the 16 electrodes.

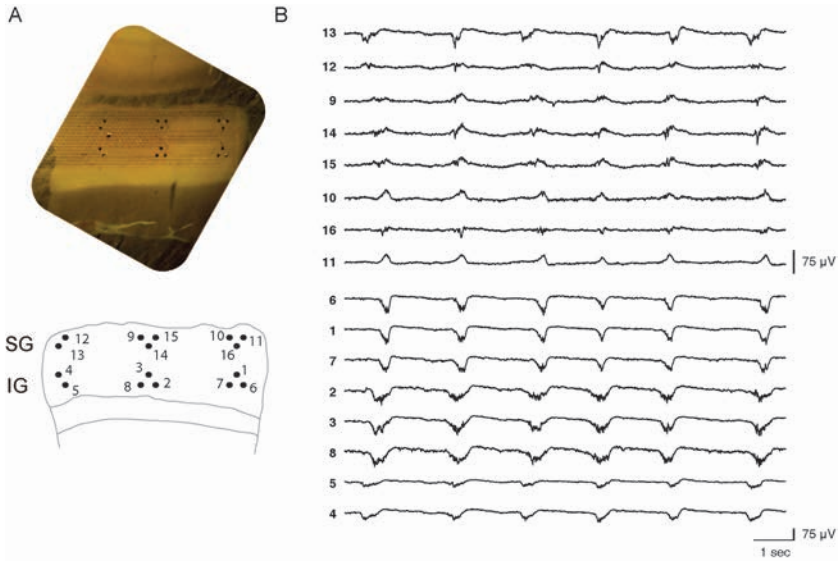

FIGURE 4.1: **SO recorded with 16-electrode array.** A. Picture (top) and scheme (bottom) of a 16-channel array over a visual cortical slice. B. 16 channels eliciting spontaneous SO.

From each raw local field potential (LFP) the network relative firing rate was estimated to further compute Up/Down state transitions and durations as illustrated in figure 4.2A with the red line. Also, the associated multiunit activity (MUA) color coded in the raster plot and the waveform average obtained from the relative firing rate were used to calculate transitions states (Fig. 4.2B-C) (see *Materials and Methods*).

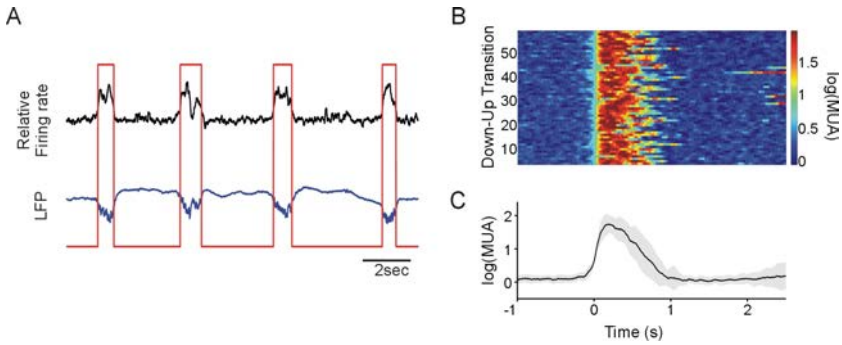

FIGURE 4.2: **Analysis of the population activity during SO.** A. Relative firing rate (black) and LFP recording (blue). Up and Down state detection is represented with a red line. B. Raster plot of 60 aligned Up states. C. Waveform average of the relative firing rate that is used to calculate Down-Up/Up-Down transitions and maximum firing rate. The shade represents the SD. LFP, local field potential; MUA, multiunit activity.

4.1 Propagation of slow waves

To achieve the first objective regarding the propagation of slow waves across columns and layers, I recorded spontaneous SO traveling along the cortical visual network on 12 slices. The first step was to identify the active and silent periods that composed SO. Thus, estimation of the multiunit activity (MUA) was used to analyze population firing rate (see *Materials and Methods*). From this estimation, Up and Down states were represented by the high and low firing rate peaks, respectively (Fig. 4.3B). Down peak standard deviation was considered the threshold to further detect transitions between Up and Down states; and from theses, Up/Down state durations and cycle frequency were measured (Fig. 4.3C).

Similar results to previous works performed with conventional extracellular recordings were observed (Sanchez-Vives and McCormick, 2000; Sanchez-Vives et al., 2010; Reig et al., 2010): bimodal distribution of the MUA and state durations showing the differences between Up ($\sim$ 310 ms) and Down ($\sim$ 3 s) states activity. Also MUA time course for state transitions elicited an average oscillatory cycle frequency of $\sim$ 0.3 Hz (Fig. 4.3 B-D). This way, we proved the reliability of the new surface array recording spontaneous SO (Capone et al., *under review*).

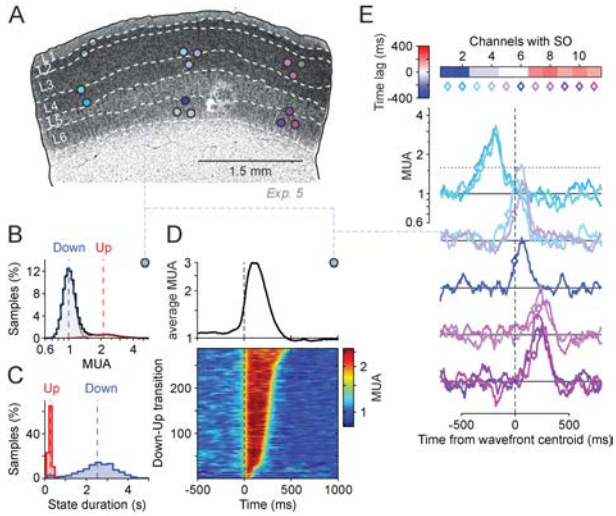

FIGURE 4.3: **Propagation of slow waves.** Analysis of population activity in one slice recorded with a 16-channel array. A. Nissl stained slice with layer limits (dashed white lines) and 16 electrodes (circles, unused electrodes displayed in gray) superimposed. B-C. Bimodal distribution of the MUA and state duration (respectively) for Up (red) and Down (blue) states. Vertical dashed lines, mean values. D. Average MUA (top). Down-Up transitions (dashed line) and maximum firing rate (MUA, color code). E. Time course of the MUA estimated from eleven channels. Horizontal dashed line represents MUA threshold for detecting Up states onsets.

4.1.1 Up/Down cycle propagation across visual cortical slices

Thanks to the simultaneous recordings with the 16-electrode array, we observed that spontaneous Up states were not isolated events, they

propagated across the slice in agreement with past studies (Sanchez-Vives et al., 2010; Wester and Contreras, 2012; Reyes-Puerta et al., 2016). To compute propagation within the slice we measured time lags between Up state onsets of every channel, particular example is shown on figure 4.3 E-top, where slow waves propagate in the horizontal direction from the left (blue traces) to the right (purple traces).

Results across experiments displayed different propagation patterns in the horizontal direction. To further explore the spatiotemporal dynamics, full waves (waves propagating across the three columns of the array) were clustered in a fixed number of 10 wave clusters (Fig. 4.4B). For each cluster, average Up state onsets were used to estimate the time course of waves along the rectangular area covered by the array, obtaining a spatial interpolation that reflected the different wave profiles (Fig. 4.4C) (see *Materials and Methods*). No preference for the ignition site was found across experiments: $\sim$59 % of waves were originated at the lateral columns of the array, while $\sim$34 % appeared first at the center (Fig. 4.4D). Besides, a confined shape perpendicular to the cortical surface underlay the faster velocity along the vertical (depth) direction with respect to the horizontal (lateral). The time course obtained from the interpolation previously described exhibited propagation speeds of slow waves similar to previous studies: 5.8 ± 1.8 mm/s lateral (horizontal direction) and 8.9 ± 3.4 mm/s in depth (vertical direction).(Fig. 4.4E).

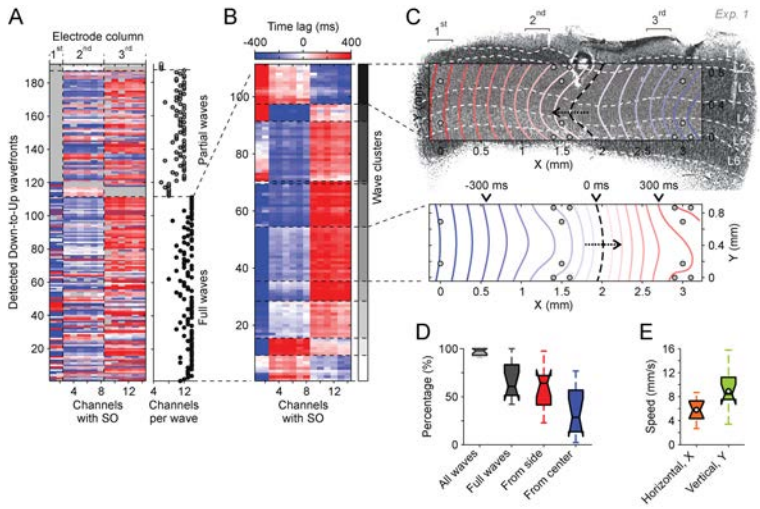

FIGURE 4.4: **Spatial interpolation from clustered waves.** A. Clustered traveling waves from an example experiment displayed on a time lag matrix, gray areas failed Up state detections. B. Same as A for full waves (waves propagating across the three columns of the array). C. Time course of average wavefronts obtained from the interpolation of Up state onsets for two different clusters. D. Average fraction of full and partial waves and electrodes from where Up states are originated (n=12 slices). E. Box plots of the speed of waves traveling lateral (horizontal, X) and in depth (vertical, Y) directions. Dashed lines, extreme values; central mark, median.

4.1.2 Laminar structure shapes slow wave propagation

Previous *in vitro* studies demonstrated the role of layer 5 in the origin of spontaneous SO (Sanchez-Vives and McCormick, 2000; Wester and Contreras, 2012). To investigate the link between the propagation of emergent spontaneous activity and cortical structure, we explored how the excitation features of waves were preserved across the different obtained clusters.

Specifically, an early propagation strip (EPS) was identified from the location where Up state onset times appeared earlier along the horizontal direction (Fig. 4.5A) (see *Materials and Methods*). The EPS density obtained from different clustered waves of the same slice were similar, supporting the idea that wavefronts shapes are independent of the origin site and the propagation direction (Fig. 4.5B). To prove whether these EPS represented the part of the

slice with the highest excitability we interpolated the average durations of Up states (T_{Up}) (Fig. 4.5C) and the maximum MUA (Fig. 4.5D) of Up states along the area covered by the array. The outcome of these interpolations was continuous strips overlapping with the EPS density (Fig. 4.5E).

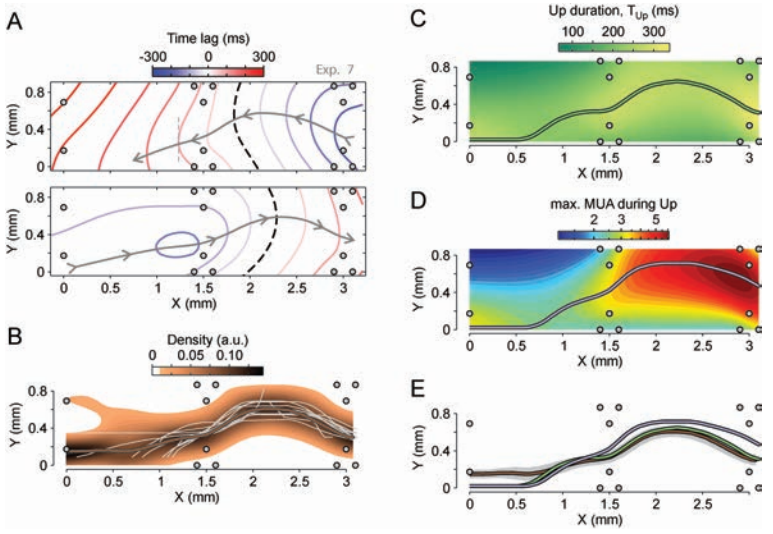

FIGURE 4.5: **Up state properties match spatial dynamics of SO.** A. Same as in figure 4.4 C for two different example waves. Dotted lines, early propagation strip (EPS); arrows propagation direction. B. Density of EPS. Gray lines, EPS of each wave cluster traveling along X direction. Brown thick line, average EPS from the wave clusters. C. Interpolation of Up state duration. Green thick line, maximum Up state duration at different X. D. Interpolation of maximum MUA of Up state. Cyan thick line, maximum MUA at different X. E. Superimposed average EPS, maximum Up and maximum MUA from plots B-D.

Altogether, these results elicited the maximum level of excitability at infragranular (IG) layers, which should correspond with the role of layer 5 on leading the generation of SO (Sanchez-Vives and McCormick, 2000; Wester and Contreras, 2012, Capone et al., *under review*). To verify whether neurons in layer 5 were the first to activate with respect to others within the same column, slices were Nissl stained and layer limits determined based on density and size of cells bodies. Then, we overlapped the laminar structure and the EPS density to further quantify the area covered by the EPS. The result was a major

overlapped with layer 5, the area exhibiting the maximum MUA and longest Up states. When comparing EPS area overlapping the different layers, layer 2/3 and layer 6 values were significantly lower than the ones obtained for layer 4 and layer 5 (Fig. 4.6).

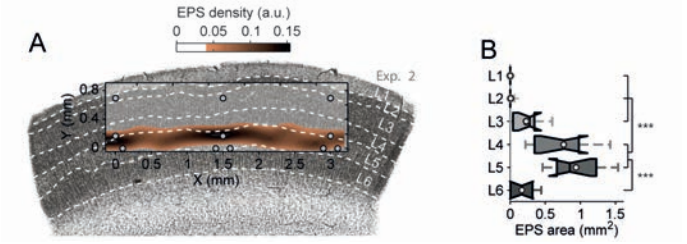

FIGURE 4.6: **Structure shapes propagation.** A. Particular example of EPS density superimposed to the corresponding slice with layers limited. B. Average values of EPS area covering every layer of the total slices stained (n=9).

These observations suggest that layer 5, together with layer 4 determine the propagation across columns with its structure (Capone et al., *under review*).

4.1.3 Excitability level for a regular propagation pattern

The next objective was to determine how excitability modulates the spatiotemporal regularity of slow waves. To act on the excitability of neuronal networks it is needed to modify the resting membrane potential of neurons, which is mainly controlled by K^+ equilibrium potential. Thus, variations in the extracellular K^+ concentration lead to changes in the neuronal population excitability. With that purpose I modified the extracellular K^+ level from 1 mM to 7 mM on 13 slices. This variation in the extracellular K^+ concentration led to an increase in the excitability of the network, which is represented by the standard deviation of the Down states log(MUA) (Fig. 4.7A). In addition, this increase in the global excitability was associated with an increase in the occurrence of Up states as expected (Fig. 4.7B). Then, we quantified the variability induced on the Up/Down cycle by such increased excitability computing coefficient of variation (CV). In this case however, there was not an increase with increasing K^+ levels, instead a minimum variability appeared at intermediate levels of excitability for SO frequency

in all the slices (Fig. 4.7C). The concentration at which CV displayed the minimum value varied between K^+ 3 and 4 mM, this variability was due to differences in the basal excitability level across slices; for that reason values were normalized, we calculated z-score of the CVs and aligned the level of K^+ placing the minima at zero. Average values for Up/Down cycle CV and Down state duration CV showed the minimum variation for intermediate K^+ concentrations, while Up states duration did not show any significant variation with distinct K^+ concentrations (Fig. 4.7D-E), meaning that it was less dependent on the network excitability (Sancristóbal et al., 2016).

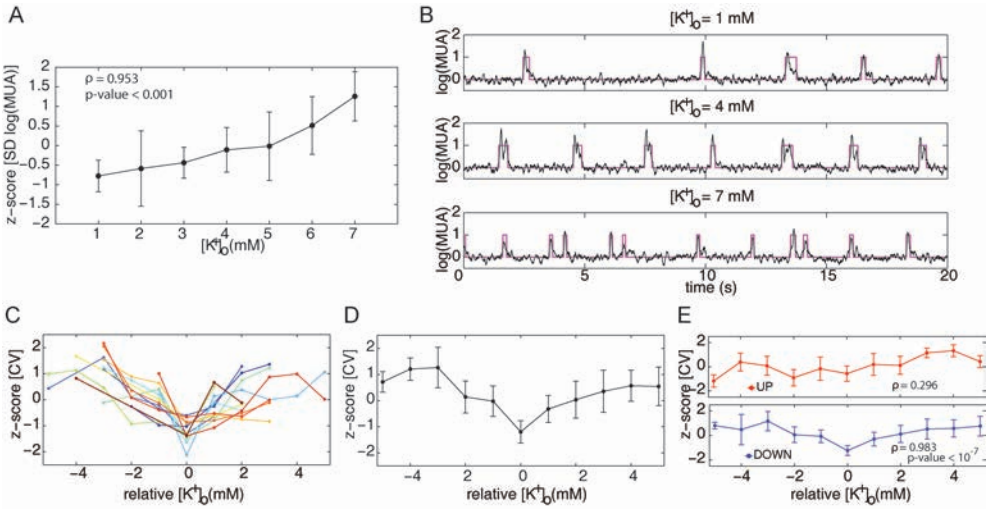

FIGURE 4.7: **Effect of extracellular K^+ concentration on the SO.** A. Standard deviation of log(MUA) during Down states under different K^+ level. B. Example of log(MUA) traces under three different K^+ concentrations. C. CV of SO cycle frequency versus relative K^+ concentration for 13 individual cases. D-E. Average CV of SO cycle frequency and Up/Down duration (red/blue), respectively. Error bars, standard deviation. Adapted from *Nature Physics* (Sancristóbal et al., 2016).

Knowing that an intermediate excitability level originates regular rhythmic SO *in vitro* with a low temporal dispersion (i.e minor CV of cycle duration). Next, we took advantage of the simultaneous recording obtained with the 16-electrode array, being able to explore spatial dynamics of slow waves under the same conditions. Thereby, for each K^+ concentration we studied the

regularity of the Up state propagation, quantified here as spatial consistency (SC) (see *Materials and Methods*). This measure revealed an irregular propagation of Up states for low and high K^+ levels, while a well-defined spatial pattern appeared for intermediate concentrations. Color plots for a particular example under three different K^+ concentrations are shown on figure 4.8A, clearly displaying more than 60% consistency (red areas) at 4 mM concentration. Indeed, population average values showed that this spatial consistency was negatively correlated with the temporal CV of the SO cycle (Fig. 4.8B).

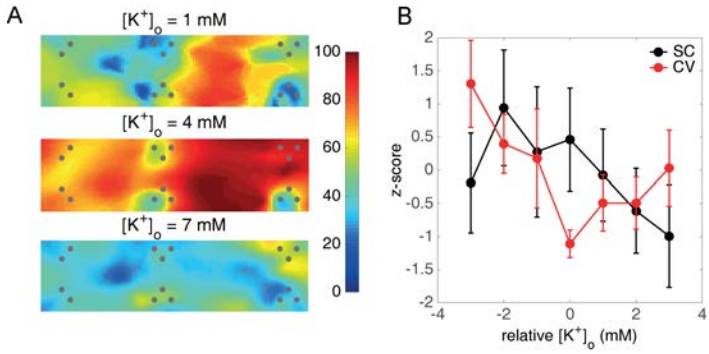

FIGURE 4.8: **Spatial Consistency.** A. Spatial consistency of the average wavefronts color-coded (percentage) for a particular slice under three different excitability levels. B. Average z-score values for the spatial consistency (SC) and the coefficient of variation (CV) from 8 slices. Error bars, standard deviation. Adapted from *Nature Physics* (Sancristóbal et al., 2016).

These results point out that an intermediate level of excitability in the neuronal population leads to the highest spatiotemporal regularity of slow waves, a phenomenon that is called stochastic coherence. Stochastic coherence has been described in individual neurons but hardly as a network phenomenon, which is a novelty reported here as a mechanisms for Up/Down cycle dynamics (Sancristóbal et al., 2016).

4.2 Electric field propagation of slow waves

The previous section showed how synaptic transmission is the main mechanism for the generation and spreading of SO in the cortical network. However, previous studies reveal that neural population activity generates endogenous electric fields (EFs), which in turn have an effect on local and distant neurons and their synaptic transmission (Fröhlich and McCormick, 2010; Anastassiou et al., 2011; Zhang et al., 2014). Thus, our next purpose was to dissect the synaptic from the EF propagation of slow waves. We performed a complete cut of the slice perpendicular to cortical layers in 73 slices while both sides remained in close contact (Fig. 4.9A). Sectioning the slice often resulted in two independent networks with different oscillatory patterns as can be observed on figure 4.9A. For this particular case, raw LFP traces from the left site (black), displayed slower oscillatory frequency than the ones from the right (red traces). Their respective autocorrelograms on the right represent more clearly the differences in periodicity between both sites.

4.2.1 Slow wave propagation between disconnected columns

The presence of two independent networks confirmed the existence of interrupted synaptic connectivity between cortical columns, along with the fact that at the end of the recording it was always checked that they were two totally independent pieces of cortex. Under this scenario, we observed that spontaneous Up states could be recorded across the cut albeit with a large decrease in amplitude (Fig. 4.9 B-C).Such decrease in amplitude represented the dimensionless measure known as *damping*, a property shared by different spontaneous and evoked responses when propagating across the two independent networks. We will refer to damping as the percentage remaining from the original Up state. Figure 4.10 exhibits four individual examples: a spontaneous Up state (black), an evoked Up state with glutamate (blue), an evoked glutamate response (green) and a spontaneous epileptiform event (red). Epileptiform activity was induced by bath applying the $GABA_A$ blocker bicuculline (2.4-3 μM)(see *Materials and Methods*). Blockade of inhibition resulted in large events that, although they were reduced to less than a 10% due to the EF propagation, the waves at the other side of the cut were easily detectable (Fig. 4.10A, bottom)(Gonzalez-Andino et al., *under review*).

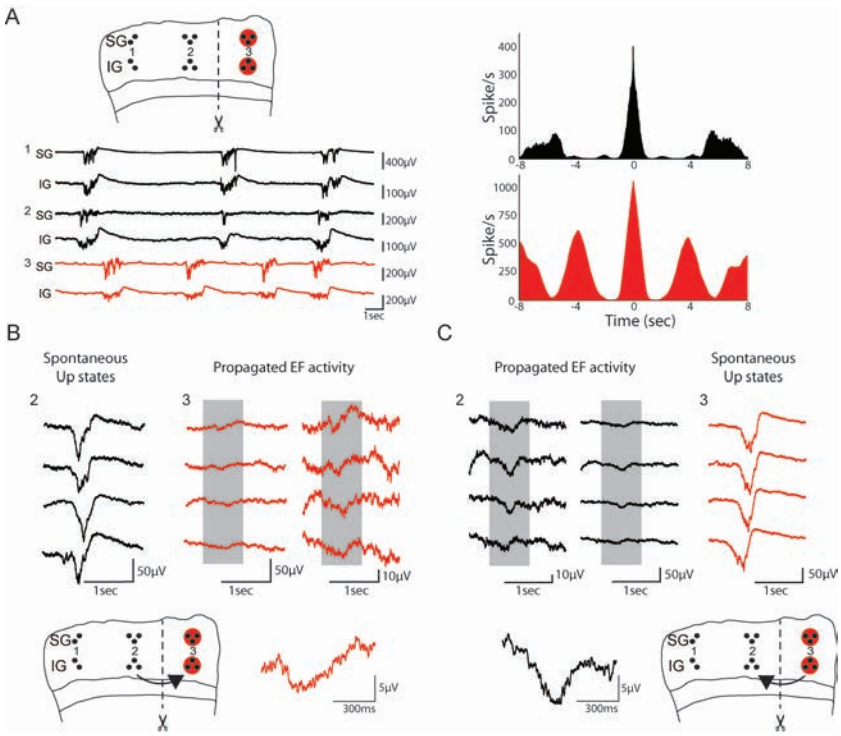

FIGURE 4.9: **EF propagation of slow waves.** A. Left, raw LFP traces from supragranular (SG) and infragranular layers (IG) at the three different locations indicated on the top scheme. Right, autocorrelograms of the multiunit activity recorded at location 2 IG and 3 IG showing two different patterns of activity. Black, left side of the slice; red, right side of the slice. B. Top, 4 spontaneous Up states recorded at location 2 and the simultaneous EFs originated at location 3 (the other side of the cut). Traces amplification on the most right. Bottom, four waves averaged of the shadowed periods (800ms). C. Same as B for the opposite direction.

Voltage cross-correlations over time between the recorded signals at both sides showed their maximum values with delays (Fig. 4.10B). Besides, in cases where fast components occurred (Fig. 4.10A blue and red, asterisks), these were filtered clearly showing the distortion that characterized EF propagation across disconnected networks. Delays and distortions represented on figure 4.10 examples were consistent across repetitions and slices. In particular, mean cross-correlation for epileptiform responses, within the 250ms following the onset of the original signal, was low (mean max CC = 0.33 $\pm$ 26, n = 7

slices), corresponding to the damping that characterizes EF waves propagation (Gonzalez-Andino et al., *under review*).

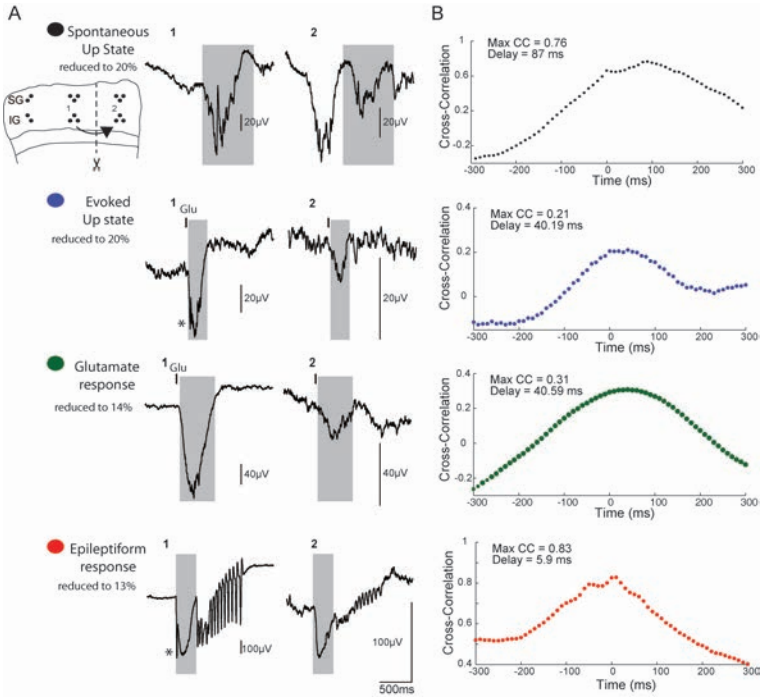

FIGURE 4.10: **EF propagation of spontaneous and evoked activity.** A. Four different responses originated at site 1 and propagating across the cut to site 2 (spontaneous Up states (black), evoked Up states with glutamate (blue), evoked glutamate responses (green) and spontaneous epileptiform events (red). B. Cross-correlation of both signals over the shadowed period (800ms, 300ms, 550ms and 320ms respectively). Colour code as in A.

4.2.2 EF propagation of slow waves to a TTX-blocked network

Hitherto, the described EF propagation took place between two different networks synaptically active. This could lead to interactions between EF and synaptic activity. An example of this phenomenon is illustrated in figure 4.11A, where the first Up state on site 1 (indicated with an asterisk) might be the synaptic reverberation blended with the EF wave of the glutamate response evoked at 2 (black traces). To avoid these episodes we applied tetrodotoxin (TTX) (30 μM) locally on the side where the EF was recorded in

7 slices. TTX prevents synaptic activity by blocking sodium conductances. The result was suprathreshold activity abolished on site 1 (green traces) while glutamate responses kept on being evoked on site 2 (gray traces) (Fig. 4.11B). The associated EF waves remained with the same amplitude before and after TTX application (mean p=0.21, t-test) (Fig. 4.11C-top). Moreover, average cross-correlations value between EF waves before ana after TTX application was highly significant (0.91 ± 0.6) without varying the delay with respect to the evoked glutamate response at site 2.
For the example illustrated in figure 4.11, EF waves propagated with a delay of 104 ms. Overall the 7 slices where synaptic activity was blocked, time lags (between the evoked glutamate responses and their respective EF waves) were practically equal before and after TTX application (92.2 ± 17 ms and 96.4 ± 23 ms, respectively; p=0.23, t-test).

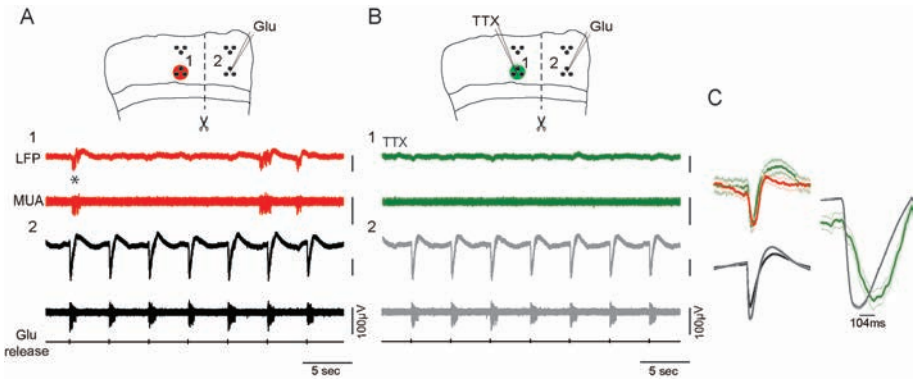

FIGURE 4.11: **EF propagation to a TTX-blockade network.** A. Raw LFP recordings (top traces) and their respective multiunit activity (MUA, bottom traces) at both sides of the slice (sites 1 and 2 on the top scheme) while evoking glutamate responses at site 2. B. Same as in A when applying TTX at site 1. Notice how spontaneous SO and multiunit activity disappear only in one side due to the local synaptic blockade (green). C. Left, average responses from A and B recordings superimposed for each side (standard errors overlaid). Right, delays between site 1 and 2 after TTX application.

Additionally, to explore if the cut was acting on the damping and delays previously described, we blocked synaptic activity at the same side where the glutamate was evoked (Fig. 4.12). By doing this we could compare the EF propagation within pharmacologically and physically synaptic-disconnected

networks. Glutamate responses were induced at site 2 (black traces) while local TTX applications were delivered at site 1, the result was similar damping at both sites (1 and 3) (Fig. 4.12A gray and green traces). Those similarities were maintained when blocking synaptic activity in the disconnected network (site 3) (Fig. 4.12B).

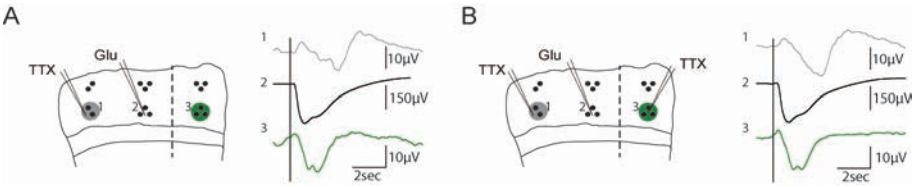

FIGURE 4.12: **EF similarities between a pharmacologically and a physically disconnected network.** A. Average waveform of the responses recorded at the three sites when blocking synaptic activity and evoking glutamate responses at the same side of the cut (but different site, TTX at site 1 and glutamate at site 2). B. Same as in A with synaptic activity abolished at the other side of the cut (site 3).

Altogether, these data suggest that EF propagation across cortical columns was not contaminated by spontaneous synaptic activity, it propagated independently within the tissue. Besides, the interface created by the cut between the two non-connected networks had no role on the damping and delays that characterize the EF propagation (Gonzalez-Andino et al., *under review*).

4.2.3 Distortion, delays and speed: characterizing endogenous EF propagation

As we have described, slow waves propagation mainly occurred within layer 4 and layer 5 matching their structures, with onsets of Up state variable in time.

Regarding non-synaptic propagation, to characterize the influence of the cortical structure in the EF propagation it is better to exactly know the spatiotemporal origin of the response that leads such EF activity. With that purpose we used glutamate-evoked responses, which represent postsynaptic activation of a limited population of neurons. Glutamate responses can be of

different amplitude depending on the amount applied, from a small response that recruits an Up state to a large response (Sanchez-Vives and McCormick, 1997; Sanchez-Vives et al., 1997, 2008). These triggered events have the advantages of being a controlled rather than a spontaneous event, and thus to measure them in a precise time window; as well as, to control the exact location where they have been generated.

We measured how different parameters of the mean EF-propagated glutamate responses varied depending on the stimulated and the recorded layer (Fig. 4.13A). Specifically, we computed duration, amplitude and distortion (peak compression/widening), and speed. Significant differences were observed between EF waves recorded and coming from different layers (Fig. 4.13 and 4.14).

EF waves recorded at SG layers (blue) were significantly narrower and smaller than EF waves recorded at IG layer (red) in both cases: when glutamate responses were evoked at SG (EF wave at SG: 4.86 $\pm$ 3.01 μV and 0.33 $\pm$ 0.02 s; EF wave at IG: 15.31 $\pm$ 8.13 μV and 0.4 $\pm$ 0.02 s) (hollow bars) and when glutamate responses were evoked at IG layers (EF wave at SG: 3.94 $\pm$ 5.41 μV and 0.34 $\pm$ 0.01 s; EF wave at IG: 25.54 $\pm$ 6.10 μV and 0.41 $\pm$ 0.01 s) (full bars) (Fig. 4.13 B-D).
Distortion was measured by computing the compression and widening of the peak. Positive values represent compression of the wave when propagating across the cut, while negative values represent widening (see *Materials and Methods section*). Only when EF propagated from IG layers to synaptically disconnected SG layers was there compression in the waves (0.05 $\pm$ 0.05) (Fig. 4.13E). While when glutamate responses propagated across the cut from SG layers to IG layers signals widened (Fig. 4.13E).
Finally, significant differences were observed between duration, amplitude and distortion of the EF wave propagation within SG layers (blue hollow bars) and IG layers (full red bars) (Fig. 4.13C-E).

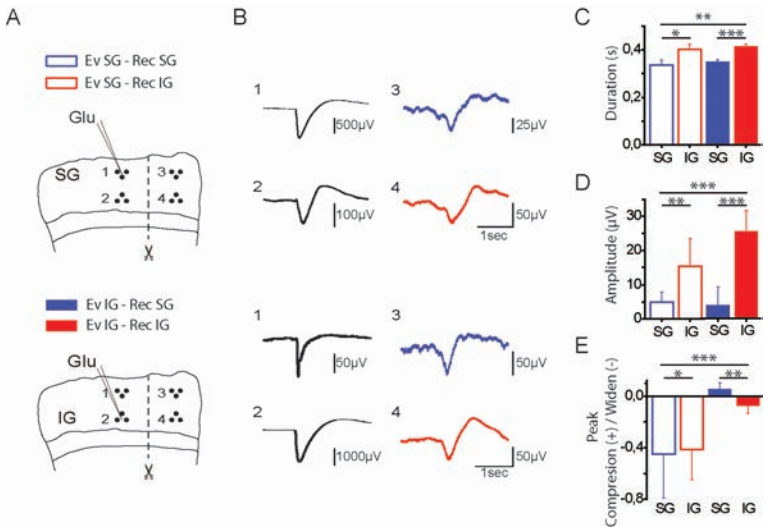

FIGURE 4.13: **Distortion of endogenous EF propagation.** A. Schematic of the recording configuration. Top, glutamate responses evoked at supragranular layers (Ev SG); bottom, glutamate responses evoked at infragranular layers (Ev IG). B. Average responses at the four sites indicated in A for a particular slice. C-E. Population averages displaying significant differences on duration, amplitude and distortion (respectively) of EF waves on 12 slices. Hollow and full bars indicate evoked responses at SG and IG layers, respectively. Blue and red indicate EF waves recorded at SG and IG layers, respectively. $^{*}p \leq 0.05$, $^{**}p \leq 0.01$,$^{***}p \leq 0.001$;t-test or Mann-Whitney U test.

Considering propagation speed, there was no significant differences between locations where the glutamate responses were induced. But, when the glutamate response was originated at IG layers, it propagated significantly faster to the same layer across the cut than to SG layers (15.7 ± 10.15 mm/s to IG, 9.5 ± 19.57 mm/s to SG) (Fig. 4.14 C, bottom). Moreover, we observed that EF velocity, despite showing significant difference with synaptic transmission velocity (EF: 18.3 ± 2.85 mm/s; synaptic: 13.6 ± 2.70 mm/s; $p<0.001$, Mann-Whitney U-text), was the same order of magnitude (mm/s) instead than instantaneous as volume conduction transmission (Gonzalez-Andino et al., *under review*).

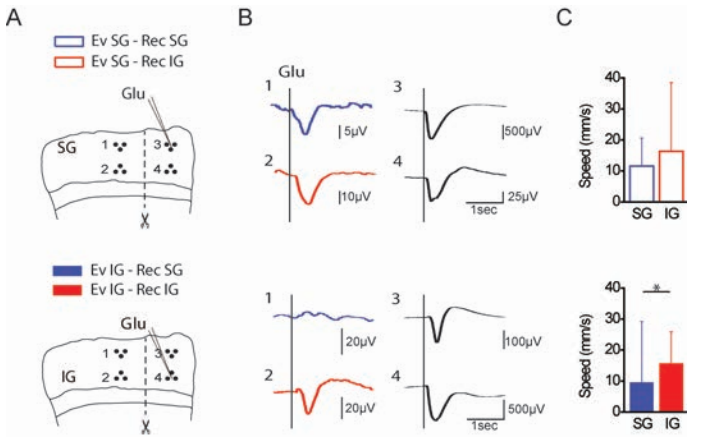

FIGURE 4.14: **Speed of endogenous EF propagation.** A-B. Same as in figure 4.13A-B, showing the time trigger of the glutamate application to better display delays. C. Speed population averages of the EF propagation when inducing the glutamate response at supraganular (SG, top) and infragranular (IG, bottom) layers of 12 slices. Bar code as in figure 4.13 $^{*}p \leq 0.05$, $^{**}p \leq 0.01$,$^{***}p \leq 0.001$; t-test or Mann-Whitney U test

4.2.4 Slow wave activity and its EF propagation within a disrupted laminar cortical structure

To further explore whether changes in the laminar cortical structure influence the interaction between synaptic and EF activity, one side of the slice was rotated. Such manipulation was done after cutting the slice in the interface chamber as previously described, and the right side of the slice was gently overturned 180°so that SG layers were next to IG layers and vice versa (Fig. 3.3 and 4.15A), care was taken that there was close contact. This configuration caused an abrupt change in the structure of the tissue, resulting in a sectioned cortical slice where one side had an inverted laminar structure. This was done in 6 slices where this protocol was performed.

Even when we investigated in detail any possible influence of the cortical structure disruption on the SO parameters, we did not detect any influence on the frequency oscillatory pattern from one side to the other. The main changes were observed in the characteristics of Up states, which were inverted with respect to layers on the right side. Interestingly, in the inverted side (site

2), there was a trend towards longer Up states in SG layer than in IG layers (SG: 0.42 $\pm$ 0.04 s; IG: 0.36 $\pm$ 0.05 s) (Fig. 4.15B), which is the opposite of a very consistent observation in physiological conditions where Up states at IG layers are longer (SG: 0.37 $\pm$ 0.05; IG: 0.39 $\pm$ 0.05 s) (Fig. 4.17Bb-Cb gray bars). The same phenomenon occurred with mean firing rates, which trended to be higher in SG layers than in IG layers on the right side (SG: 0.40 $\pm$ 0.03; IG: 0.38 $\pm$ 0.01) (Fig. 4.15C), as well as with maximum firing rates (SG: 1.68 $\pm$ 0.18 IG: 1.35 $\pm$ 0.25)(Fig. 4.15D). Although significant differences were not observed, a trend to elicit opposite behaviors can be noticed between both sides.

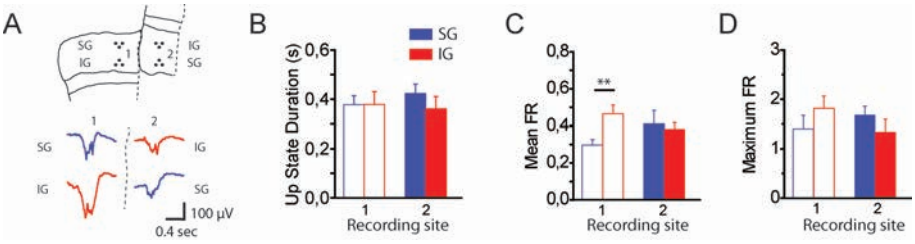

FIGURE 4.15: **Effect of layer inversion on SO.** A. Top, schematic of the recording configuration. Bottom, representative Up state at each recording site. (B-D) Mean average values of Up state duration, mean firing rate and maximum firing rate from 6 slices. Mean and maximum firing rate are the absolute values of Up state computed from the transform log MUA (see *Materials and Methods*) ($^{**}p \leq 0.01$; Paired student t-test).

We next explored the influence of the cortical structure on the propagation of endogenous EF waves. For this, we used spontaneous Up states at IG layer on site 2 (Fig. 4.16A) as the reference responses that led to EF waves at the other side of the cut (sites 3 and 4 in figure 4.16A). Interestingly, rotating the right side of the slice led to amplitude values of EF waves that trended to be larger in SG layers (site 4 in figure 4.16A) than in IG layers (site 3 in figure 4.16A) (SG: 19.67 $\pm$ 9.2 μV; IG: 17.89 $\pm$ 11.23 μV) (Fig. 4.16A-B). This tendency observed in sectioned slices where one side was rotated (larger amplitude in SG than in IG layers) was the opposite to the tendency observed in sectioned slices where there was no rotation (larger amplitude in IG than in SG layers). Duration and peak compression of EF waves elicited a similar tendency in both sectioned slices (with and without rotated side): IG layers showed EF waves with longer duration than the EF waves in SG layers (Fig. 4.16C), and

EF waves widened at IG layers and were compressed at SG layers (Fig. 4.16D).

The same tendency in the characteristics of EF waves were observed in three slices (with the right side rotated) where glutamate responses were induced to better control the origin of the response. From these three cases we could compute the speed of propagation from the peak to peak delays that turned out to be similar between layers (from SG to IG: 19.35 $\pm$ 9.45 mm/s; from IG to SG: 18.98 $\pm$ 9.19 mm/s) (not shown), and in the same range measured for the larger population presented in previous section (4.2.3).

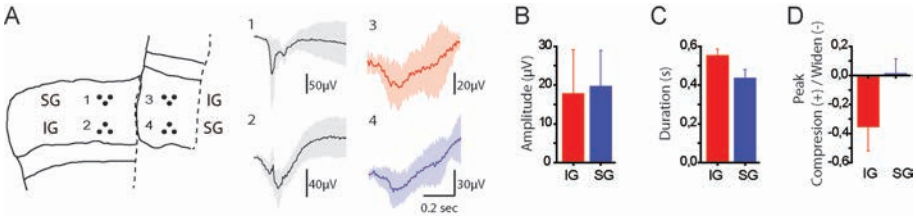

FIGURE 4.16: **Effect of layer inversion on EF waves** A. Left, schematic of the recording configuration. Right, waveform average responses at the four indicated sites. B-D. Mean values of amplitude, duration and peak compression from 6 slices. Blue, supragranular layer (SG); red, infragranular layer (IG).

In summary, the reversion observed in the amplitude of the recorded EF waves (larger in SG than IG layers), together with the resulting damping (29,06 $\pm$ 38,68 % from SG to IG, and 52.2 $\pm$ 18.07% from IG to SG) suggests some dependence of these parameters on the local network where the EF wave is originated, and not only on the network where it is recorded.

4.2.5 Influence of extracellular space on slow waves and its EF propagation

To study the influence of extracellular space on the synaptic and non-synaptic mechanisms of SO, we increased the osmolarity of the ACSF, which is known to expand the extracellular space (Traynelis and Dingledine, 1989).
For this, saccharose (40 mM) was added to the ACSF solution to increase by

12% the osmolarity (from 328 to 368 mOsm). Similar increases with other agents have been proved to decrease synaptic and non-synaptic activity (Shahar et al., 2009; Zhang et al., 2014; Qiu et al., 2015).

Spontaneous SO (<1Hz) in normal ACSF solution (328 mOsm) displayed Up states, (0.39 $\pm$ 0.05 s duration) interspersed with Down states (3.47 $\pm$ 0.86 s duration) in IG layers. Up/Down cycle frequency was 0.33 $\pm$ 0.06 Hz.

Increases in osmolarity resulted in alterations in the Up and Down states at SG and IG layers (Fig. 4.17). Although significant differences were only observed in the oscillatory frequency, which decreased from 0.33 $\pm$ 0.06 Hz in control condition to 0.17 $\pm$ 0.02 in the hyperosmolar condition ($p < 0.05$) (Fig. 4.17 Be), changes in other parameters were non significant but consistent (observed in 6 out of 7 slices). Up and Down state durations tended to increase, from 0.39 $\pm$ 0.05 s to 0.54 $\pm$ 0.1 s; and from 3.47 $\pm$ 0.86 s to 6.31 $\pm$ 1.44 s, respectively (Fig. 4.17 Ba-c). These changes in the Up/Down cycle dynamics led to a more irregular slow oscillatory pattern: the coefficient of variation (CV) of the SO frequency increased (control: 7.03 $\pm$ 3.22, hyperosmolar: 31.89 $\pm$ 21.33) (Fig. 4.17 Bd).
In spite of this reduction in the capacity of the network to generate Up states, there was an increase in mean firing rate during Up states (from 0.45 $\pm$ 0.04 under 328 mOsm, to 0.56 $\pm$ 0.09 under 368 mOsm), as well as in maximum firing rate (from 1.89 $\pm$ 0.2 under 328mOsm, to 2.47 $\pm$ 0.28 under 368mOsm) (Fig. 4.17 Be-f). Up/Down cycle variations reported here, which refer to IG layers, elicited similar variation as the ones obtained in SG layers (Fig. 4.17C).

These results suggest that slightly increasing osmolarity altered the excitability of the network, thereby decreasing the frequency of oscillations.

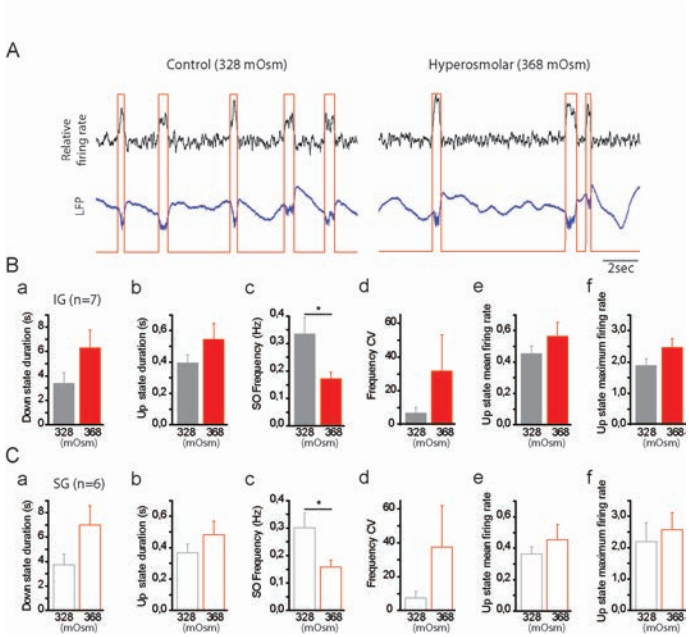

FIGURE 4.17: **Effect of hyperosmolar ACSF on SO.** A. One example under control (328 mOsm) (left) and hyperosmolar (368 mOsm) ACSF (right). Relative firing rate (top) and LFP recording (bottom). The red line represents the Up and Down states detection. B. Average population data for the two conditions (control: gray; hyperosmolar: red) showing variations in the different parameters in infragranular (IG) layers when increasing osmolarity by 12% in 7 slices. a, Down state duration. b, Up state duration. c, SO frequency. d, SO Frequency CV. e, Up state mean firing rate. f, Up state maximum firing rate. C. Same as in B for supragranular (SG) layers in 6 slices. $^{*}p \leq 0.05$; Paired student t-test vs. control).

Our main objective was to study the influence on the EF induced by Up states across the cut. Regarding EF propagation of spontaneous Up states in a hyperosmolar medium, we observed similar damping as previously reported (20.45%) in section 4.2.1. When computing average amplitude values of EF waves, these were significantly reduced with respect to the control condition (328mOsm, 15.24 $\pm$ 2.8 μV; 368 mOsm, 7.5 $\pm$ 1.9 μV at IG layers) (Fig. 4.18A-B). Such reduction was due to a decrease in amplitude of the original LFP signal (328mOsm, 56.37 $\pm$ 9.4 μV; 368 mOsm, 37.47 $\pm$ 2.8 μV). Significant differences were also observed in peak compression: spontaneous

Up states were compressed when propagating across the cut under the control condition (0.39 ± 0.16 at SG, 0.27 ± 0.09 at IG), while they were widened in an expanded extracellular medium (-0.08± 0.11 at SG; -0.15 ± 0.05 at IG) (Fig. 4.18D).
When computing time delays from peak to peak in four slices, EF waves in SG layers displayed slower velocities under a hyperosmolar medium (10.22 ± 3.9 mm/s with 328 mOsm versus 8.39 ± 3.21 mm/s with 368 mOsm) while EF waves in IG layers remained similar (10.47 ± 4.09 mm/s with 328 mOsm versus 10.52 ± 1.98 mm/s with 368 mOsm) (Fig. 4.18E).
A similar decrease in EF wave propagation was observed in three slices under a hyperosmolar medium where glutamate responses were evoked (not shown).

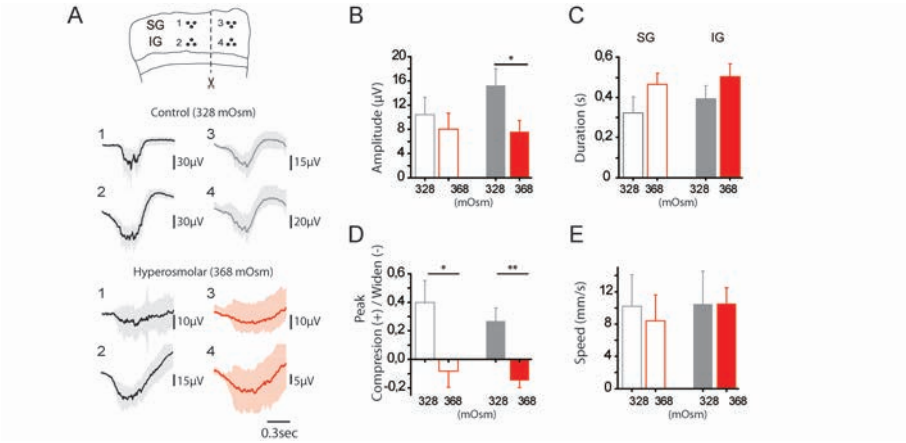

FIGURE 4.18: **Effect of hyperosmolar ACSF on EF propagation.** A. Schematic of the recording configuration (top). Average responses at the four sites indicated in the scheme (middle and bottom). B-E. Mean values of amplitude, duration, peak compression and speed from 6 slices. (Hollow bars, supragranular layer (SG); full bars, infragranular layer (IG).

By expanding the extracellular space we were able to decrease EF propagation of slow waves. Similar observations have been made with epileptiform bursts caused by 4-aminopyridine (Zhang et al., 2014; Qiu et al., 2015) or low-Mg^{2+} (Shahar et al., 2009) in hippocampal slices.

4.2.6 Influence of external EF stimulation on slow waves and their EF propagation

Next, we explored the influence of external EF stimulation on the endogenous EF propagation of slow waves. Previous studies have used external EF stimulation to mimic endogenous fields (Fröhlich and McCormick, 2010); here we have already disconnected the endogenous fields from the synaptic activity, thus we have used the exogenous EF to modulate the network excitability and affect the detectability of endogenous EFs.

Therefore, uniform external EFs were applied by direct current (DC) stimulations through two parallel AgCl electrodes in 8 sectioned slices (Fig. 4.19B). It is widely known that positive DC stimulation induces somatic depolarizations that lead to an increase in the excitability of neurons (Fröhlich and McCormick, 2010; Schmidt et al., 2014). Thus, we applied DC stimulation with increasing intensities (from -4 V/m to +4 V/m) which enhanced the frequency of SO cycle at both sides of the cut without having any relevant effect on spontaneous Up state properties (Fig. 4.19), as reported in previous studies (Sanchez-Vives et al., 2017a).

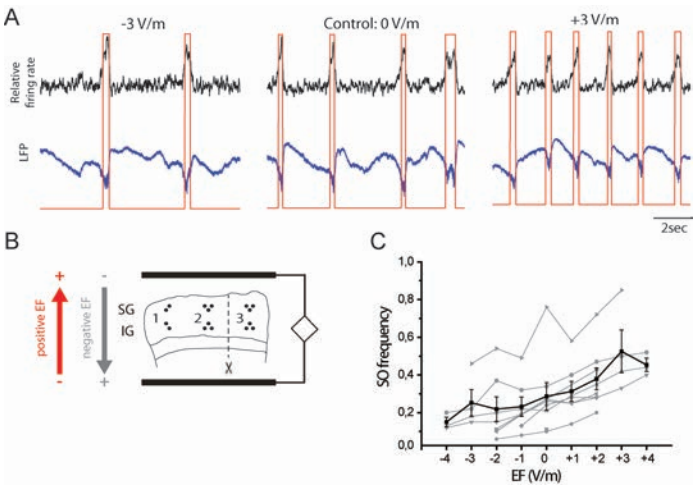

FIGURE 4.19: **Effect of EF stimulation on SO.** A. One example of Up/Down state detection (red lines) under two different intensities of EFs (left, right) and in a control condition (0 V/m). Relative firing rate (top) and LFP recording (bottom). B. Schematic of the recording configuration with the two AgCl electrodes parallel to the apical surface. C. SO frequency increase for different EF stimulations (gray, individual cases; black, average values from 8 slices).

Our hypothesis was that increasing DC stimulation would result in larger EF waves that could increase the probability of inducing suprathreshold responses. According to the results described before (section 4.2.4 and 4.2.5) suggesting that the EF wave amplitude depends on the original signal where it comes from, the absence of effect on Up states amplitude and duration with DC stimulation led to no differences in EF waves traveling across the cut. Figure 4.20 shows the lack of a clear variation or tendency in amplitude, damping, duration and peak compression of EF waves with increasing DC stimulation (similar results observed with glutamate responses) (not shown).

According to our hypothesis (see above), DC stimulation could be driving the EF wave to induce suprathreshold responses, hence contributing to the generation of Up states in the disconnected network. In this case, these suprathreshold responses would have been discarded according to analysis criteria (periods with Up states overlapped from both sides were removed from the averaged EF waves) (see *Materials and Methods*). However, we found

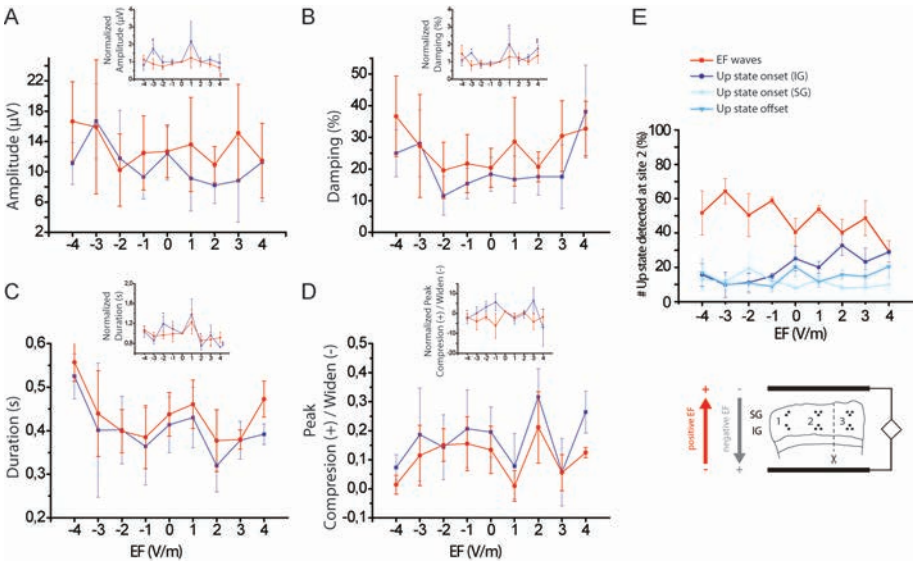

FIGURE 4.20: **Effect of external EF stimulation on endogenous EF waves.** A-D. Amplitude, damping, duration and peak compression of EF waves at site 3 shown in E (bottom). Insets, normalized data with respect to control (0 V/m) values. Blue, supragranular layers (SG); red, infragranular layers (IG). E. Top, line plot showing the percentages of Up state detected at site 2 that led to EF waves (red), and that overlapped with Up states onset/offset at site 3 (blue). Bottom, schematic of the recording configuration.

that from all Up states recorded on site 2 the majority did not overlap with Up state onset or offset on site 3; in fact, most of them were recorded with similar damping at the other side of the cut (Fig. 4.20 E). Thus, against our hypothesis, enhanced excitability did not result into higher probability of inducing suprathreshold responses.

4.3 Endogenous electric fields modulate the occurrence slow oscillations

So far, the results described previously in this thesis demonstrated that propagation activity of SO and the EFs that they generate coexist in the neural tissue. Past studies demonstrated that external EFs are able to entrain

neocortical network activity (Fröhlich and McCormick, 2010; Anastassiou et al., 2011). Taking advantage of our *sectioned in vitro* preparation, where synaptic and endogenous EFs can be disassociated, we next explored the interaction of activity across the two synaptically disconnected networks.

4.3.1 Synchronizing two synaptically disconnected networks with external EF stimulation

Synchronous Up states at both sides of the cut could occur randomly. We wanted to test whether enhancing excitability with exogenous EFs would increase SO synchronization between both sides of the cut. To study whether there was any modulated synchronization across both disconnected networks, we computed cross-covariation coefficients between site 2 (IG) and site 3 (IG) (Fig. 4.19B) under control conditions (no stimulation applied) and with different intensities of DC stimulation (negative and positive) in 8 slices. Hence, we obtained the cross-covariation coefficient that corresponds to the cross-correlation between both sides where the mean had been subtracted. Even though DC stimulation increased the cross-covariation coefficient, the only value significantly different from the control condition (0 V/m) was at -1 V/m.

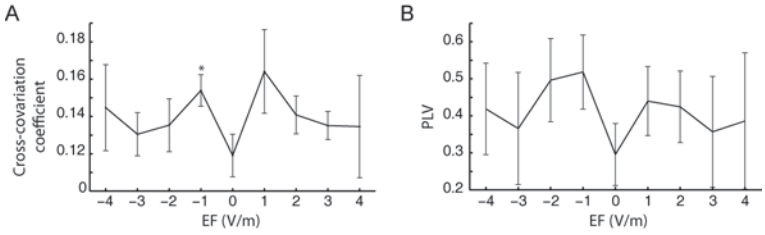

FIGURE 4.21: **Synchrony between disconnected cortical columns at different EF stimulations.** A. Mean cross-covariation coefficients between two selected channels from both sides of the slice at different EF intensities in 8 slices. B. Same as A for phase-locking values (PLV).

As changes in the cross-covariation coefficient were too small, we looked for a more sensitive measurement such as the phase locking value (PLV), which is a statistical measure used to study synchronization of neural activity. The PLV computed between site 2 (IG) and site 3 (IG) led to similar results as the cross-covariation coefficient: higher values with DC stimulation however not significant (Fig. 4.21B).

Although, a linear relationship in average PLV was not observed with increasing DC stimulation, it is worth to note the results for low EF stimulations (± 1 V/m), which suggest that DC electric stimulation of low intensity may be enough to synchronize two independent networks.

4.3.2 Modulation of subthreshold glutamate-induced responses by endogenous EF

We have shown above that DC stimulation on both sides of the slice modulates excitability. However, the increase in excitability with increasing DC stimulation did not result in an enhanced synchronization of spontaneous SO between both disconnected networks. To further explore the possibility of inducing SO in spite of the interrupted cortical synaptic connectivity, we used small local applications of glutamate to slightly increase the excitability only in one side at a desired time without evoking an Up state. I will refer to these as subthreshold responses that do not trigger Up states. This should be differentiated from the classical use of *subthreshold responses* referring to those that do not evoke action potentials.

First, small local applications of glutamate were adjusted to induce depolarization without evoking Up states on one side (side 2) (Fig. 4.22 A, top: Off-On). Next, full blown Up states (or glutamate-evoked responses) were induced on the other side (side 1). Thus, two glutamate applications were applied at the same time on both sides of the slice (on the left side to induce Up states, on the right side to locally increase excitability without evoking Up states) (Fig. 4.22 A, middle: On-On).

With this strategy we wanted to amplify the potential effect of the endogenous EF across the cut. Although endogenous EFs could not induce SO in a non-synaptically connected network even when we locally increased the excitability with small glutamate applications, they did significantly increase amplitude ($p<0.005$) and duration ($p<0.01$) of the subthreshold induced responses (Fig. 4.22 C-D, mean values from 260 waves analyzed offline with Spike2 software: 20 waves x 13 slices). These increases were reverted to control values (i.e, same values presented when adjusting the glutamate application at side 2) when the glutamate application inducing Up states on the left side stopped (Fig. 4.22 A, bottom; B-D), further confirming that the changes observed were due to the endogenous EFs generated by evoked Up states on the left side.

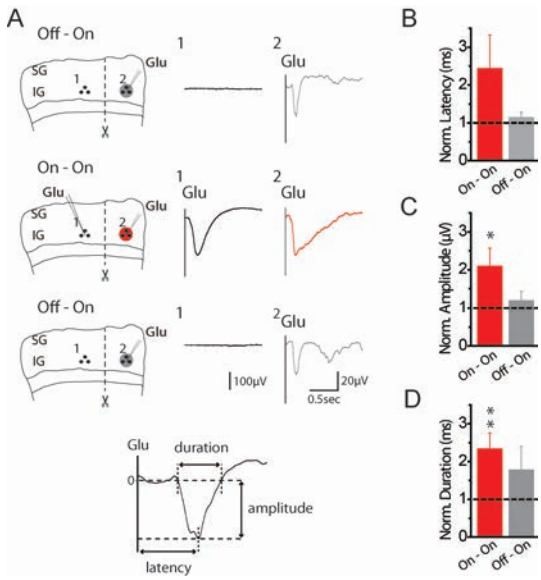

FIGURE 4.22: **Modulation of subthreshold glutamate-induced responses by endogenous EFs.** A. Induced wave responses by local glutamate application. Schematic of the recording configuration (left) and 20 averaged waves obtained from the glutamate applications at site 1 and 2 (right). Top, subthreshold responses induced at site 2 prior to glutamate response induction at site 1. Middle, responses from glutamate applications on both sides (inducing glutamate responses at 1 and subthreshold responses at 2). Bottom, subthreshold responses at site 2 after the induction at site 1. Most bottom, designated features. B,C,D. Mean values for latency, amplitude and duration (respectively) of the subtheshold response at site 2. Values are normalized to the first subthreshold response. $^{*}p \leq 0.05$, $^{**}p \leq 0.01$, $^{***}p \leq 0.001$; Paired student t-test vs. control).

4.3.3 Frequency modulation of SO by endogenous EFs

We have seen in the previous section how the endogenous EFs generated by evoked Up states modulate subthreshold glutamate-induced responses. Here, we used another strategy to detect the influence of endogenous EFs on the temporal pattern of occurrence of spontaneous SO.

So, in order to further explore the impact of endogenous EFs on spontaneous synaptic activity, we used glutamate-evoked Up states to modulate

non-synaptically the neural activity across disconnected networks. By using local glutamate applications we could control the periodicity of the Up state occurrence. Thus, different oscillatory frequencies were induced on the left side of the slice (Fig. 4.23 A-top scheme). By doing this we explored the impact on the spontaneous oscillatory frequency of the right side. Interestingly, this manipulation resulted in a frequency variation in the spontaneous SO on the right side of the cut. Increasing (decreasing) the glutamate application periodicity induced an increase (decrease) in the spontaneous SO frequency of the disconnected network (Fig. 4.23A-B).

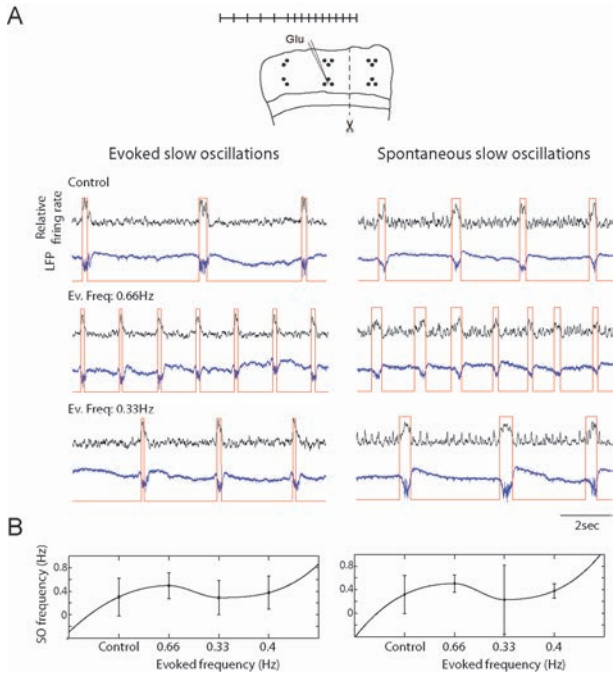

FIGURE 4.23: **Frequency modulation of spontaneous SO by endogenous EFs.** A. Relative firing rate (black), LFP recording (blue) and Up and Down state detection (red lines) for spontaneous activity (top) and two evoked oscillatory frequencies: 0.66 Hz and 0.33 Hz (middle and bottom, respectively). Left, left side on the slice; right, right side on the slice. B. Mean SO frequency from a 50-second period analyzed at four different frequencies (one control and three evoked in the following order: 0.66, 0.33 and 0.4 Hz).

We next explored the kinetics of such entrainment. To explore the time course

of the interaction, we changed the frequency on the left side and we measured the evolution of the frequency on the right. We observed that the interaction followed an exponential time course. An exponential fit was adjusted (Fig. 4.24 B - red line); the time constant τ (red dot) of this exponential fit was considered as the time that the signal took to change the frequency on the right side depending on the glutamate application on the left side (average values: 8.62 ± 5.18 s for increasing frequencies, n = 11 frequency variations - 1 outlier discarded - ; 36.15 ± 17.71 s for decreasing frequencies, n = 6 frequency variations - 4 outliers discarded - ; from a total of 12 slices, 4 slices discarded) (see *Materials and Methods*).
Because the SO cycle did not exactly reach the same frequency on both sides of the slice with glutamate applications, normalized differences of frequencies (ND) (see Eq. 3.4) were quantified at each side of the slice to better compare the frequency variations observed (see *Material and Methods*). The dispersion plot in figure 4.24 C represents the ND for the glutamate application frequency versus the ND of the spontaneous SO frequency on the right side. The result was a linear relationship between both NDs: the induced on the left side and the spontaneous modulated on the right side, with significant linear regression values ($R^2 = 0.42$, $p = 0.01$ for 22 variation in frequency; in a total of 13 slices; 3 slices where no modulation was observed were discarded) (Fig. 4.24 D).

This entrainment was also explored after disrupting the cortical layer structure by rotating the right side (in 3 slices) or increasing the extracellular space by adding saccharose (40 mM) to the ACSF solution (in 2 slices). In these two cases a clear modulation was not observed: the evoked glutamate application on the left did not induce any influence on SO frequency on the right.

In summary, endogenous EFs were able to modulate the SO frequency of a disconnected network when maintaining the physiological conditions. Disrupting the layer structure or expanding the extracellular space prevented the modulation.

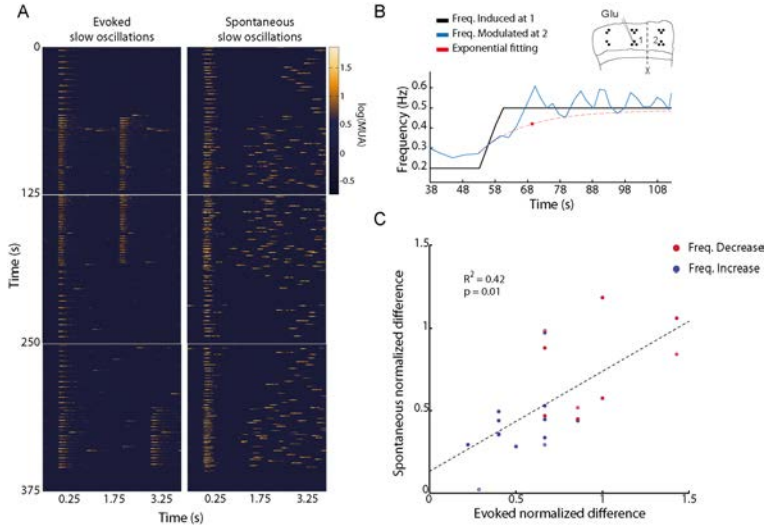

FIGURE 4.24: **Frequency modulation kinetics.** A. Raster plots of three consecutive recordings from one representative slice (375 s) for a time window of 4 s (time period covering one or two Up/Down cycles). Three frequency variations can be observed (from 0.2 to 0.5 Hz, top; from 0.5 to 0.2 Hz, middle; from 0.2 to 0.33 Hz, bottom), on the left where it is induced, perfectly defined; on the right, a clear modulation over time (from top to bottom) of the spontaneous SO. B. Exponential fit for a particular change in frequency (top in A) displaying: the glutamate application frequency (black); the spontaneous SO frequency of the disconnected network (blue) and its exponential fit displaying the τ (red dot). C. Dispersion plot of the ND at both sides of the slice. Increases in frequencies, blue; decreases in frequencies, red. (n=22 frequency variations, 13 slices)

Chapter 5

Discussion

The two major aims of this PhD work were to explore the synaptic and non-synaptic propagation of SO within the laminar cortical network. The results reported here illustrate that SO are generated spontaneously in the cortical network. Different excitability levels modulate the frequency and the spatiotemporal dynamics of the slow waves reaching the maximal regularity with intermediate excitability levels. Moreover, the propagation of these slow waves across the cortex is led by the region eliciting the maximum firing rate in the cortical structure. Further we showed that such cortical rhythm generates propagating endogenous EFs, opening the possibility to better study the conductive properties of neural tissue. Finally, these endogenous EFs have in turn a feedback effect that can further modulate the synaptic activity.

5.1 Propagation of slow oscillations

To explore local and global dynamics of the cortical network I used a 16-channel array over cortical slices which covered different cortical columns and layers allowing to study the propagation of SO, one of the most spatially synchronized rhythmic patterns within the brain (Destexhe et al., 1999). In our slice preparation different ignition sites along the cortical structure were observed, but a longitudinal strip with the maximum firing rate led to a consistent parallel propagation to the cortical surface for all the different cluster waves detected (Fig. 4.4). In humans, the slow wave propagation has different origin sites with different propagation directions within the cortex, drawing out a preference pattern of propagation from anterior to posterior areas (Massimini et al., 2004). Thus in both, coronal slices and the full cortex superficial propagation, slow waves can start at any point but there are

prefered paths for their propagation.
The propagation pattern led by layer 5 reported here agrees with the spreading of SO in deep layers described in previous studies (Sanchez-Vives and McCormick, 2000; Wester and Contreras, 2012).

5.1.1 Slow oscillations accommodate within layer 5

The experimental recordings from slices that I obtained during the course of this PhD revealed that Up states were consistently originated in and spread through deep layers of the cortical structure. Particularly, overlapping the EPS density with the anatomical slice reconstruction showed that the propagation pattern accommodated well with the structure of layer 5 and to some extent with layer 4 (Fig. 4.6). Average values of the area covered by the EPS did not show significant differences between layer 4 and layer 5, suggesting that even if layer 5 had the major contribution to the generation of SO, the neuronal population of layer 4 might also be involved in its spatiotemporal dynamics (Fiáth et al., 2016).

Layer 5 comprises a large number of synaptic connections between columns and layers within the cortex (Wester and Contreras, 2012; Beltramo et al., 2013), thus being more likely involved in the origin of SO (Sanchez-Vives and McCormick, 2000; Chauvette et al., 2010). Indeed, most animal studies have shown that layer 5 plays a key role in the origin and propagation of slow waves (Sanchez-Vives et al., 2010; Beltramo et al., 2013; Neske, 2015; Blaeser et al., 2017). In contrast, a human study reported that the superficial layers are the ones eliciting stronger multi- and single- unit activity (Csercsa et al., 2010) and thus endowing SG layers with a role in the genesis of SO. Assuming that the network structure determines how neurons synchronize with each other to generate transition network states such as the SO pattern (Blaeser et al., 2017), the differences observed between humans and rodents regarding SO generation could be due to the differences in their cortical cytoarchitecture (DeFelipe, 2011). The human cortex is thicker than the rodent one, with SG layers conforming half of the cortex, while in rodents more than half of the cortex corresponds to IG layer. If any layer can be involved in the initiation of Up states as far as its neurons have the ability to synchronize (Chauvette et al., 2010), the neuronal density of each respective layer could explain why SO are originated at superficial layers in humans and at deep layers in rodent

preparations.

Results on the propagation speed across different columns (5.5 $\pm$ 1.5 mm/s) (Fig. 4.4E) are similar to the velocities reported in past works using the same preparation, which yielded propagation speeds of 7.2 mm/s (Sanchez-Vives et al., 2010) and 10.9 mm/s (Sanchez-Vives and McCormick, 2000). However, other preparations eliciting SO *in vitro* in rat brain slices measured 20 mm/s propagation speed with voltage sensitive dye images (Wester and Contreras, 2012). This higher speed might be due to the recording technique which also examines subthreshold activity of neurons, while our LFP analysis, based on the logMUA (Fig. 4.3), only reflects suprathreshold activity of those cells.
Higher speeds appeared also in *in vivo* preparations: 23.4 mm/s in visual cortex of anesthetized mice (Ruiz-Mejias et al., 2011), and 37 mm/s within the whole cortex reported with calcium imaging (Stroh et al., 2013). The lower velocities observed in *in vitro* experiments would be explained by the elimination of long range cortico-cortical connectivity and also by the disconnection from the thalamus.

5.1.2 Slow oscillations: a collective network phenomenon

To further explore the spatiotemporal dynamics of SO within the laminar cortex, I varied the extracellular K^+ concentration to globally modulate the excitability of neurons within the network. We observed that intermediate K^+ levels maximized the temporal and spacial regularity of the SO (Sancristóbal et al., 2016). Low excitability levels decreased the probability of Up state occurrence while increasing the variability of Down state duration. With high excitability levels the occurrence of Up states increased also enhancing the variability of the SO frequency (Fig. 4.7 and 4.8).
Together these results showed the self-regulation of the cortical dynamics with different excitability levels. An intermediate amount of synaptic noise, here determined by the neuronal excitability, is needed to maximized the SO regularity, what correspond to a collective stochastic coherence phenomenon (Sancristóbal et al., 2016). A similar phenomenon has been observed in cell cultures where random firing of neurons led to a cascade of activity in neuronal populations generating coherent spontaneous activity (Soriano and Casademunt, 2015).
Also, evidence regarding SO as a network phenomenon increases when

endogenous fields are considered to be involved in the generation and maintenance of neural oscillations (Weiss and Faber, 2010)(see next section).

5.2 Endogenous electric fields generated by slow oscillations

SO have been regarded as a relevant experimental approach to investigate the interactions between endogenous EFs and synaptic activity (Fröhlich and McCormick, 2010; Reato et al., 2010; Schmidt et al., 2014). The SO represents a large spatially synchronized activity which generates endogenous EFs that, in turn, might be involved in the orchestration of such oscillatory rhythm (Fröhlich and McCormick, 2010) by inducing ephaptic coupling between neurons (Anastassiou et al., 2011).
LFP, an accessible measure widely used to study mesoscopic brain activity, is an informative signal to experimentally explore the electrical activity measured in clinical applications with EEG, magnetoencephalogram (MEG) or electrocorticogram (Buzsáki et al., 2012). LFP provides insights not only about the suprathreshold activity, but also about the subthreshold components and the charges distribution within the tissue (Herreras, 2016), here manifested as EF waves. Additionally, LFP can reflect the activity of networks that are far from the recording point (Kajikawa and Schroeder, 2011; Herreras, 2016), enabling us to measure the propagation of signals within synaptically disconnected networks located several millimeters apart. Therefore, considering all the advantages just mentioned, LFP offers a suitable and reliable measure for studying the synaptic and non-synaptic components of slow waves.

In the experimental approach used here, cutting the cortical slice in two pieces perpendicularly to the white matter, while maintaining both sides tightly in contact, yielded two independent networks with different oscillatory patterns. Importantly, the independence between both networks meant that there was no synaptic propagation of slow waves across the cut. This way, the activity (Up states) originated in one side of the cut could be recorded as EF waves at the other side. Thereby, the limitation of studying endogenous EFs with external field stimulation was overcome, and instead of measuring a mimicked or induced activity (Fröhlich and McCormick, 2010; Reato et al., 2010; Schmidt et al., 2014), we just recorded the endogenous EF generated by

the spontaneous SO.

5.2.1 Endogeneous EF propagation is damped and delayed

Surprisingly, EF propagation of spontaneous and evoked activity elicited damping and delays when traveling across the cut between both disconnected networks (Fig. 4.10). This observation goes against the assumption that neural tissue acts as a homogeneous ohmic conductor where EFs travel nearly instantaneously and undistorted from their origin. To rule out the possibility that the presence of the cut itself was acting on the observed damping and delays, we compared the EF propagation between pharmacologically and physically disconnected networks (Fig. 4.12). The similarity between both recorded waves confirmed that the interface created by the cut was not the cause of the observed damping and delays. Moreover, if the cut had had any impact on the propagation, we would have then expected an increase, and not a decrease, in the conductivity of the medium; the remaining space would have been filled with ACSF mimicking better the isotropic properties of homogeneous ohmic mediums that do not account for damping and delays (Logothetis et al., 2007).

5.2.2 The cortical network as a non-homogeneous tissue

Accompanying the damping effects, propagation of EF waves traveling across cortical columns and layers was characterized by distortions. As a consequence of this, differences arose between EF waves recorded at IG and SG layers; EF waves at IG were wider and larger than EF waves at SG layers (Fig. 4.13). These results point out that the EF propagation is sensitive to the structure and composition of the neural tissue. Thus, the knowledge collected from our experimental model questions the assumption that neural tissue is a homogeneous ohmic conductor, and rather suggests that the wiring cortical network conforms a non-homogeneous medium. Our results are in agreement with previous studies where impedance measurements of the tissue showed non-ohmic and filtering properties of the extracellular medium due to ionic diffusion (Gomes et al., 2016).

However, the conductive properties of the neural tissue still remains controversial. In a recent report, Gratiy and colleagues postulated that the

displacement of currents in the extracellular space (ionic diffusion) can be neglected on extracellular signals as CSD (Gratiy et al., 2017); therefore, tissue could be considered as a homogeneous medium where EF propagation is isotropic (Logothetis et al., 2007). Within the framework of this debate, one should consider whether CSD can be used to infer conductivity properties of the neural tissue. There are numerous complex interactions taking place during network activity, such as synaptic activity, current distribution within the space, temporal dynamics of those currents, dipoles generations etc. that can be recorded with extracellular signals (Bédard et al., 2004; Buzsáki et al., 2012). Evidence that CSD does not totally reflect all those processes occurring during neural activity as LFP signals do (Kajikawa and Schroeder, 2011) awakes some pertinent doubts about the assumptions of CSD theory revisited by Gratiy and collaborators. Along this line of reasoning, even if the ionic diffusion could be neglected when interpreting CSD measurements (Gratiy et al., 2017), such disregard might not be an indicator of the ohmic and filtering properties of the tissue. Also, the possibility of ignoring ionic diffusion cannot be generalized to every pattern of activity, and for instance alternative interpretations may account for slow rhythms ($<$1 Hz) where ionic diffusion exerts a larger contribution (Gratiy et al., 2017). Hence, in our present study, damping and delays observed within the EF propagation of slow waves might be an echo of the non-ohmic properties of the tissue, where ionic diffusion could be contributing (Gomes et al., 2016).

Further evidence about the inhomogeneities of the tissue were found when we computed the EF propagation speed. Velocities measured from the delays turned out to be very low (18.3 ± 2.85 mm/s) (Fig. 4.14), similar to the synaptic propagation velocities (13.6 ± 2.7 mm/s) rather than instantaneous as expected in a homogeneous medium. The speed we found (18.3 ± 2.85 mm/s) was similar to the electric propagation speed of epileptiform activity measured in unfolded hippocampal slices ($\sim$100 mm/s) where the endogenous field transmission was independent of synaptic activity (Zhang et al., 2014).

In previous studies, spatial and temporal analysis of fast and slow rhythms in anesthetized and chronically implanted cats showed larger spatial correlations for slow waves than for fast oscillations (Destexhe et al., 1999). These data further suggest that the frequencies do not attenuate equally within the tissue: fast frequencies attenuate more than slow frequencies (Bédard et al., 2004). Hence, considering the existing variations in the attenuation of frequencies

reported in activity patterns similar to ours (SO) (Bédard et al., 2004), it would be reasonable to speculate that the damping and low speed reported in our study could result from a filtering of high frequencies within the tissue. This would accumulate more evidence to consider the cortical structure as a non-homogeneous medium with frequency dependence (Bédard et al., 2004), rather than as an ohmic conductor with a frequency independent impedance (Logothetis et al., 2007).

In this context, where the characteristics of the tissue might determine the EF propagation, I further investigated whether the anatomical structure has any repercussion in the EF propagation. For this purpose, I tested the effect that an abrupt change in the laminar cortical structure would cause by rotating one side of the slice. This experiment revealed that, EF waves traveling from IG to SG layers were larger than the EFs traveling from SG to IG, the EF waves detected at SG exhibited larger amplitude than at IG, although there were no significant differences (Fig. 4.16). This result was the opposite to the one reported on slices without rotation (longer wave amplitude at IG than at SG). Because IG layers caused larger EF waves than SG layers, disregarding the recording site, one could conclude that the EF wave depended on the network where it was originated. This would be at odds with the previous idea that the tissue behaves as a non-ohmic and frequency-dependence conductor where the measured signals might not totally depend on their origin site. Conversely, considering that substrates with weak synaptic responses receive greater impact of the non-synaptic components occurring in the network (Kajikawa and Schroeder, 2011), SG layers should then reflect better responsiveness to EF waves originated at IG.
However, our experimental procedure, consisting in rotating one side of the slice, involves certain limitations such as damaging the slice or hampering the position of the recording sites with the superficial arrays, that might obscure a possible effect of the structure. Therefore, better approaches are needed to understand to what extent the laminar cortical structure influences EF propagation. In this regard, different tests could be done, for example one interesting experiment to address this matter would be to study EF propagation in the reelin mutant mouse, which shows a disrupted pattern of cortical lamination due to defective polarization and migration of neural cells during cortical development (Wagener et al., 2010; Pielecka-Fortuna et al., 2015; Guy et al., 2016). Therefore, if the laminar structure has any influence on EF propagation, differences in the EF propagation reported here must be

absent in the cortex of those animals.

To further investigate the influence of the medium in the EF propagation, the extracellular space was increased by increasing the ACSF osmolarity. It is well known that hyperosmolarity expands the extracellular space (Traynelis and Dingledine, 1989). This expansion creates more space between neurons resulting in an increase in the conductivity of the medium. So, assuming there is a contribution of ionic diffusion in the EF propagation of SO, the increase in space would make the charges to be more scattered within the medium leading to smaller EF waves and slower EF propagation as observed in our results (Fig. 4.18). Such reduction in the EF propagation is in agreement with previous *in vitro* and *in silico* studies in hippocampus where osmolarity changes were explored (Shahar et al., 2009; Qiu et al., 2015), confirming that the extracellular space influences the endogenous EF activity.

5.3 Endogenous electric fields modulate the occurrence of slow oscillations

Previous approaches to study the feedback loop between endogenous EF and synaptic activity have used external DC stimulation through parallel electrodes (Radman et al., 2007; Fröhlich and McCormick, 2010; Reato et al., 2010; Schmidt et al., 2014), without solving the experimental challenge of isolating synaptic activity and its authentic endogenous EF. Our *in vitro* preparation has overcome this challenge, allowing a better exploration of the interactions between endogenous EF and synaptic activity.

In this work, we used DC stimulation in an attempt to enhance the local excitability and increase the chance that the EF would evoke suprthreshold responses (Up state). Increasing EF stimulation led to faster SO at both sides of the cut (Fig. 4.19), but did not promote the induction of suprathreshold activity by endogenous EF (Fig. 4.20). This could be due to the DC stimulation inducing suprathreshold activity randomly. However, when I induced controlled subthreshold responses with small local applications of glutamate to check if endogenous EF could convert them into proper Up states, no suprathreshold activity was triggered either (Fig. 4.22). These results agree with previous works, where EFs did not trigger action potentials but they

did have an effect on the spike timing (Radman et al., 2007; Reato et al., 2010; Anastassiou and Koch, 2015). Indeed, we observed an increase in synchrony between the two disconnected networks with DC stimulation (4.21), which might be the result of a greater bidirectional effect of each endogenous EF over the corresponding population activity timing on the disconnected networks. Moreover, the higher correlation between both networks was more notorious for weak EF stimulations (± 1 V/m), stimulations that kept the oscillatory rhythms close to their basal frequency (without extremely hyperpolarizing or depolarizing the networks). These results concur with what has been observed in *in vitro* experiments and *in silico*, namely, that low EF stimulations have a significant effect on oscillatory activity (Fröhlich and McCormick, 2010; Reato et al., 2010) and frequency shifts only appear with EF stimulations that match the intrinsic oscillations (Schmidt et al., 2014).

Even if the reported increases in synchrony with DC stimulation denoted entrainment of SO by EFs, it was difficult to know to what extent this was due to the exogenous EF applied through the parallel electrodes or to the pure endogenous EF originated by the slow waves. Simultaneously, there was a double modulation from one network to the other that was difficult to tease apart.
To clarify the entrainment that the noise induced by external EF stimulation might be masking, the frequency of SO was precisely controlled with local application of glutamate. Up states were induced only in one side of the slice at different periodicities. Frequency changes in the glutamate application in one network led to frequency changes in the spontaneous SO in the disconnected network, unraveling an entrainment of slow wave rhythms by endogenous EF (Fig. 4.24). It should be noticed that the side modulated by the endogenous EF did not reach frequencies similar to the glutamate applications, meaning that evoked Up states on one side did not directly trigger Up state occurrence on the other. This is in line with the notion that endogenous EFs are able to synchronize neural activity by modulating its timing but they cannot trigger any additional synaptic activity (Anastassiou et al., 2011).

Variations in the structure (cortical layer disruption) or the extracellular medium (osmolarity increase) avoided the modulation, suggesting that physiological conditions under which SO are originated must be preserved to study ephaptic coupling between independent networks.

Why can endogenous EFs not trigger Up states but can induce variations in the frequency of SO? The main reason would involve resonance of neurons and networks. Resonance of a neuron is the propensity that it has to respond more strongly to an input, modulating either its spike probability or subthreshold activity. Thus, resonance becomes the link between subthreshold and suprathreshold responses (Dwyer et al., 2012). Indeed, theta resonance in layer 5 pyramidal neurons has been described as one of the contributors to drive cortical network activity (Schmidt et al., 2016). Moreover, such resonance was demonstrated in freely behaving animals to allow the entrainment of the cortex by the hippocampus through parvalbumin interneurons (Stark et al., 2013). Thus, the modulation observed between both disconnected networks in our experiments could be due to the resonance properties of neurons.
Future research will hopefully shed light on how intrinsic properties of neurons are affected by endogenous EFs, and to what extent such fields affect the activity of individual neurons leading to changes in the global network activity.

5.4 Concluding remarks and perspectives

In summary, the findings exposed within this thesis have unraveled that slow waves are not local events, they propagate along the cortical network. The propagation of SO within the cortex is largely influenced by the structure of the cortical tissue. Also, an intermediate excitability level controlled by extracellular K^+ leads to the highest spatiotemporal regularity. This excitability level represents the synaptic noise, revealing that a collective stochastic coherence phenomenon leads to the maximal regularity of SO. In addition, slow waves generate EFs which travel independently of synaptic transmission within the cortical tissue, suggesting that cortical rhythms emerge from interconnected networks and might be influenced by the EFs generated by these networks. Moreover, these EFs travel with damping at a slow propagation speed, similar to the synaptic propagation velocities (18.3 ± 2.85 mm/s), rather than instantaneous as volume conduction, suggesting that neural tissue is non-homogeneous. All together, these results imply that interpretation of LFP, EEG/MEG needs to be reconsidered as most experimental and clinical approaches assume that neural tissue is a homogeneous ohmic conductor. Finally, endogenous fields modulate

the SO frequency of a synaptically disconnected network, suggesting that non-synaptic mechanisms may be able to couple populations of neurons. Such coupling may affect information processing in the cortex and synaptic plasticity; thus, the ability of EFs to modulate neuronal timing might be explored as a promising therapeutical intervention to restore abnormal spike timing that characterize many neurobiological disorders.

Chapter 6

Conclusions

1. Slow waves are not local events, but they propagate along cortical slices parallel to the surface.
2. The slow wave propagation across cortical columns is variable in initiation sites and speed. Our concrete measures suggest that under the *in vitro* conditions that we work, it is a memoryless random process, similarly to what has been observed in deep anesthesia.
3. Slow wave propagation across columns is led by an early propagation strip that is shaped by the structure of cortical layer 4 and layer 5, coinciding with the highest firing rate and longest Up states that act as leader of the propagating wave.
4. The neuronal population excitability can be modulated by extracellular K^+ concentration, leading to changes in the background synaptic noise, and in the frequency and variability of slow oscillations.
5. Slow oscillations reach the highest spatiotemporal regularity with an intermediate excitability level, and thus noise level, similar to that in physiological conditions, what is known as stochastic coherence.
6. Initiation and termination of Up states are a global network phenomenon led by a collective stochastic coherence regime.
7. Slow waves generate an endogenous electric field that travels with damping and delays, suggesting that cortical rhythms emerging from synaptically interconnected networks may be influenced by the interaction of the electric fields generated by these networks.
8. Local blockade of synaptic activity with TTX did not affect electric field propagation, revealing that electric fields travel independently

of synaptic activity across pharmacologically and physically synaptic-disconnected cortical networks.

9. Endogenous electric field propagation is characterized by distortions when traveling across cortical columns and layers, suggesting that EF propagation is sensitive to the structure and the composition of the neural tissue.

10. Our measures of electric field propagation speeds are low (18.3 ± 2.85 mm/s), being similar to synaptic propagation speeds rather than instantaneous as volume conduction transmission.

11. Experimental manipulation that changes the cortical structure, such as layer inversion, suggest that electric fields have a critical influence in shaping emergent activity.

12. Increasing the extracellular space with a hyperosmolar solution reduces amplitude and increases duration of electric field waves with respect to a control condition, changing the distortion suffered by spontaneous Up states when traveling across the cut (compression in control conditions, widening in hyperosmolar conditions).

13. External DC electric stimulation does not induce any variation on spontaneous Up states; in consequence no changes were observed in the characteristics of electric field waves generated by them.

14. External DC electric stimulations of low intensity, such as ± 1 V/m, can be enough to synchronize non-synaptically two independent networks.

15. Endogenous electric fields can hardly induce suprathreshold activity in a synaptically disconnected network, but they are able to enhance subthreshold responses.

16. Endogenous electric fields modulate slow wave frequency of a synaptically disconnected network, suggesting that non-molecular mechanisms may be able to couple neurons non-synaptically.

17. Slow oscillations propagate in the cortical network shaped by the laminar structure and generating electric fields that in turn modulate the frequency of slow waves.

Bibliography

George K Aghajanian and Kurt Rasmussen. Intracellular studies in the facial nucleus illustrating a simple new method for obtaining viable motoneurons in adult rat brain slices. *Synapse*, 3(4):331–338, 1989.

Florin Amzica, Marcello Massimini, and Alfredo Manfridi. Spatial buffering during slow and paroxysmal sleep oscillations in cortical networks of glial cells in vivo. *Journal of Neuroscience*, 22(3):1042–1053, 2002.

Costas A Anastassiou and Christof Koch. Ephaptic coupling to endogenous electric field activity: why bother? *Current opinion in neurobiology*, 31:95–103, 2015.

Costas A Anastassiou, Rodrigo Perin, Henry Markram, and Christof Koch. Ephaptic coupling of cortical neurons. *Nature neuroscience*, 14(2):217–223, 2011.

Costas A Anastassiou, Rodrigo Perin, György Buzsáki, Henry Markram, and Christof Koch. Cell type-and activity-dependent extracellular correlates of intracellular spiking. *Journal of neurophysiology*, 114(1):608–623, 2015.

Dominique Arion, Travis Unger, David A Lewis, and Károly Mirnics. Molecular markers distinguishing supragranular and infragranular layers in the human prefrontal cortex. *European Journal of Neuroscience*, 25(6): 1843–1854, 2007.

Giorgio A Ascoli, Lidia Alonso-Nanclares, Stewart A Anderson, German Barrionuevo, Ruth Benavides-Piccione, Andreas Burkhalter, György Buzsáki, Bruno Cauli, Javier DeFelipe, Alfonso Fairén, et al. Petilla terminology: nomenclature of features of gabaergic interneurons of the cerebral cortex. *Nature Reviews Neuroscience*, 9(7):557–568, 2008.

A Peter Bannister. Inter-and intra-laminar connections of pyramidal cells in the neocortex. *Neuroscience research*, 53(2):95–103, 2005.

Maxim Bazhenov, Igor Timofeev, Mircea Steriade, and Terrence J Sejnowski. Model of thalamocortical slow-wave sleep oscillations and transitions to activated states. *Journal of neuroscience*, 22(19):8691–8704, 2002.

Maxim Bazhenov, Igor Timofeev, Mircea Steriade, and Terrence J Sejnowski. Potassium model for slow (2-3 hz) in vivo neocortical paroxysmal oscillations. *Journal of neurophysiology*, 92(2):1116–1132, 2004.

Claude Bédard, Helmut Kröger, and Alain Destexhe. Modeling extracellular field potentials and the frequency-filtering properties of extracellular space. *Biophysical journal*, 86(3):1829–1842, 2004.

Riccardo Beltramo, Giulia D'urso, Marco Dal Maschio, Pasqualina Farisello, Serena Bovetti, Yoanne Clovis, Glenda Lassi, Valter Tucci, Davide De Pietri Tonelli, and Tommaso Fellin. Layer-specific excitatory circuits differentially control recurrent network dynamics in the neocortex. *Nature neuroscience*, 16 (2):227–234, 2013.

Andrew Stephen Blaeser, Barry W Connors, and Arto V Nurmikko. Spontaneous dynamics of neural networks in deep layers of prefrontal cortex. *Journal of Neurophysiology*, pages jn–00295, 2017.

György Buzsáki, Costas A Anastassiou, and Christof Koch. The origin of extracellular fields and currents - eeg, ecog, lfp and spikes. *Nature reviews neuroscience*, 13(6):407–420, 2012.

S Ramon Y Cajal. Structure and connections of neurons. *Bulletin of the Los Angeles Neurological Society*, 17(1-2):5–46, 1952.

Patricia Castano-Prat, Maria Perez-Zabalza, Lorena Perez-Mendez, Rosa M Escorihuela, and Maria V Sanchez-Vives. Slow and fast neocortical oscillations in the senescence-accelerated mouse model samp8. *Frontiers in Aging Neuroscience*, 9:141, 2017.

Sylvain Chauvette, Maxim Volgushev, and Igor Timofeev. Origin of active states in local neocortical networks during slow sleep oscillation. *Cerebral cortex*, 20(11):2660–2674, 2010.

Albert Compte, Maria V Sanchez-Vives, David A McCormick, and Xiao-Jing Wang. Cellular and network mechanisms of slow oscillatory activity (¡ 1 hz) and wave propagations in a cortical network model. *Journal of neurophysiology*, 89(5):2707–2725, 2003.

Albert Compte, Ramon Reig, Vanessa F Descalzo, Michael A Harvey, Gabriel D Puccini, and Maria V Sanchez-Vives. Spontaneous high-frequency (10–80 hz) oscillations during up states in the cerebral cortex in vitro. *Journal of Neuroscience*, 28(51):13828–13844, 2008.

Albert Compte, Ramon Reig, and Maria V Sanchez-Vives. Timing excitation and inhibition in the cortical network. In *Coherent Behavior in Neuronal Networks*, pages 17–46. Springer, 2009.

Vincenzo Crunelli and Stuart W Hughes. The slow (<1 hz) rhythm of non-rem sleep: a dialogue between three cardinal oscillators. *Nature neuroscience*, 13 (1):9–17, 2010.

Vincenzo Crunelli, Francois David, Magor L Lőrincz, and Stuart W Hughes. The thalamocortical network as a single slow wave-generating unit. *Current opinion in neurobiology*, 31:72–80, 2015.

Richárd Csercsa, Balázs Dombovári, Dániel Fabó, Lucia Wittner, Loránd Erőss, László Entz, András Sólyom, György Rásonyi, Anna Szűcs, Anna Kelemen, et al. Laminar analysis of slow wave activity in humans. *Brain*, page awq169, 2010.

Mattia D'Andola, Beatriz Rebollo, Adenauer G Casali, Julia F Weinert, Andrea Pigorini, Rosa Villa, Marcello Massimini, and Maria V Sanchez-Vives. Bistability, causality, and complexity in cortical networks: An in vitro perturbational study. *Cerebral Cortex*, pages 1–10, 2017.

François David, Joscha T Schmiedt, Hannah L Taylor, Gergely Orban, Giuseppe Di Giovanni, Victor N Uebele, John J Renger, Régis C Lambert, Nathalie Leresche, and Vincenzo Crunelli. Essential thalamic contribution to slow waves of natural sleep. *Journal of Neuroscience*, 33(50):19599–19610, 2013.

Javier DeFelipe. The evolution of the brain, the human nature of cortical circuits, and intellectual creativity. *Frontiers in neuroanatomy*, 5:29, 2011.

Alain Destexhe, Diego Contreras, and Mircea Steriade. Spatiotemporal analysis of local field potentials and unit discharges in cat cerebral cortex during natural wake and sleep states. *Journal of Neuroscience*, 19(11): 4595–4608, 1999.

Rodney J Douglas and Kevan AC Martin. Neuronal circuits of the neocortex. *Annu. Rev. Neurosci.*, 27:419–451, 2004.

Jennifer Dwyer, Hyong Lee, Amber Martell, and Wim van Drongelen. Resonance in neocortical neurons and networks. *European Journal of Neuroscience*, 36(12):3698–3708, 2012.

Richárd Fiáth, Bálint Péter Kerekes, Lucia Wittner, Kinga Tóth, Patrícia Beregszászi, Domonkos Horváth, and István Ulbert. Laminar analysis of the slow wave activity in the somatosensory cortex of anesthetized rats. *European Journal of Neuroscience*, 44(3):1935–1951, 2016.

Flavio Fröhlich and David A McCormick. Endogenous electric fields may guide neocortical network activity. *Neuron*, 67(1):129–143, 2010.

Jean-Marie Gomes, Claude Bédard, Silvana Valtcheva, Matthew Nelson, Vitalia Khokhlova, Pierre Pouget, Laurent Venance, Thierry Bal, and Alain Destexhe. Intracellular impedance measurements reveal non-ohmic properties of the extracellular medium around neurons. *Biophysical journal*, 110(1):234–246, 2016.

Sergey L Gratiy, Geir Halnes, Daniel Denman, Michael J Hawrylycz, Christof Koch, Gaute T Einevoll, and Costas A Anastassiou. From maxwell's equations to the theory of current-source density analysis. *European Journal of Neuroscience*, 2017.

Julien Guy, Alexandra Sachkova, Martin Möck, Mirko Witte, Robin J Wagener, and Jochen F Staiger. Intracortical network effects preserve thalamocortical input efficacy in a cortex without layers. *Cerebral Cortex*, 2016.

Andrea Hasenstaub, Yousheng Shu, Bilal Haider, Udo Kraushaar, Alvaro Duque, and David A McCormick. Inhibitory postsynaptic potentials carry synchronized frequency information in active cortical networks. *Neuron*, 47 (3):423–435, 2005.

Oscar Herreras. Local field potentials: Myths and misunderstandings. *Frontiers in Neural Circuits*, 10, 2016.

Jihane Homman-Ludiye, Paul R Manger, and James A Bourne. Immunohistochemical parcellation of the ferret (mustela putorius) visual cortex reveals substantial homology with the cat (felis catus). *Journal of Comparative Neurology*, 518(21):4439–4462, 2010.

JG Jefferys. Nonsynaptic modulation of neuronal activity in the brain: electric currents and extracellular ions. *Physiological reviews*, 75(4):689–723, 1995.

Yoshinao Kajikawa and Charles E Schroeder. How local is the local field potential? *Neuron*, 72(5):847–858, 2011.

Jean-Philippe Lachaux, Eugenio Rodriguez, Jacques Martinerie, Francisco J Varela, et al. Measuring phase synchrony in brain signals. *Human brain mapping*, 8(4):194–208, 1999.

Wei-Chung Allen Lee, Vincent Bonin, Michael Reed, Brett J Graham, Greg Hood, Katie Glattfelder, and R Clay Reid. Anatomy and function of an excitatory network in the visual cortex. *Nature*, 532(7599):370–374, 2016.

Nikos K Logothetis, Christoph Kayser, and Axel Oeltermann. In vivo measurement of cortical impedance spectrum in monkeys: implications for signal propagation. *Neuron*, 55(5):809–823, 2007.

Rafael Lorente de Nó. Studies on the structure of the cerebral cortex. ii. continuation of the study of the ammonic system. *Journal für Psychologie und Neurologie*, 1934.

Magor L Lőrincz, David Gunner, Ying Bao, William M Connelly, John TR Isaac, Stuart W Hughes, and Vincenzo Crunelli. A distinct class of slow ($\sim$ 0.2–2 hz) intrinsically bursting layer 5 pyramidal neurons determines up/down state dynamics in the neocortex. *Journal of Neuroscience*, 35(14):5442–5458, 2015.

Arianna Maffei. Fifty shades of inhibition. *Current Opinion in Neurobiology*, 43: 43–47, 2017.

Henry Markram, Eilif Muller, Srikanth Ramaswamy, Michael W Reimann, Marwan Abdellah, Carlos Aguado Sanchez, Anastasia Ailamaki, Lidia Alonso-Nanclares, Nicolas Antille, Selim Arsever, et al. Reconstruction and simulation of neocortical microcircuitry. *Cell*, 163(2):456–492, 2015.

Lisa Marshall, Halla Helgadóttir, Matthias Mölle, and Jan Born. Boosting slow oscillations during sleep potentiates memory. *Nature*, 444(7119):610–613, 2006.

Marcello Massimini, Reto Huber, Fabio Ferrarelli, Sean Hill, and Giulio Tononi. The sleep slow oscillation as a traveling wave. *Journal of Neuroscience*, 24(31): 6862–6870, 2004.

Maurizio Mattia and Paolo Del Giudice. Population dynamics of interacting spiking neurons. *Physical Review E*, 66(5):051917, 2002.

Maurizio Mattia and Maria V Sanchez-Vives. Exploring the spectrum of dynamical regimes and timescales in spontaneous cortical activity. *Cognitive neurodynamics*, 6(3):239–250, 2012.

David A McCormick, Barry W Connors, James W Lighthall, and David A Prince. Comparative electrophysiology of pyramidal and sparsely spiny stellate neurons of the neocortex. *Journal of neurophysiology*, 54(4):782–806, 1985.

Garrett T Neske. The slow oscillation in cortical and thalamic networks: mechanisms and functions. *Frontiers in neural circuits*, 9, 2015.

Michael Okun and Ilan Lampl. Instantaneous correlation of excitation and inhibition during ongoing and sensory-evoked activities. *Nature neuroscience*, 11(5):535–537, 2008.

Justyna Pielecka-Fortuna, Robin Jan Wagener, Ann-Kristin Martens, Bianka Goetze, Karl-Friedrich Schmidt, Jochen F Staiger, and Siegrid Löwel. The disorganized visual cortex in reelin-deficient mice is functional and allows for enhanced plasticity. *Brain Structure and Function*, 220(6):3449–3467, 2015.

Kira E Poskanzer and Rafael Yuste. Astrocytic regulation of cortical up states. *Proceedings of the National Academy of Sciences*, 108(45):18453–18458, 2011.

Chen Qiu, Rajat S Shivacharan, Mingming Zhang, and Dominique M Durand. Can neural activity propagate by endogenous electrical field? *Journal of Neuroscience*, 35(48):15800–15811, 2015.

Thomas Radman, Yuzhuo Su, Je Hi An, Lucas C Parra, and Marom Bikson. Spike timing amplifies the effect of electric fields on neurons: implications for endogenous field effects. *Journal of Neuroscience*, 27(11):3030–3036, 2007.

Davide Reato, Asif Rahman, Marom Bikson, and Lucas C Parra. Low-intensity electrical stimulation affects network dynamics by modulating population rate and spike timing. *Journal of Neuroscience*, 30(45):15067–15079, 2010.

Ramon Reig and Maria V Sanchez-Vives. Synaptic transmission and plasticity in an active cortical network. *PLoS One*, 2(8):e670, 2007.

Ramon Reig, Roberto Gallego, Lionel G Nowak, and Maria V Sanchez-Vives. Impact of cortical network activity on short-term synaptic depression. *Cerebral Cortex*, 16(5):688–695, 2006.

Ramon Reig, Maurizio Mattia, Albert Compte, Carlos Belmonte, and Maria V Sanchez-Vives. Temperature modulation of slow and fast cortical rhythms. *Journal of neurophysiology*, 103(3):1253–1261, 2010.

Vicente Reyes-Puerta, Jenq-Wei Yang, Magdalena E Siwek, Werner Kilb, Jyh-Jang Sun, and Heiko J Luhmann. Propagation of spontaneous slow-wave activity across columns and layers of the adult rat barrel cortex in vivo. *Brain Structure and Function*, 221(9):4429–4449, 2016.

Marcel Ruiz-Mejias, Laura Ciria-Suarez, Maurizio Mattia, and Maria V Sanchez-Vives. Slow and fast rhythms generated in the cerebral cortex of the anesthetized mouse. *Journal of neurophysiology*, 106(6):2910–2921, 2011.

Marcel Ruiz-Mejias, Maria Martinez de Lagran, Maurizio Mattia, Patricia Castano-Prat, Lorena Perez-Mendez, Laura Ciria-Suarez, Thomas Gener, Belen Sancristobal, Jordi García-Ojalvo, Agnès Gruart, et al. Overexpression of dyrk1a, a down syndrome candidate, decreases excitability and impairs gamma oscillations in the prefrontal cortex. *Journal of Neuroscience*, 36(13): 3648–3659, 2016.

Seward B Rutkove. Introduction to volume conduction. In *The clinical neurophysiology primer*, pages 43–53. Springer, 2007.

Shuzo Sakata and Kenneth D Harris. Laminar structure of spontaneous and sensory-evoked population activity in auditory cortex. *Neuron*, 64(3): 404–418, 2009.

Maria V Sanchez-Vives. Spontaneous rhythmic activity in the adult cerebral cortex in vitro. *Isolated Central Nervous System Circuits*, pages 263–284, 2012.

Maria V Sanchez-Vives and Maurizio Mattia. Slow wave activity as the default mode of the cerebral cortex. *Arch Ital Biol*, 152:147–155, 2014.

Maria V Sanchez-Vives and David A McCormick. Functional properties of perigeniculate inhibition of dorsal lateral geniculate nucleus thalamocortical neurons in vitro. *Journal of Neuroscience*, 17(22):8880–8893, 1997.

Maria V Sanchez-Vives and David A McCormick. Cellular and network mechanisms of rhythmic recurrent activity in neocortex. *Nature neuroscience*, 3(10):1027–1034, 2000.

Maria V Sanchez-Vives, Thierry Bal, and David A McCormick. Inhibitory interactions between perigeniculate gabaergic neurons. *Journal of Neuroscience*, 17(22):8894–8908, 1997.

Maria V Sanchez-Vives, Vanessa F Descalzo, Ramón Reig, NA Figueroa, Albert Compte, and Roberto Gallego. Rhythmic spontaneous activity in the piriform cortex. *Cerebral cortex*, 18(5):1179–1192, 2008.

Maria V Sanchez-Vives, Maurizio Mattia, Albert Compte, Maria Perez-Zabalza, Milena Winograd, Vanessa F Descalzo, and Ramon Reig. Inhibitory modulation of cortical up states. *Journal of neurophysiology*, 104(3): 1314–1324, 2010.

Maria V Sanchez-Vives, Mattia D'Andola, Pol Boada-Collado, M Giulioni, and Julia F Weinert. Electrical modulation of cerebral cortex activity: Mechanisms and applications. In *Converging Clinical and Engineering Research on Neurorehabilitation II*, pages 1409–1411. Springer, 2017a.

Maria V Sanchez-Vives, Marcello. Massimini, and Maurizio Mattia. Shaping the default activity pattern of the cortical network. *Neuron*, in press, 2017b. doi: NEURON-D-16-02060R2.

Belén Sancristóbal, Beatriz Rebollo, Pol Boada, Maria V Sanchez-Vives, and Jordi Garcia-Ojalvo. Collective stochastic coherence in recurrent neuronal networks. *Nature Physics*, 12(9):881–887, 2016.

Stephen L Schmidt, Apoorva K Iyengar, A Alban Foulser, Michael R Boyle, and Flavio Fröhlich. Endogenous cortical oscillations constrain neuromodulation by weak electric fields. *Brain stimulation*, 7(6):878–889, 2014.

Stephen L Schmidt, Christopher R Dorsett, Apoorva K Iyengar, and Flavio Fröhlich. Interaction of intrinsic and synaptic currents mediate network resonance driven by layer v pyramidal cells. *Cerebral Cortex*, 2016.

E Shahar, M Derchansky, and PL Carlen. The role of altered tissue osmolality on the characteristics and propagation of seizure activity in the intact isolated mouse hippocampus. *Clinical Neurophysiology*, 120(4):673–678, 2009.

Jordi Soriano and Jaume Casademunt. Neuronal cultures: The brains complexity and non-equilibrium physics, all in a dish. *Contributions to science*, 11:225–235, 2015.

Eran Stark, Ronny Eichler, Lisa Roux, Shigeyoshi Fujisawa, Horacio G Rotstein, and György Buzsáki. Inhibition-induced theta resonance in cortical circuits. *Neuron*, 80(5):1263–1276, 2013.

M Steriade, D Contreras, R Curró Dossi, and A Nunez. The slow (<1 hz) oscillation in reticular thalamic and thalamocortical neurons: scenario of sleep rhythm generation in interacting thalamic and neocortical networks. *Journal of Neuroscience*, 13(8):3284–3299, 1993a.

Mircea Steriade, A Nunez, and F Amzica. A novel slow (<1 hz) oscillation of neocortical neurons in vivo: depolarizing and hyperpolarizing components. *Journal of neuroscience*, 13(8):3252–3265, 1993b.

Mircea Steriade, Angel Nuñez, and Florin Amzica. Intracellular analysis of relations between the slow (<1 hz) neocortical oscillation and other sleep rhythms of the electroencephalogram. *Journal of Neuroscience*, 13(8): 3266–3283, 1993c.

Mircea Steriade, Diego Contreras, Florin Amzica, and Igor Timofeev. Synchronization of fast (30-40 hz) spontaneous oscillations in intrathalamic and thalamocortical networks. *Journal of Neuroscience*, 16(8):2788–2808, 1996.

Olav Stetter, Jordi Soriano, Theo Geisel, Demian Battaglia, Pedro L Garrido, Joaquín Marro, Joaquín J Torres, and JM Cortés. From structure to function, via dynamics. In *AIP Conference Proceedings*, volume 1510, pages 64–73. AIP, 2013.

Albrecht Stroh, Helmuth Adelsberger, Alexander Groh, Charlotta Rühlmann, Sebastian Fischer, Anja Schierloh, Karl Deisseroth, and Arthur Konnerth. Making waves: initiation and propagation of corticothalamic ca 2+ waves in vivo. *Neuron*, 77(6):1136–1150, 2013.

Bartosz Teleńczuk, Nima Dehghani, Michel Le Van Quyen, Sydney S Cash, Eric Halgren, Nicholas G Hatsopoulos, and Alain Destexhe. Local field potentials primarily reflect inhibitory neuron activity in human and monkey cortex. *Scientific Reports*, 7:40211, 2017.

Alex M Thomson and Christophe Lamy. Functional maps of neocortical local circuitry. *Frontiers in neuroscience*, 1:2, 2007.

I Timofeev, F Grenier, M Bazhenov, TJ Sejnowski, and Mircea Steriade. Origin of slow cortical oscillations in deafferented cortical slabs. *Cerebral Cortex*, 10 (12):1185–1199, 2000.

Stephen F Traynelis and Raymond Dingledine. Role of extracellular space in hyperosmotic suppression of potassium-induced electrographic seizures. *Journal of Neurophysiology*, 61(5):927–938, 1989.

Maxim Volgushev, Sylvain Chauvette, Mikhail Mukovski, and Igor Timofeev. Precise long-range synchronization of activity and silence in neocortical neurons during slow-wave sleep. *Journal of Neuroscience*, 26(21):5665–5672, 2006.

Vladyslav V Vyazovskiy and Kenneth D Harris. Sleep and the single neuron: the role of global slow oscillations in individual cell rest. *Nature Reviews Neuroscience*, 14(6):443–451, 2013.

Robin J Wagener, Csaba Dávid, Shanting Zhao, Carola A Haas, and Jochen F Staiger. The somatosensory cortex of reeler mutant mice shows absent layering but intact formation and behavioral activation of columnar somatotopic maps. *Journal of Neuroscience*, 30(46):15700–15709, 2010.

Shennan A Weiss and Donald S Faber. Field effects in the cns play functional roles. *Frontiers in neural circuits*, 4:15, 2010.

Jason C Wester and Diego Contreras. Columnar interactions determine horizontal propagation of recurrent network activity in neocortex. *Journal of Neuroscience*, 32(16):5454–5471, 2012.

Charles J Wilson and Philip M Groves. Spontaneous firing patterns of identified spiny neurons in the rat neostriatum. *Brain research*, 220(1):67–80, 1981.

Lulu Xie, Hongyi Kang, Qiwu Xu, Michael J Chen, Yonghong Liao, Meenakshisundaram Thiyagarajan, John ODonnell, Daniel J Christensen, Charles Nicholson, Jeffrey J Iliff, et al. Sleep drives metabolite clearance from the adult brain. *science*, 342(6156):373–377, 2013.

Mingming Zhang, Thomas P Ladas, Chen Qiu, Rajat S Shivacharan, Luis E Gonzalez-Reyes, and Dominique M Durand. Propagation of epileptiform activity can be independent of synaptic transmission, gap junctions, or diffusion and is consistent with electrical field transmission. *Journal of Neuroscience*, 34(4):1409–1419, 2014.

Appendix A

Publications

nature physics

ARTICLES

PUBLISHED ONLINE: 2 MAY 2016 | DOI: 10.1038/NPHYS3739

Collective stochastic coherence in recurrent neuronal networks

Belén Sancristóbal[1†], Beatriz Rebollo[2], Pol Boada[2], Maria V. Sanchez-Vives[2,3*] and Jordi Garcia-Ojalvo[1*]

Recurrent networks of dynamic elements frequently exhibit emergent collective oscillations, which can show substantial regularity even when the individual elements are considerably noisy. How noise-induced dynamics at the local level coexists with regular oscillations at the global level is still unclear. Here we show that a combination of stochastic recurrence-based initiation with deterministic refractoriness in an excitable network can reconcile these two features, leading to maximum collective coherence for an intermediate noise level. We report this behaviour in the slow oscillation regime exhibited by a cerebral cortex network under dynamical conditions resembling slow-wave sleep and anaesthesia. Computational analysis of a biologically realistic network model reveals that an intermediate level of background noise leads to quasi-regular dynamics. We verify this prediction experimentally in cortical slices subject to varying amounts of extracellular potassium, which modulates neuronal excitability and thus synaptic noise. The model also predicts that this effectively regular state should exhibit noise-induced memory of the spatial propagation profile of the collective oscillations, which is also verified experimentally. Taken together, these results allow us to construe the high regularity observed experimentally in the brain as an instance of collective stochastic coherence.

Recurrent networks are directed graphs with cyclic paths that can exhibit self-sustained collective dynamics. When the network nodes are threshold elements, a sufficiently large background noise will render their activity stochastic. Yet, the collective behaviour of the network is frequently highly regular in time. This raises the question of how the stochastic nature of the network elements coexists with the quasi-deterministic character of the collective dynamics. Although coupling has long been proposed as a regularizing mechanism for interacting sloppy oscillators[1,2], the situation is much less clear when the individual elements are not intrinsic oscillators, but exhibit noise-driven pulsatile dynamics, such as in excitable elements. A relevant instance of this situation is given by neuronal networks.

Here we study the interplay between noise and collective dynamics in networks of neurons from the cerebral cortex operating in the state of slow oscillations, a dynamical regime that has been suggested as the default activity of the cortex[3]. In this physiological state, typical of slow-wave sleep and anaesthesia[4], the membrane potential of cortical neurons alternates at frequencies of the order of 1 Hz between the so-called UP and DOWN states[5,6]. UP states are characterized by a depolarization of the membrane voltage towards the spiking threshold and a sustained firing activity of the neurons, similar to their dynamics during wakefulness. In contrast, in the DOWN states, neurons are mostly silent and exhibit a hyperpolarized membrane voltage. The fact that UP and DOWN states exist spontaneously *in vitro*[7,8], in the absence of external stimulation, suggests that this dynamical regime is self-sustained, appearing locally without requiring either large-scale cortical interactions or external inputs. In other words, the recurrent connectivity between neurons is sufficient for the emergence of these slow oscillations[9].

We examine the recurrent network dynamics exhibited *in vitro* by slices of the ferret cerebral cortex. In our experiments, noise is determined by the level of neuronal excitability, which can be controlled by the extracellular potassium concentration in the medium. In contrast to previous studies[10], no external time-dependent signals are applied to the system, which operates spontaneously in a regime very close to what is observed *in vivo*[7]. The regularity of the slow oscillations decreases when the brain comes out of deep anaesthesia[11], anticipating the loss of the slow oscillatory regime and the emergence of the sustained depolarized state characteristic of wakefulness[12].

Theoretical work has shown that the sequence of UP and DOWN states can be highly irregular in the presence of noisy inputs, provided inhibition is decreased[13], for low AMPA conductances of the connections between pyramidal neurons and inhibitory interneurons[14], or more generally by changing the stability balance between metastable UP and DOWN attractors—for instance, through modulation of the fatigue- and adaptation-mediated inhibitory feedback[9]. The nature of the more regular regime characteristic of the sleep state is, however, still under debate. Is it a deterministic or a noise-driven state? Here we explore the latter possibility in an isolated network of the cerebral cortex. We observe that the cortical network generates slow oscillations that exhibit maximal regularity for an intermediate amount of background synaptic noise, in what can be construed as an instance of stochastic coherence.

In generic (uncoupled) excitable systems, stochastic coherence arises from the fact that the entry into the excited state is noise-driven, whereas the exit is basically controlled by deterministic processes and is followed by a refractory period, after which

[1]Department of Experimental and Health Sciences, Universitat Pompeu Fabra, Barcelona Biomedical Research Park, 08003 Barcelona, Spain. [2]Institut de Investigacions Biomèdiques August Pi i Sunyer, 08036 Barcelona, Spain. [3]Institució Catalana de Recerca i Estudis Avançats (ICREA), 08010 Barcelona, Spain. [†]Present addresses: Physics Department and Center for Neural Dynamics, University of Ottawa, Ottawa, Ontario K1N 6N5, Canada; Mind, Brain Imaging and Neuroethics Research Unit, Royal Ottawa Healthcare, Institute of Mental Health Research, Ottawa, Ontario K1Z 7K4, Canada.
*e-mail: msanche3@clinic.ub.es; jordi.g.ojalvo@upf.edu

no reinitiation is possible for a certain time window under moderate noise[15,16]. In those conditions, increasing noise leads to more frequent initiations, which eventually pile up at the refractory period with strong regularity, whereas, for larger noise, refractoriness breaks down and the dynamics becomes irregular again. Here we conjecture that UP/DOWN oscillations exhibit this behaviour, motivated by the realization that the neuronal networks underlying the phenomenon show the three main requirements of stochastic coherence (stochastic initiation, deterministic termination, and refractoriness) at the collective level.

First, the initiation of the UP state is triggered by the spontaneous (noise-driven) simultaneous firing of a few excitatory neurons. Second, the termination of the UP state can be explained by an accumulation of adaptation during the UP state, which can be expected to be mainly deterministic[9]. The transition from the UP to the DOWN state can be accounted for by the activity-dependent adaptation of neurons caused by the activation of potassium channels that reduce the sensitivity to synaptic inputs[7,17]. This is a cumulative processes driven by the high (and well-defined) firing rate characteristic of the UP regime, and is thus essentially deterministic. Other cumulative mechanisms for UP-state termination have been proposed, including synapse fatigue caused by depression[18,19], but they are also mostly independent of noise at the network level. Importantly, all these mechanisms require a recovery of the network excitability following the UP state, leading to refractoriness[7].

We thus propose that stochastic coherence provides a mechanism by which the natural excitability of the cortex determines the regularity of the UP/DOWN dynamics, by controlling the amount of background synaptic noise acting on the neurons. In that way, an intermediate level of excitability which coincides with physiological conditions[20] would lead to maximally coherent slow oscillations. In that scenario, the variations in regularity that are characteristic of sleep-to-wake transitions[21,22] would arise from regulated changes in cortical excitability. In contrast to previous studies of stochastic coherence at the level of individual neurons[15,23,24], the stochastic coherence reported here is a purely collective phenomenon, because both the initiation and the termination of the UP states arise only at the network level (initiation resulting from recurrent activation, and termination emerging from potassium channel-mediated adaptation, which comes into effect only during network-driven, high-frequency UP-state activity).

Collective stochastic coherence in a spiking network model

Following Compte *et al.*[17], we consider a network of excitatory and inhibitory neurons described by conductance-based models (see Methods for a full description). Network clustering enables recurrence of neuronal activity, through which randomly occurring spikes lead to a cascade of neuronal firing events (UP state). This is shown in the top panel of Fig. 1a, which depicts the typical dynamics of two neurons from the network, one excitatory and the other inhibitory. The UP state terminates mainly via a potassium channel dependent on the intracellular sodium concentration, I_{KNa}, which is known to be expressed throughout the brain[25]. An increase in the sodium concentration due to the enhancement of the firing activity of the cell during the UP state activates this adaptive current, which in turn renders the neuron insensitive to upcoming presynaptic action potentials[26]. This mechanism leads to a hyperpolarization of the neurons that increases in amplitude and duration with the firing rate[27,28], and terminates the UP state[17]. To quantify the dynamics of the entire neuronal population we use the multiunit activity (MUA), whose value on a logarithmic scale is estimated as the average spectral power of the local field potential (LFP) in a particular frequency band, relative to the total power[29] (see Methods). The time evolution of the LFP (Fig. 1a, middle) and of the log(MUA)

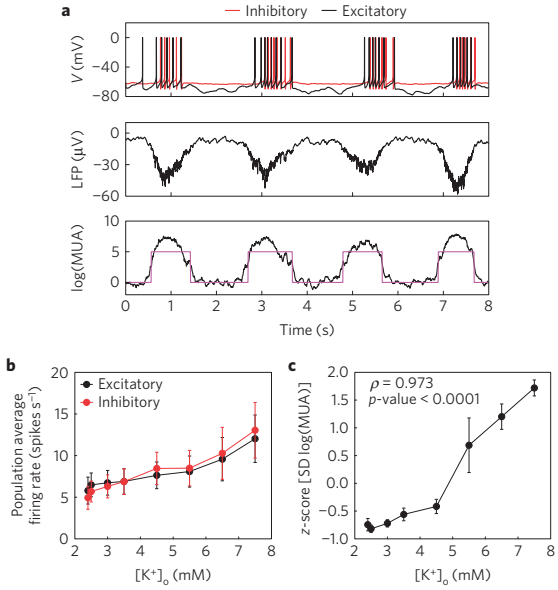

Figure 1 | UP/DOWN oscillations in a cortical network model. a, Time traces of two specific neurons in the network (top panel), including an excitatory neuron (black line) and an inhibitory neuron (red line). The LFP and log(MUA) time traces of the full network are shown in the middle and bottom panels, respectively. Magenta lines in the bottom panel indicate the boundaries of the UP states computed from the log(MUA) signal. **b**, Average firing rate of the excitatory and inhibitory subpopulations of the complete network during the UP state for varying extracellular potassium concentration. **c**, *z*-score of the log(MUA) standard deviation in the DOWN state for increasing extracellular potassium concentration. Error bars in **b** and **c** represent the corrected sample standard deviation. Computations are made across five different simulations with distinct realizations of the connectivity matrix and external input. ρ denotes the Pearson correlation coefficient.

(Fig. 1a, bottom) exhibit clear slow oscillations, which reflect the cyclic time course of the synaptic currents flowing within the network and, at the same time, the firing activity of neurons.

The UP states shown in Fig. 1a are driven by background synaptic activity impinging stochastically on each neuron, coming from their presynaptic neighbours. The main way in which this background synaptic noise can vary is through changes in the excitability of the local network. To modify the excitability (ignoring external inputs), and thus change the background synaptic noise, we varied the resting membrane potential of all neurons by acting on the equilibrium potential of potassium, which plays the largest role in establishing the neuron's resting potential. This can be replicated experimentally by modifying the concentration of potassium in the extracellular medium, $[K^+]_o$. In fact, recordings performed in cats during transitions from slow-wave to REM sleep showed an enhancement of $[K^+]_o$ (ref. 30), suggesting its influence in neuronal excitability and network dynamics. In our model we increased $[K^+]_o$ from 2.4 mM to 7.5 mM, examining its effect on the dynamics of the individual neurons. The firing rate during the UP states, shown in Fig. 1b for both excitatory and inhibitory neurons, reveals that the firing activity of both neuron types increases with $[K^+]_o$. Note that inhibition overcomes excitation for high excitability, preventing runaway activity that would otherwise appear in this recurrently connected model network.

To establish the relationship between network excitability and the initiation of UP states, we next quantify the activity of the network during the DOWN states (which is small but non-negligible). This activity is estimated by the log(MUA), which is known to correlate with spiking activity[28,29]. Variability in this quantity during the DOWN states can thus be associated with background synaptic noise. We compute the standard deviation of the log(MUA) during the DOWN states as a function of $[K^+]_o$. The result, shown in Fig. 1c, reveals a clear increase of the standard deviation as the extracellular potassium level rises (with a high linear correlation, ρ, and low p-value) . We thus identify the excitability, controlled by $[K^+]_o$, with the noise acting on the network.

The response of the network to an increase in excitability is shown in Fig. 2a. The figure depicts the temporal evolution of the membrane potential of a representative neuron of the model network for three different values of the extracellular potassium concentration. For low $[K^+]_o$ (top panel) the excitability level is small, and consequently the initiation of UP states is infrequent. As the excitability increases (middle and bottom panels of Fig. 2a) the UP events become more frequent, owing to higher noise levels, and the firing rate during the UP state also increases (in agreement with Fig. 1b).

We next examine how the variability of the oscillatory dynamics depends on noise (excitability), by computing the coefficient of variation of the durations of the UP and DOWN events. As shown in Fig. 2b, for low excitability levels, the variability of the UP phase duration is basically constant, in agreement with our assumption that termination is essentially deterministic unless noise is too large. In contrast, the variability of the DOWN phase duration decreases sharply with noise for low noise levels, growing again when noise dominates the dynamics. The coefficient of variation (CV) of the full cycle duration (Fig. 2c) follows closely that of the DOWN state, showing a clear minimum for intermediate noise (excitability), which is the main hallmark of stochastic coherence. This behaviour is not due to the concomitant increase in firing rate arising from growing excitability (Fig. 1b): as shown in the Supplementary Section 3, increasing the external noise acting on the neurons produces the same effect, with essentially no variation in the firing rate.

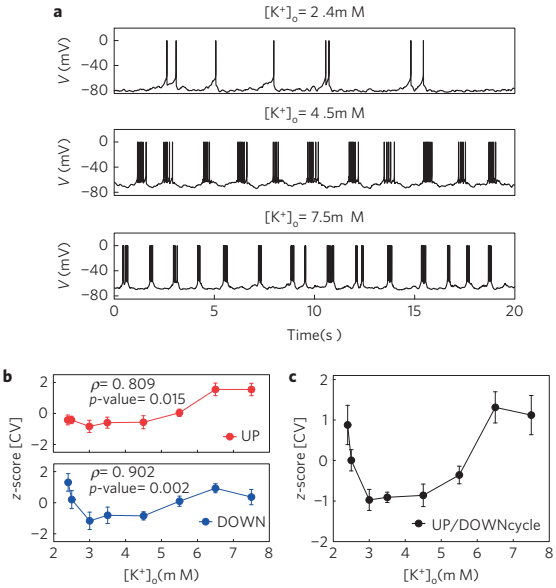

Figure 2 | Stochastic coherence in a cortical network model. a, Temporal evolution of the membrane potential of a representative excitatory neuron of the network for three different values of the extracellular potassium concentration $[K^+]_o$. **b**, Coefficient of variation (CV) of the duration of the UP and DOWN events (red and blue, respectively). The Pearson coefficient ρ and the p-value quantify the correlation between each CV and the one shown in **c**, and the statistical significance of such correlation, respectively. **c**, CV of the duration of the full UP/DOWN cycle. Note that z-scores are shown in the y axes of **b** and **c**. In those panels, error bars denote corrected sample standard deviation.

Evidence in cortical slices

To validate experimentally the prediction made by our computational model we turned to *in vitro* cortical slices of ferret visual cortex, which generate UP/DOWN state transitions spontaneously[6,7,31]. We studied the rhythmic activity patterns generated under various levels of synaptic noise by varying the extracellular potassium concentration $[K^+]_o$ (Fig. 3a), as discussed in the previous section. Spontaneous slow oscillations were recorded at extracellular potassium concentrations ranging from 1 mM to 7 mM (ref. 7) (see Supplementary Section 2 for experimental details). These values are of the same order of magnitude of the potassium levels found typically *in vivo*, located around 3 mM (refs 20,32,33).

First, we tested whether an increase of the extracellular potassium concentration led to an increase in the background noise of the network, as measured by the standard deviation of the log(MUA) during the DOWN states. Figure 3b confirms that this is indeed the case. The response of the population firing rate, measured again in terms of the log(MUA), is shown in Fig. 3c for three different potassium levels. As expected, higher potassium leads to more frequent UP states. To quantify the variability in the duration of the complete UP/DOWN cycle, we evaluated the coefficient of variation of that quantity as a function of the potassium level. As shown in Fig. 3d, all the experimental trials ($N = 13$ slices) exhibit a minimum in the variability for an intermediate excitability level, although the minima occur at slightly different extracellular potassium concentrations across slices. Differences across slices and experiments may arise due to distinct basal excitability levels secondary to intrinsic connectivity. To account for these differences, we aligned the level of potassium to place the minima of all trials at zero, and calculated the average z-score of the CVs. The result, plotted in Fig. 3e, shows a minimum variability for an intermediate level of excitability, thus confirming the predicted existence of stochastic coherence. Note that the normalization implicit in the z-score computation does not change the relationship between the dependent variables and $[K^+]_o$. The results also show that the CV of the UP state is much less dependent on the excitability level than that of the DOWN state for low excitability (Fig. 3f), in qualitative agreement with the modelling results. Taken together, our experiments confirm that the network activity acts as a collective order parameter that controls the regularity of the global rhythm.

Noise-induced spatial memory

The neuronal network underlying the emergence of UP/DOWN dynamics in our model is organized in space: the connection probability between pairs of neurons is higher the closer the neurons are to each other (see Methods). This gives the UP states a propagative character: noise-driven initiation of the neuronal activity occurs at a given point in the network, and propagates away from it with a speed that depends on the strength of the synaptic coupling and on the excitatory/inhibitory balance[17]. We thus ask what is the effect of background synaptic noise, and of the associated noise-induced regularity, on the spatiotemporal organization of the UP/DOWN dynamics. In fact, previous theoretical studies[34]

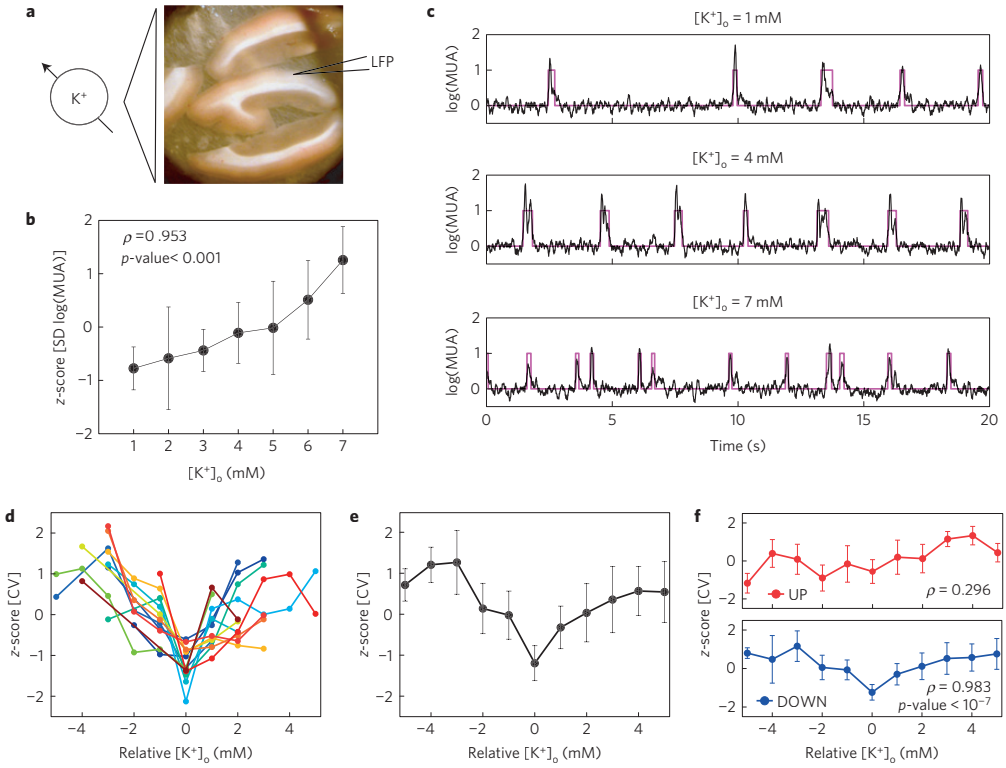

Figure 3 | Experimental evidence of stochastic coherence in the cortical tissue. a, Illustration of the experimental procedure: three visual cortex slices maintained in an interface recording chamber *in vitro*. **b**, Effect of varying extracellular potassium concentration $[K^+]_o$ on the standard deviation of the log(MUA) during the DOWN states. **c**, Typical time traces of the log(MUA) for three different levels of $[K^+]_o$. **d**, CV of the UP/DOWN cycle duration versus $[K^+]_o$ for all the experimental trials ($N=13$ slices). **e**, Average CV of the UP/DOWN cycle duration. **f**, Average CV of the individual durations of the UP and DOWN states versus $[K^+]_o$. To account for variability across experiments, in **d**–**f** the curves are shifted horizontally so that the CV minima of the UP/DOWN cycle are aligned to relative $[K^+]_o = 0$. Error bars in **b**,**e**,**f** correspond to the corrected sample standard deviation.

have suggested the existence of noise-induced memory in spatially extended systems with non-collective excitability, when operating in a regime of stochastic coherence.

To test whether our system can exhibit noise-induced spatial memory, we examined the spatiotemporal behaviour of our neuronal network model for increasing excitability levels. To capture clear UP wavefronts, we decreased the speed of propagation by reducing the spread of the excitatory connectivity in the model. The results are presented in Fig. 4a–c, which shows the wavefronts of the UP states exhibited by the model network (aligned horizontally so that they are superimposed in time) for three different amounts of extracellular potassium concentration (corresponding to three levels of excitability, and thus of background synaptic noise). The wavefronts are shown as contour plots computed over the spike-time histograms of groups of 40 consecutive neurons spanning the entire array. These plots suggest that the propagation of UP states is rather irregular for both low and high excitability (noise), whereas it follows a well-defined spatial pattern with clear initiation sites for intermediate noise levels. This is quantified in terms of the spatial consistency (SC) of the UP wavefronts, which is inversely related to the amount of spatial dispersion among the wavefronts shown in Fig. 4a–c (see Methods). This quantity exhibits a clear maximum as the potassium concentration increases, as shown in Fig. 4d. On the other hand, the temporal dispersion of the initiation events (as quantified by the CV) shows a clear minimum as the excitability increases. Therefore, our model predicts the existence of noise-induced spatial memory in the propagation of UP states for intermediate levels of background synaptic noise, which concurs with the regularity of the collective dynamics.

To verify this theoretical prediction, we measured the electrical activity of cortical slices with the electrode array shown in Fig. 5a–c (see Supplementary Section 2). This set-up allows us to monitor the spatiotemporal dynamics of the LFP exhibited by the cortical slice, and we do so for varying levels of extracellular potassium. An example of the behaviour of the tissue for a given experimental trial is depicted in Fig. 5d, again for three different levels of excitability. As we did with the modelling results, we quantified the spatial consistency of the UP wavefronts as described in the Methods. This measure is shown in the colour maps of Fig. 5d for a given experiment. The plot reveals that the UP wavefronts follow more regular patterns of propagation (dark red areas) for an intermediate excitability level, as predicted by our computational model. The behaviour of this spatial consistency for varying extracellular potassium levels is negatively correlated with the temporal dispersion (coefficient of variation) of the UP/DOWN cycle durations, as illustrated in Fig. 5e, in agreement with the theoretical prediction. An analysis of the statistical significance of the curves shown in Fig. 5e using mixed-effects modelling[35] allows us to reject the null hypothesis that potassium affects neither CV ($p < 10^{-10}$) nor SC ($p < 0.005$). This supports our conclusion

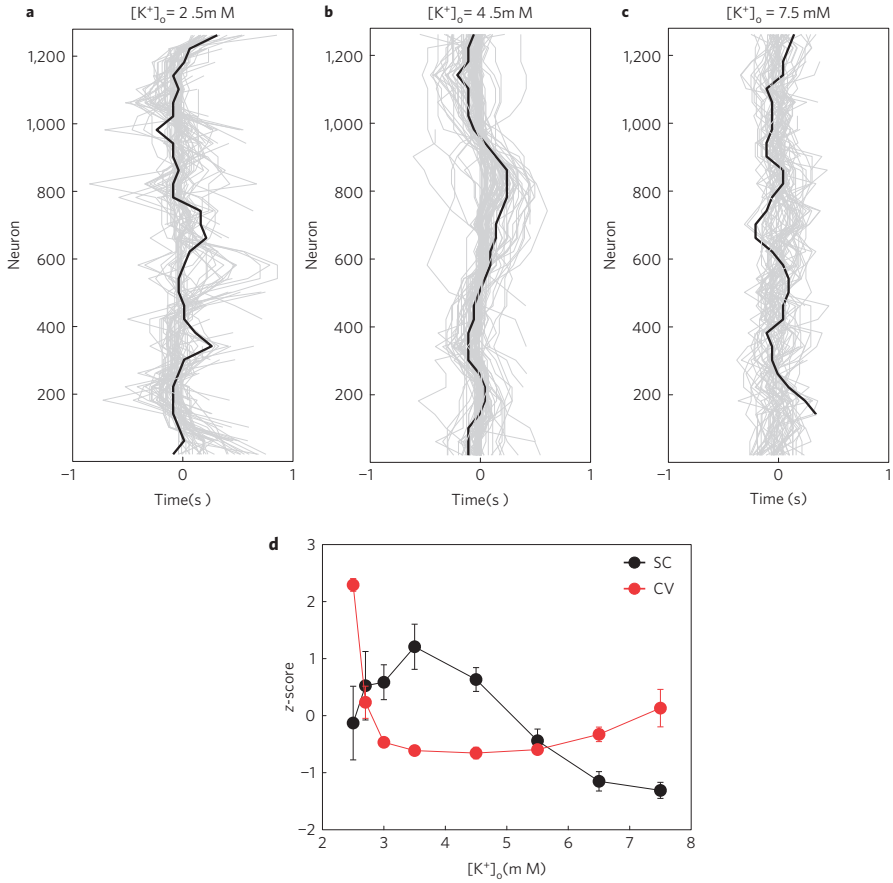

Figure 4 | Noise-induced spatial memory of UP-state initiation in the model. a–c, UP wavefronts (grey) centred at the origin as they propagate through the network, for three different excitability levels, controlled by the extracellular potassium concentration $[K^+]_o$. Specific wavefronts are highlighted in black. **d**, Spatial consistency (SC) of the UP waves and coefficient of variation (CV) of the cycle duration for increasing $[K^+]_o$. Note that this plot differs from Fig. 2c, because the connectivity between excitatory neurons has been decreased to better capture the propagation of the UP state through the network. Error bars in **d** represent corrected sample standard deviation.

that potassium (noise) affects both the temporal and the spatial dispersion of the UP/DOWN dynamics.

Physiological implications

It is well known that excitable systems (of which neurons are an example) can tune noise to enhance the regularity of their pulsing dynamics[15,16,36] at a characteristic timescale that is intrinsic to the system[37], instead of being imposed externally[38–44]. This effect has been observed in single neurons[45] and in the somatosensory pathway of anaesthetized cats[46] in response to *ad hoc* noisy inputs. In contrast to these works, here we have studied a purely cortical *in vitro* system under the influence of its own intrinsic noise, operating in a dynamic regime of slow oscillations that mimic those during slow-wave sleep and anaesthesia. Our results reveal that an intermediate amount of background noise maximizes the regularity of the UP/DOWN cycle. Modulating the regularity of these slow oscillations, which are an emerging property of the network, could facilitate the control of cortical information processing, by enabling mechanisms such as communication through coherence[47,48], or in general any mechanism that requires a periodic information carrier. Differently from other studies[23,49] that consider a white noise added to the membrane voltage, in our model the source of noise arises within the network, in the form of irregular presynaptic spike trains affecting all neurons of the network, and coming from neighbouring areas. This noise can be tuned experimentally via the membrane excitability of the individual neurons, determined by the potassium concentration $[K^+]_o$ in the extracellular medium. In this scenario, population activity appears as a collective phenomenon that underlies the control of rhythmicity.

Both the network model and the experimental recordings confirm that slow UP/DOWN rhythms are modulated by random fluctuations, and achieve a maximum periodicity at an intermediate amplitude of those fluctuations. At low excitability levels, the probability of eliciting an UP state is low, and the occurrence of these events fluctuates strongly with time, giving rise to high variability in the durations of the DOWN states. On the other hand, for high levels of excitability, the refractory period can be overcome more easily (that is, the system is re-excited sooner following the UP termination). This is in agreement with the behaviour observed in the transition from sleep to awake, or from deep to light anaesthesia[11], where the UP/DOWN transitions become more frequent and irregular. Between the two extremes, the UP

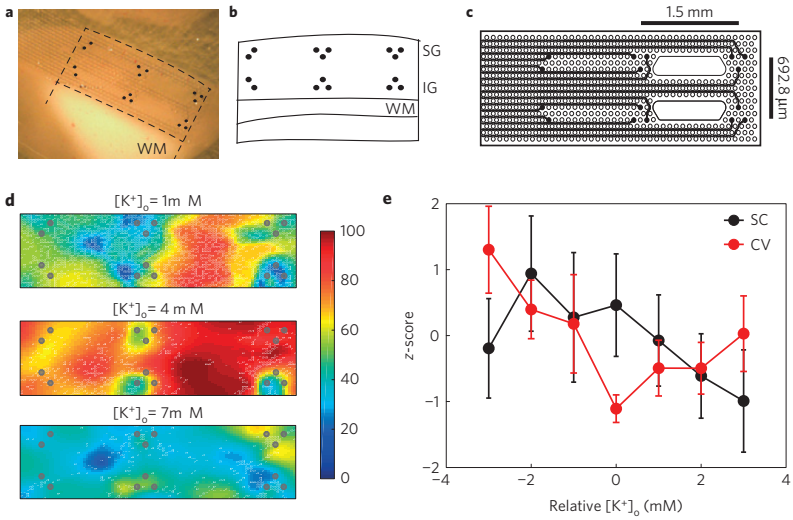

Figure 5 | Noise-induced spatial memory of UP-state initiation events in cortical slices. a, Illustration of our flexible array with sixteen electrodes (black dots) superimposed on a visual cortex slice. **b**, Scheme of the recording configuration showing the location of the different electrodes on the slice (supragranular layers, SG, and infragranular layers, IG) with respect to the white matter (WM). **c**, Scheme of the two-dimensional electrode array and distances between groups of electrodes. **d**, Colour-coded spatial consistency of the UP wavefronts (as a percentage, see Methods) for three different levels of extracellular potassium concentration in a typical slice. The grey circles indicate the location of the electrodes. **e**, *z*-score values of the spatial consistency (SC) and temporal coefficient of variation (CV) across the set of experiments ($N=8$). All $[K^+]_o$ values are referred to the location of the CV minimum for each experiment before averaging. Error bars show the corrected sample standard deviation across experiments.

states are consistently evoked at a similar phase of the DOWN state, and a recurrent collective period emerges. The specifics of this regular UP/DOWN regime depend on the balance between recurrent excitation and inhibition[28].

These results shed light on the self-regulation of cortical dynamics across different states of excitability, and reveal the existence of a regime of collective stochastic coherence leading to a maximal regularity of the dynamics for intermediate excitability. This is an emerging behaviour reminiscent of the phenomenon of coherence resonance, which has been reported in a large variety of physical and chemical excitable systems over the years[16]. In contrast with those previous studies, however, the effect described here is an emerging property of the network, arising from the collective interaction between the neurons. Given the stochastic and intrinsically emerging character of brain function, our results might be evidence of the functional benefits of noise in the activity of the central nervous system.

Methods

Methods and any associated references are available in the online version of the paper.

Received 24 June 2015; accepted 23 March 2016;
published online 2 May 2016

References

1. Enright, J. T. Temporal precision in circadian systems: a reliable neuronal clock from unreliable components? *Science* **209,** 1542–1545 (1980).
2. Garcia-Ojalvo, J., Elowitz, M. B. & Strogatz, S. H. Modeling a synthetic multicellular clock: repressilators coupled by quorum sensing. *Proc. Natl Acad. Sci. USA* **101,** 10955–10960 (2004).
3. Sanchez-Vives, M. V. & Mattia, M. Slow wave activity as the default mode of the cerebral cortex. *Arch. Ital. Biol.* **152,** 147–155 (2014).
4. Steriade, M., Nuñez, A. & Amzica, F. A novel slow (<1 Hz) oscillation of neocortical neurons *in vivo*: depolarizing and hyperpolarizing components. *J. Neurosci.* **13,** 3252–3265 (1993).
5. Stern, E. A., Kincaid, A. E. & Wilson, C. J. Spontaneous subthreshold membrane potential fluctuations and action potential variability of rat corticostriatal and striatal neurons *in vivo*. *J. Neurophysiol.* **77,** 1697–1715 (1997).
6. Shu, Y., Hasenstaub, A. & McCormick, D. A. Turning on and off recurrent balanced cortical activity. *Nature* **423,** 288–293 (2003).
7. Sanchez-Vives, M. V. & McCormick, D. A. Cellular and network mechanisms of rhythmic recurrent activity in neocortex. *Nature Neurosci.* **3,** 1027–1034 (2000).
8. Compte, A. *et al*. Spontaneous high-frequency (10–80 Hz) oscillations during up states in the cerebral cortex *in vitro*. *J. Neurosci.* **28,** 13828–13844 (2008).
9. Mattia, M. & Sanchez-Vives, M. V. Exploring the spectrum of dynamical regimes and timescales in spontaneous cortical activity. *Cogn. Neurodynam.* **6,** 239–250 (2012).
10. Gluckman, B. J. *et al*. Stochastic resonance in a neuronal network from mammalian brain. *Phys. Rev. Lett.* **77,** 4098–4101 (1996).
11. Deco, G., Martí, D., Ledberg, A., Reig, R. & Sanchez-Vives, M. V. Effective reduced diffusion-models: a data driven approach to the analysis of neuronal dynamics. *PLoS Comput. Biol.* **5,** e1000587 (2009).
12. Steriade, M., Timofeev, I. & Grenier, F. Natural waking and sleep states: a view from inside neocortical neurons. *J. Neurophysiol.* **85,** 1969–1985 (2001).
13. Parga, N. & Abbott, L. F. Network model of spontaneous activity exhibiting synchronous transitions between up and down states. *Front. Neurosci.* **1,** 57–66 (2007).
14. Bazhenov, M., Timofeev, I., Steriade, M. & Sejnowski, T. J. Model of thalamocortical slow-wave sleep oscillations and transitions to activated states. *J. Neurosci.* **22,** 8691–8704 (2002).
15. Pikovsky, A. S. & Kurths, J. Coherence resonance in a noise-driven excitable system. *Phys. Rev. Lett.* **78,** 775–778 (1997).
16. Lindner, B., Garcia-Ojalvo, J., Neiman, A. & Schimansky-Geier, L. Effects of noise in excitable systems. *Phys. Rep.* **392,** 321–424 (2004).
17. Compte, A., Sanchez-Vives, M. V., McCormick, D. A. & Wang, X.-J. Cellular and network mechanisms of slow oscillatory activity (<1 Hz) and wave propagations in a cortical network model. *J. Neurophysiol.* **89,** 2707–2725 (2003).
18. Holcman, D. & Tsodyks, M. The emergence of up and down states in cortical networks. *PLoS Comput. Biol.* **2,** e23 (2006).
19. Mejias, J. F., Kappen, H. J. & Torres, J. J. Irregular dynamics in up and down cortical states. *PLoS ONE* **5,** e13651 (2010).

20. Amzica, F., Massimini, M. & Manfridi, A. Spatial buffering during slow and paroxysmal sleep oscillations in cortical networks of glial cells *in vivo*. *J. Neurosci.* **22,** 1042–1053 (2002).
21. McCormick, D. A. Cholinergic and noradrenergic modulation of thalamocortical processing. *Trends Neurosci.* **12,** 215–221 (1989).
22. Romcy-Pereira, R. N., Leite, J. P. & Garcia-Cairasco, N. Synaptic plasticity along the sleep-wake cycle: implications for epilepsy. *Epilepsy Behav.* **14,** 47–53 (2009).
23. Han, S. K., Yim, T. G., Postnov, D. E. & Sosnovtseva, O. V. Interacting coherence resonance oscillators. *Phys. Rev. Lett.* **83,** 1771–1774 (1999).
24. Balenzuela, P. & García-Ojalvo, J. Role of chemical synapses in coupled neurons with noise. *Phys. Rev. E* **72,** 021901 (2005).
25. Bhattacharjee, A., von Hehn, C., Mei, X. & Kaczmarek, L. Localization of the Na-activated K channel slick in the rat central nervous system. *J. Comp. Neurol.* **484,** 80–92 (2005).
26. Wang, X.-J., Liu, Y., Sanchez-Vives, M. V. & McCormick, D. A. Adaptation and temporal decorrelation by single neurons in the primary visual cortex. *J. Neurophysiol.* **89,** 3279–3293 (2003).
27. Sanchez-Vives, M. V., Nowak, L. G. & McCormick, D. A. Cellular mechanisms of long-lasting adaptation in visual cortical neurons *in vitro*. *J. Neurosci.* **20,** 4286–4299 (2000).
28. Sanchez-Vives, M. V. *et al*. Inhibitory modulation of cortical up states. *J. Neurophysiol.* **104,** 1314–1324 (2010).
29. Mattia, M. & Del Giudice, P. Population dynamics of interacting spiking neurons. *Phys. Rev. E* **66,** 051917 (2002).
30. Satoh, T., Watabe, K. & Eguchi, K. Enhancement during REM sleep of extracellular potassium ion activity in the reticular formation. *Brain Res.* **174,** 180–183 (1979).
31. Cossart, R., Aronov, D. & Yuste, R. Attractor dynamics of network up states in the neocortex. *Nature* **423,** 283–288 (2003).
32. Yamaguchi, T. Cerebral extracellular potassium concentration change and cerebral impedance change in short-term ischemia in gerbil. *Bull. Tokyo Med. Dental Univ.* **33,** 1–8 (1986).
33. Bazhenov, M., Timofeev, I., Steriade, M. & Sejnowski, T. J. Potassium model for slow (2–3 hz) *in vivo* neocortical paroxysmal oscillations. *J. Neurophysiol.* **92,** 1116–1132 (2004).
34. Chialvo, D., Cecchi, G. & Magnasco, M. Noise-induced memory in extended excitable systems. *Phys. Rev. E* **61,** 5654–5657 (2000).
35. Baayen, R. H., Davidson, D. J. & Bates, D. M. Mixed-effects modeling with crossed random effects for subjects and items. *J. Mem. Lang.* **59,** 390–412 (2008).
36. Sagués, F., Sancho, J. & García-Ojalvo, J. Spatiotemporal order out of noise. *Rev. Mod. Phys.* **79,** 829–882 (2007).
37. Gang, H., Ditzinger, T., Ning, C. & Haken, H. Stochastic resonance without external periodic force. *Phys. Rev. Lett.* **71,** 807–810 (1993).
38. Bulsara, A., Jacobs, E., Zhou, T., Moss, F. & Kiss, L. Stochastic resonance in a single neuron model. *J. Theor. Biol.* **152,** 531–555 (1991).
39. Longtin, A. Stochastic resonance in neuron models. *J. Stat. Phys.* **70,** 309–327 (1993).
40. Douglass, J. K., Wilkens, L., Pantazelou, E. & Moss, F. Noise enhancement of information transfer in crayfish mechanoreceptors by stochastic resonance. *Nature* **365,** 337–340 (1993).
41. Levin, J. E. & Miller, J. P. Broadband neural encoding in the cricket cereal sensory system enhanced by stochastic resonance. *Nature* **380,** 165–168 (1996).
42. Collins, J. J., Imhoff, T. T. & Grigg, P. Noise-enhanced information transmission in rat SA1 cutaneous mechanoreceptors via aperiodic stochastic resonance. *J. Neurophysiol.* **76,** 642–645 (1996).
43. Stacey, W. C. & Durand, D. M. Stochastic resonance improves signal detection in hippocampal ca1 neurons. *J. Neurophysiol.* **83,** 1394–1402 (2000).
44. McDonnell, M. D. & Ward, L. M. The benefits of noise in neural systems: bridging theory and experiment. *Nature Rev. Neurosci.* **12,** 415–426 (2011).
45. Gu, H., Yang, M., Li, L., Liu, Z. & Ren, W. Experimental observation of the stochastic bursting caused by coherence resonance in a neural pacemaker. *Neuro Rep.* **13,** 1657–1660 (2002).
46. Manjarrez, E. *et al*. Internal stochastic resonance in the coherence between spinal and cortical neuronal ensembles in the cat. *Neurosci. Lett.* **326,** 93–96 (2002).
47. Fries, P. Rhythms for cognition: communication through coherence. *Neuron* **88,** 220–235 (2015).
48. Barardi, A., Sancristóbal, B. & Garcia-Ojalvo, J. Phase-coherence transitions and communication in the gamma range between delay-coupled neuronal populations. *PLoS Comput. Biol.* **10,** e1003723 (2014).
49. Horikawa, Y. Coherence resonance with multiple peaks in a coupled FitzHugh-Nagumo model. *Phys. Rev. E* **64,** 031905 (2001).

Acknowledgements

We thank A. Compte for useful comments, and our colleagues from CSIC-CNM in Barcelona (X. Villa, R. Villa, G. Gabriel) for providing the recording arrays used in Fig. 5. This work was supported by the Ministerio de Economia y Competividad and FEDER (Spain, projects FIS2012-37655-C02-01, to J.G.-O., and BFU2014-52467-R, to M.V.S.-V.) and EU project CORTICONIC (contract number 600806, to M.V.S.-V.). B.R. was supported by the FPI programme associated to BFU2011-27094 (Spain, Ministerio de Economia y Competividad). J.G.-O. acknowledges support from the ICREA Academia programme and from the Generalitat de Catalunya (project 2014SGR0974).

Author contributions

B.S., M.V.S.-V. and J.G.-O. conceived the research. B.S. implemented the mathematical model. B.S. and P.B. analysed the data. B.R. performed the experiments. M.V.S.-V. and J.G.-O. supervised the work. B.S., M.V.S.-V. and J.G.-O. wrote the manuscript. All authors revised and approved the text.

Additional information

Supplementary information is available in the online version of the paper. Reprints and permissions information is available online at www.nature.com/reprints. Correspondence and requests for materials should be addressed to M.V.S.-V. or J.G.-O.

Competing financial interests

The authors declare no competing financial interests.

Methods

Description of the network model. We consider a network composed of 1,280 neurons, 80% of which are excitatory whereas the remaining 20% are inhibitory[50]. The neurons, modelled as described in Supplementary Section 1, were arranged in two open one-dimensional chains, one for the excitatory population and the other for the inhibitory population, with one inhibitory neuron placed every four adjacent excitatory neurons. All connections between cells are chemical synapses (no gap junctions are considered), and each neuron connects with 20 ± 5 other neurons. The two chains are 5 mm long, with no empty space between adjacent neurons. We use the coupling architecture introduced by ref. 17, in which the probability that two neurons are connected is determined by the distance x between them, according to a Gaussian probability distribution $P(x) = e^{-x^2/2\sigma^2}/\sqrt{2\pi\sigma^2}$, with no autapses being allowed. The standard deviation σ is set to 250 μm for the excitatory connections, and 125 μm for the inhibitory connections. As a reference, the size of an excitatory neuron can be considered ∼5 μm (50 times smaller than its σ) and that of an inhibitory neuron ∼19 μm (about 13 times smaller than its σ). The neurons are also driven by random spike trains drawn from a Poisson distribution, representing the effect of neurons that are not included explicitly in the network. Experimentally, this random input corresponds to fluctuations in the excitability of neurons neighbouring the area where the slow oscillation is taking place.

Estimation of the local field potential (LFP). The local field potential (LFP) is computed as the sum of the absolute values of the excitatory and inhibitory synaptic currents acting on the excitatory neurons[51–53]:

$$\mathrm{LFP} = R_e \sum (|I_{\mathrm{AMPA}}| + |I_{\mathrm{NMDA}}| + |I_{\mathrm{GABA}}|) \quad (1)$$

The terms I_{AMPA} and I_{NMDA} account for both the external excitatory heterogeneous Poisson spike train and the recurrent excitatory synaptic current due to network connectivity. In turn, I_{GABA} corresponds to the recurrent inhibitory synaptic current. R_e represents the resistance of a typical electrode used for extracellular measurements, here chosen to be 1 MΩ. The LFP is sampled at 1 kHz. The initiation and termination of the UP and DOWN states were identified by means of the log(MUA), a measure extracted from the power spectrum of the LFP (equation (1)) within the frequency range 0.2–0.5 kHz (see next section for a complete description).

Estimation of the log(MUA). The multiunit activity (MUA) is estimated as the power change in the Fourier components of the recorded (or simulated) LFP at high frequencies. The time-dependent MUA is computed from the power spectrum in 50-ms windows, each frequency normalized by the corresponding amplitude of the power spectrum computed over the whole time series, and averaged within the 0.2–1.5 kHz band (0.2–0.5 kHz in the simulations, except in Supplementary Fig. 1B, where the range 0.1–0.5 kHz was used). The MUA signal is then logarithmically scaled and smoothed by a moving average with a sliding window of 80 ms (ref. 54). The UP and DOWN states were singled out by setting a threshold in the log(MUA) signal. The threshold was set between peaks of the bimodal distributions of log(MUA), corresponding to the UP and DOWN states. The peak related to the DOWN state was used as reference, setting there $\log(\mathrm{MUA}) = 0$. The z-score of the log(MUA) is computed by subtracting from each SD curve its mean value for all simulations/experiments across the extracellular potassium range, normalizing it by its standard deviation, and averaging the results across replicates.

Spatial consistency analysis. To quantify the regularity of the UP waves we proceed as follows. First, after detection of every UP state, we compute the times at which each electrode crosses a given threshold (as mentioned in the section above). Electrodes whose signals are very noisy are not used for the analysis. On the other hand, we consider only those UP states that are detected in all three columns in which the array is arranged (see Fig. 5a,b)—but not necessarily in all the electrodes in each column. This condition enables us to consider those waves that propagate through all three columns across the slice. We transform those first-passage times into time lags by subtracting the initial time at which the UP wave is first detected somewhere within the array. If one of the propagating UP states is not detected in one of the electrodes used for the analysis, we assign to that electrode, for that particular wave, a time lag that is an average from other time lags belonging to the five most similar propagating wavefronts.

Next, we interpolate the time lags using a thin-plate spline by means of the MATLAB function tpaps. The new data points form a grid of 105×49 points. Hence we have as many grids as detected UP states. Each grid is further subdivided into a coarse matrix of 15×7 cells. We then compute the correlation between each one of these cells with the equivalent cell belonging to the other detected UP waves. Therefore, the correlation between two UP waves leads to $105 (= 15 \times 7)$ correlation coefficients, and the correlation between N UP waves leads to $(N(N-1)/2) \times 105$ coefficients.

Finally, we compute the spatial consistency (SC) of the wavefronts in terms of the percentage of highly correlated matrix elements (>0.7) between all wave pairs for each of the cells. The colour maps in Fig. 5d represent the spatial consistency for all cells in the 15×7 coarse matrix. The same approach is followed in our one-dimensional model, where the time lags are obtained from 16 clusters of consecutive excitatory neurons covering the entire one-dimensional model network, and an interpolation is performed to generate a vector of 49 cells.

References

50. Mountcastle, V. B. *Perceptual Neuroscience: The Cerebral Cortex* (Harvard Univ. Press, 1998).
51. Mazzoni, A., Panzeri, S., Logothetis, N. K. & Brunel, N. Encoding of naturalistic stimuli by local field potential spectra in networks of excitatory and inhibitory neurons. *PLoS Comput. Biol.* **4,** e1000239 (2008).
52. Berens, P., Logothetis, N. K. & Tolias, A. S. Local field potentials, BOLD and spiking activity–relationships and physiological mechanisms. Available at http://precedings.nature.com/documents/5216/version/1 (2010).
53. Buzsáki, G., Anastassiou, C. A. & Koch, C. The origin of extracellular fields and currents - EEG, ECoG, LFP and spikes. *Nature Rev. Neurosci.* **13,** 407–420 (2012).
54. Reig, R., Mattia, M., Compte, A., Belmonte, C. & Sanchez-Vives, M. V. Temperature modulation of slow and fast cortical rhythms. *J. Neurophysiol.* **103,** 1253–1261 (2010).

Appendix B

Manuscripts

Slow-waves in cortical slices: how spontaneous activity is shaped by laminar structure

Running title: Shaping of slow waves by cortical layers.

Cristiano Capone[1,2], Beatriz Rebollo[3], Alberto Muñoz[4], Xavi Illa[5,6], Paolo Del Giudice[2], Maria V. Sanchez-Vives[3,7], Maurizio Mattia[2]

[1] Phd Program in Physics, Sapienza University, Rome, Italy
[2] Istituto Superiore di Sanità, Rome, Italy
[3] IDIBAPS (Institut d'Investigacions Biomèdiques August Pi i Sunyer), Barcelona, Spain
[4] Universidad Complutense de Madrid, Madrid, Spain
[5] IMB-CNM-CSIC (Instituto de Microelectrónica de Barcelona), Universitat Autónoma de Barcelona, Barcelona, Spain
[6] CIBER-BBN, Networking Center on Bioengineering, Biomaterials and Nanomedicine, Zaragoza, Spain
[7] ICREA (Institucio Catalana de Recerca i Estudis Avançats), Barcelona, Spain

* Corresponding author: Maurizio Mattia, PhD
Istituto Superiore di Sanità
Viale Regina Elena 299
00161 Rome, Italy
Phone: + 39 06 49902513
E-mail: maurizio.mattia@iss.it

Figures: 8
Abstract (≤ 200 words): 200 words

Keywords (≥ 5): Slow waves; oscillations; cortical layers; in vitro recordings; computer models.

Author contributions: MM, CC, MVSV designed research; BR performed and MVSV supervised experimental research; CC performed and MM, PDG supervised simulations and analyses; AM, BR performed histology; XI, co-designed and fabricated the new electrode array; MM, PDG, CC, MVSV wrote the paper.

Abstract

Cortical slow oscillations (SO) of neural activity spontaneously emerge and propagate during deep sleep and anesthesia and are also expressed in isolated brain slices and cortical slabs. We lack full understanding of how SO integrate different structural levels underlying local excitability of cell assemblies and their mutual interaction. Here, we focus on ongoing slow waves (SWs) in ferret cortical slices reconstructed from a 16-electrodes array, designed to probe the neuronal activity at multiple spatial scales. In spite of the variable propagation patterns observed, we reproducibly found a smooth strip of loci leading the SW fronts, overlapped with cortical layers 4 and 5, along which Up states were the longest and displayed the highest firing rate. Propagation modes were uncorrelated in time, signaling a memoryless generation of SWs. All these features could be modeled by a multi-modular large-scale network of spiking neurons with a specific balance between local and intermodular connectivity. Modules work as relaxation oscillators with a weakly stable Down state and a peak of local excitability to model layers 4 and 5. These conditions allow for both optimal sensitivity to the network structure and richness of propagation modes, a potential neuronal substrate for dynamic flexibility in more general contexts.

Introduction

Propagating waves are a natural strategy to transfer information across the cortical web of neurons. For example, the processing of sensory stimuli by the brain is the result of a coordinated activity of all its cellular components, which are huge in number and distributed in space. Activation waves travelling across the cortical surface appears to be one of the possible ways in which such orchestration takes place (Ermentrout and Kleinfeld 2001; Sato et al. 2012). Travelling waves emerge in topologically organized media (Cross and Hohenberg 1993), where the nonlinear dynamics of its interacting elements contribute to generate complex and state-dependent responses to external stimulations: a way to implement sensory information processing. A wide body of literature supports this view, as activity waves elicited by sensory stimuli are invariantly found to propagate across the cortex of anesthetized animals (Bringuier et al. 1999; Jancke et al. 2004; Benucci et al. 2007; Xu et al. 2007; Stroh et al. 2013). This findings are corroborated by the similar spatiotemporal patterns of cortical activity measured in behaving animals (Rubino et al. 2006; Ferezou et al. 2007; Muller et al. 2014). Remarkably, these stimulus-evoked waves are not only a mere echo of the incoming input from the environment. Indeed, stimulus-evoked activations can continuously and cyclically propagate across the visual cortex even when sensory information does not change in time, as in the case of binocular rivalry induced by presenting to the two eyes dissimilar patterns (Lee et al. 2007). Moreover, perceptual waves spread well beyond primary sensory cortices giving rise to a self-sustained activity propagation which eventually involves other cortical areas at higher hierarchical levels, and can persist in time for fractions of seconds after stimulus presentation (Ferezou et al. 2007; Xu et al. 2007).

Hence it is not by chance that activation waves are spontaneously expressed by the cortical tissue also when it is kept isolated from the environment, as it happens in the intact brain of many species during slow-wave (SW) sleep (Cirelli and Tononi 2008; Siegel 2008) and under deep anaesthesia (Alkire et al. 2008). A default activity mode (Sanchez-Vives and Mattia 2014) which invariantly emerges also in the extreme condition of brain slices maintained *in vitro* (Sanchez-Vives and McCormick 2000; Wester and Contreras 2012). Despite the reproducibility of this SW activity, the ongoing spatiotemporal patterns composing this default mode display a high degree of dynamical richness. Indeed, *in vivo* SWs are endowed with a remarkable balance between stochastic and deterministic components. In this brain state, waves preferentially initiates in frontal cortex and propagates backward to parietal/occipital

cortical areas (Massimini et al. 2004; Mohajerani et al. 2010; Ruiz-Mejias et al. 2011; Stroh et al. 2013; Sheroziya and Timofeev 2014). On the other hand, these propagating wavefronts follow pathways widely distributed across the cortex with variable speeds. This variability is area-specific (Ruiz-Mejias et al. 2011), further highlighting that SW activity is shaped by the underlying structure of the cortex. The relationship between structure and SWs is corroborated also by recent findings showing that wavefront propagation is influenced by past experience (Han et al. 2008) and that activation variability is not a wandering between random activity patterns but rather it is the stochastic rehearsal of previously encoded sensory responses (Luczak et al. 2009).

Here we investigate the balance between global nonlinear dynamics supporting SW activity, the intrinsic richness of ongoing spatiotemporal patterns, and the sensitivity to the structure of the underlying cortical medium. More specifically, we focused on the laminar structure of the cortex, known to shape *in vitro* SWs (Sanchez-Vives and McCormick 2000; Wester and Contreras 2012). By clustering the phase-locked slow oscillations (SO) between high-firing (Up) and quiescent (Down) states across the cortical slices, we quantitatively characterized the large variability of SO ignition sites and wave propagation modes. Reconstructed travelling waves revealed *loci* across the slices, reproducibly leading the propagation of Up state onset. These loci were distributed along a smooth strip that, upon checking with anatomical reconstruction, largely overlapped layers 4 and 5. By matching semi-quantitatively large scale simulations of a multi-modular slice model to the measured slow-waves, we found that cell assemblies in this smooth excitable strip must work as relaxation oscillators, with finite-size fluctuations destabilizing an otherwise stable Down state. We also found that simulations reproduce the observed overlap between the excitable strip and the region with maximum firing rate and longest Up state durations, only if the intra- and inter-module coupling strengths are optimally balanced, thereby further strengthening the relationship between spontaneous activity and network structure.

Materials and Methods

Slice preparation and histology.

In vitro experiments were done on 0.4 mm thick visual cortical slices (areas 17, 18 and 19) from 5 to 10 month old male ferrets (*Mustela putorius furo*) that were anesthetized with sodium pentobarbital (40 mg/kg) and decapitated. Their brain were removed and placed in the cold (4-10^{o}C) cutting solution. Ferrets were cared in accordance with the European Union guidelines on protection of vertebrates used for experimentation (Strasbourg 3/18/1986) as well as approved by the local ethical committee. During cutting of slices on a vibratome, the tissue was place in a solution in which the NaCl was substituted with sucrose. Following transfer to the interface-style recording chamber (Fine Sciences Tools, Foster City, CA), the slices were incubated in 'traditional' slice solution containing 126 mM NaCl, 2.5 mM KCl, 2 mM $MgSO_4$, 1 mM $NaHPO_4$, 2 mM $CaCl_2$, 26 mM $NaHCO_3$ and 10 mM dextrose, aerated with 95% O_2, 5% CO_2 to a final pH of 7.4. After approximately 1 hour, the slice solution was modified to contain 1 mM $MgCl_2$, 1 mM $CaCl_2$ and 4 mM KCl (Sanchez-Vives and McCormick 2000). Bath temperature was maintained at 34-36^{o}C.

Extracellular multiple unit recordings were obtained with flexible arrays of 16 electrodes arranged in columns as in Fig. 1A (Illa et al. 2015). The multi electrode array (MEA) covered most of the area occupied by a cortical slice. It consisted of six groups of electrodes positioned to record electrophysiological activity from supra- and infra-granular layers (692μm apart) and from what should correspond to 3 different cortical columns (1500μm apart). The unfiltered field potential (raw signal) was acquired at 20 kHz with Multichannel System amplifier and digitized with a 1401 CED acquisition board and Spike2 software (Cambridge Electronic Design).

At the end of each experiment slices were fixed in paraformaldehyde (4%), cryoprotected in 30% sucrose solution in phosphate buffer (0.1 M, pH7.4), frozen in dry ice and cut in a Thermo Scientific MICROM HM 450 freezing sliding microtome. The sections (50 μm thick) were mounted in glass slides and Nissl stained, dehydrated, coverslipped and photographed. Layer limits were drawn according to the size and density of observed cells and the MEA position was superimposed on the basis of the identification of marks performed at the end of the recording session.

To check the reliability of the interpolation procedure introduced to investigate the relationship between spontaneous electrophysiological activity and network structure in the slice regions far from MEA position, we performed the same

experiments on 5 additional cortical slices including the simultaneous recordings from an additional extra electrode placed sequencially in 5 different location within the area covered by the MEA (see Supplementary Material for details).

MUA estimate and state detection

Up and Down states and multi-unit activity (MUA) were estimated from the recorded raw signals as in (Reig et al. 2010; Sanchez-Vives et al. 2010). Briefly, the power spectra from sliding windows of 5 ms of the raw signal were computed. MUA were estimated as the relative change of the power in the frequency band [0.2, 1.5] kHz. Average MUA following Up-to-Down transitions was used as reference value and set to 1. Such spectral estimate of the MUA was not affected by the electrode filtering properties and provided a good estimate of the relative firing rate of the pool of neurons nearby the electrode tip. We then smoothed log(MUA) performing a moving average with a sliding window of 80 ms. From the long-tailed histogram of log(MUA) (see Fig. 1B) an optimal threshold separating Up and Down activity states was set at 4 times the standard deviation (SD) of the Down peak. To avoid biases in the identification of wavefronts, the same threshold was used for each recording in the same slice, as all having similar Down peaks SD. This to avoid introducing biases among electrodes in the characterization of activation and silencing wavefronts. The threshold was also the same for detecting both Down-to-Up and Up-to-Down transitions.

Slow waves detection and reconstruction

Activation waves were detected when a Down-to-Up transition from multiple electrodes occurred within a time window ΔT initially chosen to 1 s. Then ΔT was iteratively reduced by a factor of 0.75, until each detected wave contained no more than one state transition per electrode. In order to recompose waves involving a subset of columns of electrodes wrongly detected as separated waves, a minimum inter-wave interval (IWI) was chosen and waves occurring within the IWI were considered as composing a single wave. The initial IWI was set to half the maximum time lag between initially detected waves. Then IWI was iteratively reduced by the 25% if collected waves included the same electrode columns more than once or if the number of time lags composing the wave size is larger than the number of electrodes. After each IWI reduction, wave recollection is recomputed. This iterative process ended once the IWI was neither reduced nor increased, or when the number of waves including the same electrode more than once was less than 10% of the total number of detected waves. The iteration was stopped if the number of recomposed waves in the first step of iteration was higher

than a reasonable value of expected waves, that is the median number of transition for each channel. Otherwise we may have an artefactual amplification of small waves. Waves including the same electrode more than once and waves with state transitions in less than 4 electrodes per column were rejected. Such constrain was dictated by the necessity to fully sample the slice area covered by the MEA in order to have reliable predictions about ongoing network activity also relatively far from the position of the electrodes.

Each wave was associated to an array T_t^i of relative time lags (where t = 1,...Wand i = 1,...N are the wave and the electrode indices), resulting from the difference between the detected state transition time in each electrode, and their average across electrodes. Such arrays of relative time lags, in turn composed the rows of the time lag matrix (TLM) showed in Figure 2A. TLM columns were grouped in 3 sets of electrodes, each related to a different electrode column of the MEA. We computed the average log(MUA) in each of these electrode column detecting Up/Down state transitions on these pooled signals relying on the same detection adopted for single electrodes. Those waves in which a Down-to-Up transition was detected in each of these columns was classified as "full", to distinguish them for the other remaining "partial" waves. Unless otherwise specified, only full waves were considered for the following analysis. In order to infer the wavefront time lags $T(x,y)$ in the slice regions not covered by the electrodes, we interpolated without smoothing such times with a thin-plate spline. For each wave only those electrodes with detected MUA state transitions were taken into account. From $T(x,y)$ the speed $V(x,y)$ was computed as

$$V(x,y) = \frac{1}{\sqrt{\left(\frac{\partial T(x,y)}{\partial x}\right)^2 + \left(\frac{\partial T(x,y)}{\partial y}\right)^2}}$$

Slow wave features characterization

We collected wave vectors describing full waves and clustered them using *k*-means algorithm to separate different modes of propagations characterized by different origin, speed and direction. In order to perform *k*-means clustering, we needed complete transition time vectors. We filled each empty entry in the vectors, that corresponds to a non recorded transition during a wave, with the average transition time recorded by the same electrode in the most similar 5 waves. The median error in the time lag of the "filled" elements estimated in this way was 30.0 ± 8.0 ms, one order of magnitude smaller than the characteristic time scale of wave propagation which typically took

more than 600 ms to cross the whole slice (see Supplementary Material). For each recording we grouped waves in 10 clusters. We rejected clusters, and relative waves, with a mean speed lower than 2 mm/s. This threshold value has been chosen starting from the observation that the distribution of the speed over all experiments (not shown) is well fitted by the sum of two distributions. These distributions are peaked just above and below such threshold, respectively. Of these two components, the one corresponding to the highest speeds is related to propagating modes described in the Results section. The other component with slowest speed seemed to be not associated to traveling activation wavefronts and for this reason we did not analyzed them. On average, 3 clusters for each experiment were rejected and the accepted ones were composed of 15 waves.

For each wave from an accepted cluster, we computed the vertical (V_x) and horizontal (V_y) components of the wavefront velocity from T(x,y) as

$$\begin{cases} V_x = \frac{1}{\frac{\partial T(x,y)}{\partial x}} \\ V_y = \frac{1}{\frac{\partial T(x,y)}{\partial y}} \end{cases}.$$

In order to characterize the spatiotemporal complexity of the identified waves we considered only in this case both full and partial waves described by the time series $\{T_t^i\}$ and partial waves and evaluated the correlation $AC(n)$ as a function of delay n as follows

$$AC(n) = \frac{1}{N}\sum_{i=1}^{N}\sum_{t=1}^{W-n}(T_{t+n}^i - \overline{T^i})(T_t^i - \overline{T^i}),$$

with N the number of electrodes and W the number of detected waves. $\overline{T^i} = \sum_{t=1}^{W} T_t^i$. Note that, lag n did not explicitly relate to the time but rather to the ordinal number of the detected wave.

Quantitative characterization of slow waves

For each wave an early propagation strip (EPS) was identified as the set of points where the wavefront tip at different times first occurred in the horizontal direction. In other words, EPS(x) was the vertical position y where the time-lag surface T(x,y) displayed a minimum at fixed x: $\mathrm{EPS}(x) = \arg\min_y T(x,y)$. EPSs were identified for all waves from accepted clusters. All the strips were convolved with a Gaussian kernel along the vertical direction and averaged to obtain a smoothed probability density function p(x,y). A cut-off to this density was further adopted by setting p(x,y) = 0 for p(x,y) <

0.75 $p_{max}(x)$, where $p_{max}(x)$ was the maximum of p(x,y) at a given x. After renormalizing this cut density average $\mathrm{EPS}(x) = \int y\, p(x,y) dy$. and its SD were finally computed.

For each electrode both the average Up state duration, and the maximum MUA during the Up state were computed for each wave in an accepted cluster. As for the time-lag surface T(x,y), these values were interpolated by a thin-plate spline allowing to obtain $T_{UP}(x,y)$ and MUA(x,y), respectively. From these surfaces, the curves where maximum Up duration and MUA can be found at different horizontal positions x ($\arg\max_y T_{Up}(x,y)$ and $\arg\max_y \mathrm{MUA}(x,y)$, respectively) were computed (see Figure 4C-E). The distances between these curves and EPS(x) at the horizontal locations of the electrodes in the array (n = 8) were computed to estimate histograms in Figure 4F-G.

We repeated the same analysis in additional set of similar experiments (n = 5 slices) using an extra electrode placed subsequently in 5 different positions far from other electrodes of the MEA (see Figure 2F and Supplementary Material), in which one recording were discarded due to data acquisition instability bringing to have n = 24 samples in the data set. For each SW the propagating wavefronts were computed relying on the thin-plate spline-based interpolation procedure described above. Such wavefronts were estimated both with and without the extra electrode (see Fig.2F and Supplementary Materials) to check the reliability by inspecting the resulting differences giving a measure of their misalignment in time. The same approach was used to estimate the measure error due to relying on the interpolation procedure in the identification of the EPS, and the strips in the slices where the Up state duration and the MUA are maximal (see Supplementary Material for further details).

To study the wave speed dependence of propagation modes (Fig. 4H-I), we computed separately the average speeds $V_L(S)$ and $V_R(S)$ along the average EPS curvilinear abscissa S in the leftward and rightward direction, respectively. We finally computed an asymmetry index as the speed difference $\Delta V(S) = V_R(S) - V_L(S)$. Similarly we also computed the gradient of Up state durations $dT_{Up}(S)/dS$. All these measures were sub-sampled in order to avoid spurious correlation effects. Decimated points were selected at steps ΔS = 0,21 mm, a length always greater than the decay constant of the autocorrelation of $T_{Up}(S)$.

To test the overlap between EPS and some specific laminar structures of the cortical slices we considered the region where the EPS density p(x,y) > 0.05. Thus we measured the portion of its area included in each layer (Fig. 7).

Where not specified averages across the n = 12 experiments are reported as mean mean ± standard deviation (SD).

All off-line analyses were performed using MATLAB (The MathWorks, Natick, MA).

Theory, models and simulations.

We used both network models of integrate-and-fire (IF) neurons and a minimal rate model to set the simulation parameters. The *in silico* slice is a multi-modular interconnected network of spiking neurons. Similarly to (Mattia et al. 2013), cortical modules were composed of 350 leaky integrate-and-fire (LIF) excitatory (E, 80%) and inhibitory (I, 20%) neurons with spike frequency adaptation (SFA). Membrane potential V(t) of LIF neurons evolved according to $\frac{dV(t)}{dt} = -\frac{V(t)}{\tau_\alpha} + I_{syn}(t) - I_{AHP}(t)$, where $I_{syn}(t)$ was the synaptic incoming current and τ_α was the membrane decay constant (τ_E = 20 ms and τ_I = 10 ms). Spikes were emitted when V(t) crossed a 20 mV threshold, after which a 15 mV reset potential was set for an absolute refractory period of 10 ms (6 ms) for excitatory (inhibitory) neurons. $I_{AHP}(t)$ was the activity-dependent after-hyperpolarizing potassium current acting as a fatigue mechanism modeling SFA for excitatory neurons: $\frac{dI_{AHP}(t)}{dt} = -\frac{I_{AHP}(t)}{\tau_{AHP}} + g_{AHP}\sum_k \delta(t - t_k)$, with τ_{AHP} = 1 s and g_{AHP} = 0.06 mV/s. The $\delta(t-t_k)$ were the spikes emitted by the neuron.

Synaptic transmission was instantaneous, and $I_{syn}(t) = \sum_{jk} J_j\, \delta(t - t_{kj} + \delta_j) + \sum_k J_{ext,k}\delta(t - t_{ext,k})$. The k-th spike emitted at $t = t_{jk}$ by the local presynaptic neuron j affected the postsynaptic membrane potential with a synaptic efficacy J_j after a transmission delay δ_j. Synaptic efficacies were randomly chosen from a Gaussian distribution with mean $J_{\alpha\beta}$ and SD $\Delta J_{\alpha\beta}$ depending on the type of presynaptic (β = {E, I}) and postsynaptic (α = {E, I}) neurons. We initially set J_{EE} = 0.73 mV, J_{IE} = 0.95 mV, J_{EI} = 2.55 mV, and J_{II} = 2.55 mV, whereas $\Delta J_{\alpha\beta} = 0.25\, J_{\alpha\beta}$ for any α and β. Intramodular connectivity is c_{loc} = 80% (probability to have synaptic contact between two neurons of the same module) for any α and β, unless otherwise specified. Excitatory and inhibitory synaptic transmission delays were drawn from an exponential distribution with average 13.3 ms and 3.3 ms respectively. Each neuron receives also spikes coming from neurons outside the cortical module it belongs to, collectively modeled as a Poisson process with average spike frequency ν_{ext} chosen to have under mean-field approximation an average firing rate ν_E = 0.7 Hz and ν_I = 1.75 Hz. Synaptic efficacies

$J_{ext,k}$ were randomly chosen from a Gaussian distribution with the same moments as the local excitatory connections.

The neurons in the excitatory population were grouped in two sub-populations, 25% in a foreground population (F) displaying Up/Down slow oscillations, and the remaining 75% in a background population (B) always firing at a relatively low firing rate (Fig. 5B). Oscillatory dynamics in the foreground population was obtained by potentiating synaptic self-excitation $J_{FF} = w_+ J_{EE}$, with a potentiation level $w_+ = 1.8$. To keep fixed $\nu_F = 0.7$ Hz and $\nu_B = 0.89$ Hz, $J_{BF} = J_{FB}$ were decreased accordingly.

In the *in silico* slice, modules were spatially arranged on a 2-dimensional grid composed of H × B sites (generally H = 9, B = 20). The intermodular connectivity c_{glob} was set only between pairs of subpopulations with presynaptic excitatory neurons, modeling cortico-cortical long-range synaptic connections. When not otherwise specified $c_{glob} = 0.2$. Inter-module spike delays were sampled from an exponential distribution with 21 ms average. Connectivity decayed following a Gaussian function of the distance with standard deviation $\lambda = 0.7$ IMD (inter-modules distance). The resulting networks had a total size of N_{neu} = 63 000 neurons and N_{syn}= 20 millions of synapses. The modulation of *in silico* slice excitability (Fig. 7D) was performed by changing the spike rate ν_{Ext} of external spikes (ν_{Ext} was multiplied by a factor ranging from 0.89 to 1.00). The layered structure of the *in silico* slices (Fig. 6) was incorporated by creating an excitable strip of modules with higher connectivity, such that modules far from the strip had the lower values of connectivity: the inter- and intramodular connectivity (c_{glob} and c_{loc}, respectively) were reduced by a factor 0.8. Approaching the excitable strip connectivity this factor was gradually increased till the maximum connectivity strip (MCS) where c_{glob} and c_{loc} reach their maximum value, independently chosen for inter- and intra-modular connectivity . Numerical simulations of *in silico* slices were performed relying on an event-based approach described in (Mattia and Del Giudice 2000), spanning network times of 100 s.

To use the same analytical approach developed for *in vitro* recordings to our *in silico* slices, we estimated the instantaneous firing rates ν(t) from the simulated population of excitatory neurons in each module, and used them as MUA after adding a relatively weak white noise to emulate unspecific background fluctuations of experimental recordings.

The optimal choice for maximum c_{glob} and c_{loc} (Fig. 7) was found performing different simulation with different values of these parameters and looking for the

minimum value of the identification error between the EPS and the MCS. The identification error was estimated as the average vertical distance between the 2 strips. Simulations were evaluated on a grid of 9 × 9 points in the (max. c_{loc}, max. c_{glob}) plane, ranging from 0.8 to 1.1. For each point 4 simulations were performed. The resulting surfaces were interpolated with a thin-plate spline with smoothing parameter p = 0.95.

The dynamical features of each module were set relying on a mean-field theory. Mean-field (minimal rate) model had dynamics determined by the gain function Φ (Wilson and Cowan 1972) as follows:

$$\begin{cases} \frac{d\nu_i}{dt} = \frac{\phi_i(\vec{\nu},\vec{c}) - \nu_i}{\tau} \\ \frac{dc_i}{dt} = -\frac{c_i}{\tau_c} + g_i\nu_i \end{cases}$$

here $\vec{\nu} = \{\nu_i\}$ and $\vec{c} = \{c_i\}$, with i = {F,B,I} pointing out the excitatory foreground, excitatory background and inhibitory populations composing the single model, respectively. Since the single module includes multiple interacting neural populations, the mean-field dynamics would be described by a multi-dimensional gain function. Our gain function Φ was computed as an 'effective' gain function $\tilde{\phi}$, along the lines proposed by (Mascaro and Amit 1999). This approximation allows the reduction of the multi-dimensional mean-field problem (Amit and Brunel 1997) to a two-dimensional one corresponding to the dynamics of the firing rate (ν) and of the fatigue level (c) of the foreground population of interest (Mattia and Sanchez-Vives 2012):

$$\begin{cases} \frac{d\nu}{dt} = \frac{\tilde{\phi}(\nu,c) - \nu}{\tau} \\ \frac{dc}{dt} = -\frac{c}{\tau_c} + g\nu \end{cases}$$

For this reduced dynamics of a single module nullclines ($\dot{\nu} = 0$ and $\dot{c} = 0$) can be derived, whose intersections represent fixed points. Modules were set to have a weakly stable Down state (meaning that low-firing rate intersection was on the lower branch of the ν nullcline, rather close to the point where this branch ended, see Figure 5C). Energy landscapes near the fixed point were defined by the integral of the function $(\tilde{\phi}(\nu,c) - \nu)$, assuming for c its value in the same fixed point.

Results

We probed spontaneous Up/Down slow oscillations (SO) traveling across 12 cortical slices from 5 ferrets by measuring the extracellular raw signals simultaneously recorded from a matrix of 16 electrodes with a multiscale arrangement (Fig. 1A, see Materials & Methods). MUA of each electrode was estimated as the relative power change of high-frequency components of the raw signals in sliding windows of 5 ms (Reig et al. 2010; Sanchez-Vives et al. 2010). The large majority of the recording channels displayed a long-tailed distribution of the logarithmically scaled MUA (Fig. 1B, 80% of the 156 used electrodes) with high and low firing rate peaks corresponding to Up and Down states, respectively. For each slice, an optimal MUA threshold was selected relying on the Down peak standard deviation, to detect transition times between Up and Down states (see Materials and Methods). From these we measured the SO statistical features like state duration distributions of representative channels (Fig. 1C) and the average oscillation frequency of 0.31 ± 0.12 Hz (n = 12 slices), similarly to what previously found (Sanchez-Vives and McCormick 2000). MUA time course around state transitions (Fig. 1D) was qualitatively similar to that from conventional extracellular recordings (Reig et al. 2010; Sanchez-Vives et al. 2010), further proving the reliability of the new surface electrodes employed here in measuring MUA from cortical slices.

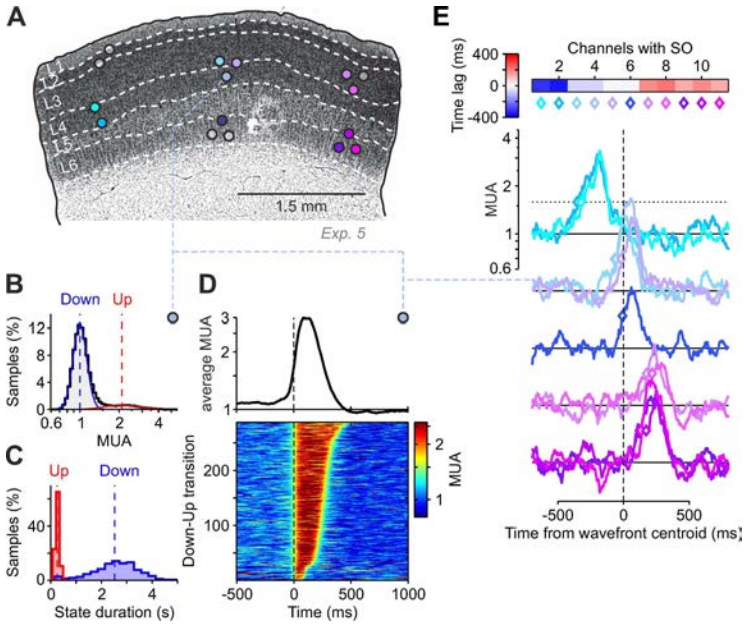

Figure 1. Multi-electrode recordings of slow Up/Down oscillations travelling across ferret cortical slices. **A**, Matrix of 16 electrodes (filled circles) superimposed to the histological slice of an example experiment. Gray circles, unused channels. **B**, Long-tailed distribution of the MUA measured from an example electrode (histogram), fitted to the sum of two Gaussian distributions (red and blue) representing the activity of the Down and Up state, respectively. Vertical dashed lines, mean of the Gaussian distributions. **C**, Histograms of the detected Up and Down state durations (red and blue, respectively). Vertical dashed lines, average durations. **D**, Rastergram of MUA (bottom) centered around the detection time of Down-to-Up transitions (0 ms). Up states are sorted by duration. Top, average MUA. **E**, Example time course of the MUA simultaneously estimated from used channels. Horizontal dotted line, MUA threshold to detect Up state onset. Diamonds, crossing time of MUA threshold. Colors are as in Panel A, and characterize different electrodes. Vertical dashed line, average time of Up state onsets composing the same wavefront. The time lags of Down-to-Up transitions from this wavefront centroid are represented as a horizontal color bar (top).

Diverse modes of wave propagation across cortical slices

Spontaneous Up state onsets at single channel level did not occur as isolated events. As shown in Fig. 1E, Up states traveled across the cortical slice (Sanchez-Vives and McCormick 2000; Sanchez-Vives et al. 2010; Wester and Contreras 2012), giving rise to waves identifiable by the set of time lags between the MUA onsets occurring across channels (Fig. 1E-top, see Materials and Methods), and the average time of such local activations was used as reference time. In each experiment we found a wide variability of the propagation patterns (Fig. 2A), the large majority of which involved at least two of the three channel vertical columns composing the multi-electrode array (MEA) (96.7 ± 3.4% of detected waves, average across all n = 12 slices). In order to uncover whether such diversity hid some spatiotemporal organization of spontaneous slow oscillations, we analyzed with a *k*-means clustering the subset of full waves, those which propagated across all the three channel columns of the MEA (Fig. 2B, see Materials and Methods for details, an average of 80 ± 19% of the detected waves per slice, n = 12). Using a fixed number of 10 wave clusters, for each we estimated the time course of average activation wavefronts across the rectangular field covered by the MEA, by performing a spatial interpolation of the averaged time lags per channel (Fig. 2C, see Materials and Methods for details).

From these wave profiles it was apparent that not only different directions in the horizontal propagation spontaneously occurred, but also that across experiments there was almost no preference in the ignition site (Fig. 2D): on average 59 ± 22 % of the

waves appeared first from the lateral columns of electrodes, while 34 ± 25 % originated close to the central column of the MEA (n = 12). Adding complexity to the phenomenon was also the evidence that more than one ignition site could contribute to the slice activation, as it is apparent from the first wave cluster in Fig. 2B (bottom) where an early Up state onset (blue matrix elements) occurred in the two most lateral electrode columns. Besides, whatever the mode of propagation was, average wavefronts displayed always a shape squeezed along the vertical axis, perpendicular to the pia of the cortical slice. This highlighted a slower velocity along the horizontal (lateral) direction with respect to the vertical (in depth) one (Fig. 2E): a difference confirmed at the population level, since the average velocities were 5.8 ± 1.8 mm/s and 8.9 ± 3.4 mm/s, respectively (n = 12), compatible with previous measures from similar experiments (Sanchez-Vives and McCormick 2000; Sanchez-Vives et al. 2010).

As all these results rely on the interpolation procedure the region of slice uncovered by the MEA, we performed an additional set of experiments including an extra electrode placed in different locations far from the MEA electrode position to check possible time shift artificially introduce by the adopted method (Fig. 2F, see Materials and Methods, and Supplementary Material). Up state onset times measured including the extra electrode was directly compared with those obtained without taking it into account displayed a high degree of correlation (Fig.2G). At population level, the average of the absolute error between real and extrapolated time lags resulted to have across recordings a rather narrow distribution (Fig.2H), with a mean error of 51.0 ± 6.5 ms (n = 24 from different slices and extra electrode positions) which corresponded to a shift of approximatively 10% the time taken by a wave to travel across the whole slice. We remark here that this is a result *per se*, as confirming the smoothness of SW propagation across cortical slices although dynamics underlying their generation is expected to be intimately nonlinear.

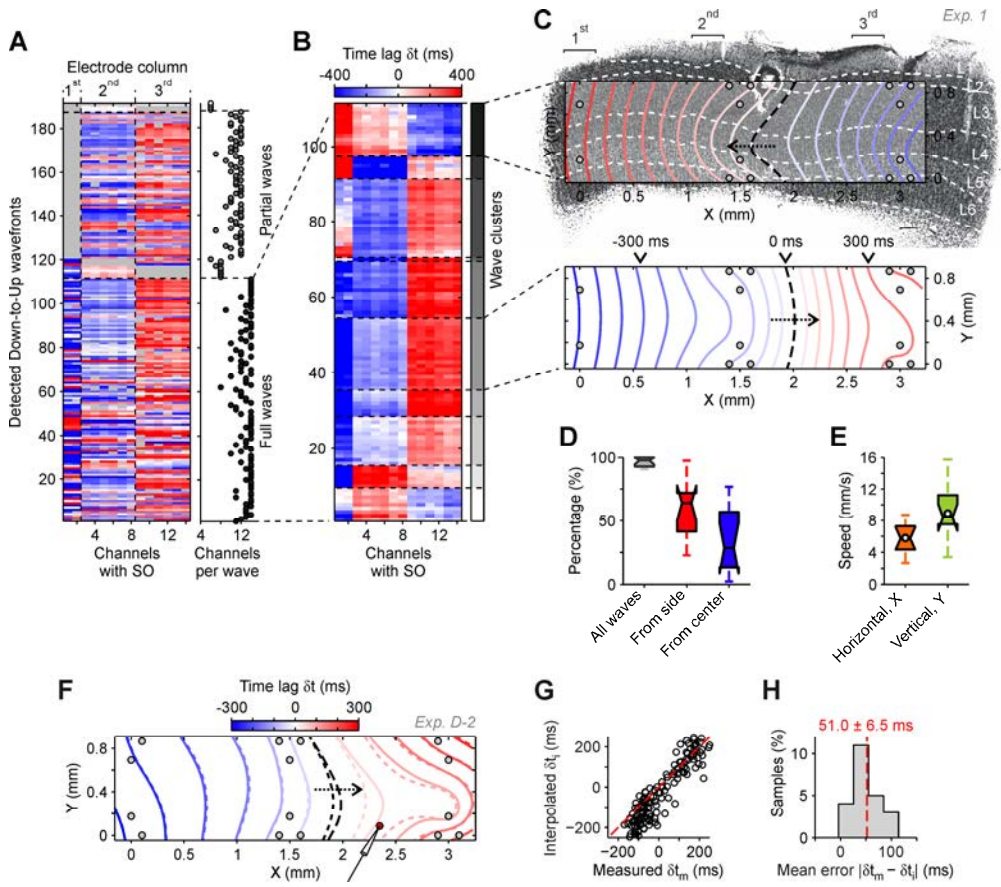

Figure 2. Variability of propagation modes of Up state onsets. **A**, Time lag matrix of detected Up state onsets from single traveling waves of an example experiment. Rows are as the top horizontal bar in Fig. 1E. Gray pixels, failed detections of Down-to-Up transition. Dashed vertical lines separate channels arranged in different vertical columns of the MEA (see panel C). Wavefronts are sorted by number of columns involved. Full and partial waves are those with 3 and 2 columns involved, respectively. Right, number of channels detecting the Up onset in each wave. **B**, Time lag matrix of full waves with failed detections of Up onsets replaced by estimates from similar wavefronts (see text). Waves are pooled in 10 groups by k-means clustering, separated by horizontal dashed lines. Gray-shading bar distinguishes different clusters. **C**, Time course of average wavefronts from two example clusters. Color code as in panel B and C. Consecutive wavefronts are separated by 50 ms. Time lags across the depicted area are interpolated from the average Up onset times across a wave cluster, relying on thin-plate splines (see text). **D**, Box plots of the fraction of full and partial waves (all = partial + full) detected across experiments (n = 12), together with the column of electrodes from where waves originated (side, from 1st and 3rd column; center, from 2nd

column). **E**, Box plots of the average absolute velocity of wave clusters across experiments (n = 12) along the horizontal (X) and vertical (Y) direction of the electrode array, parallel and perpendicular to the cortical surface, respectively. In each box plot, whiskers (dashed lines) are extreme values of the distribution, edges are the 1st and 3rd quartiles and the central mark is the median. Where shown, circles are average values of the distribution. **F,** Example of interpolated activation wavefronts obtained including or not data from an extra electrode (solid and dashed lines, respectively). Red circle represent the location of extra electrode. **G,** Scatter plot for an example slice/eleectrode position of Down-to-Up transition times measured from the extra electrode (δt_m) *versus* the interpolated ones estimated without taking account this electrode (δt_i). **H,** Histogram of the average absolute error estimated for each slice/electrode position (n = 24).

Memoryless generation of spontaneous waves

Traveling wavefronts of Up state onsets belong to the realm of phenomena occurring in noisy excitable media, known to spontaneously express spatiotemporal patterns (Cross and Hohenberg 1993; Sagués et al. 2007). Experimental evidence supports this view, as local excitation in space elicit propagating self-sustained wavefronts of *in vitro* activity (Wu et al. 1999; Wester and Contreras 2012). This phenomenon in slices displays a low degree of complexity, as spontaneous propagation modes are unidirectional (Golomb and Amitai 1997; Wu et al. 1999; Sanchez-Vives and McCormick 2000; Wester and Contreras 2012), i.e. wavefronts mainly propagate in a direction parallel to the cortical surface. Here, we characterized the dimensionality of the Up wavefronts by performing a principal component analysis (PCA) of the time lag matrices (Fig. 3A). Detected spatiotemporal patterns had low dimensionality (maximal dimensionality is 15 as the electrodes in the MEA are 16 and we set to 0 the average time lag per wave), as the first two principal components (PC) explained a large part of the time lag variance (Fig. 3B, average variance explained 82% ± 16%, n = 12). This is consistent with the previous reports on propagation patterns measured with optical imaging (Wu et al. 1999; Wester and Contreras 2012). Moreover, in the (PC_1,PC_2) plane where each full wave corresponded to a circle (Fig. 3A), two main clusters were often recognizable, representing the preferred mode of propagations, hence further decreasing the degree of complexity of spontaneous activity. This indeed corresponded to a rather stereotyped activation of the slices when belonging to the same mode (wave cluster) of propagation (see Supplementary Material). In the specific example shown in Fig. 3A, the two preferred modes corresponded to those shown in Fig. 2C for the same experiment, although other two smaller clusters were apparent in the first and third quadrant representing waves with different numbers and positions of ignition sites.

To uncover possible complexity in the time domain, we inspected the similarity degree between wavefronts occurring at different distances in time (see Materials and Methods). Visual inspection of the time course of ϕ (Fig. 3C), the angle (phase) associated in the plane (PC1,PC2) to each circle/wave in Fig. 3A, highlighted a rather irregular nature in the selection of the next wave onset between the two preferred propagation modes shown in Fig. 3A and 2C. This qualitative picture was confirmed at the population level: average autocorrelation AC_n of the time lag arrays characterizing the waves at lag *n* (see Materials and Methods), was close to 0 (Fig. 3D). Also at single slice level, wave selection was memoryless ($AC_n = 0$), with only one exception (Fig. 3E, red plot). In this experiment we found a significant positive correlation $AC_1 = 0.04$ (Wilcoxon signed-rank test, $P < 0.01$). Intriguingly, there we measured the longest Up state duration (540 ± 90 ms, more than 200 ms longer than the average duration of 310 ± 110 ms across experiments), supporting the hypothesis that this cortical slice was in a relatively more excitable state with respect to the others. The correlation between AC1 and Up state duration (Fig. 3D) confirmed that the memory degree in the next wave selection was tighlty related to the excitability of the network, which in turn is expected to be associated to longer high-firing states. From this perspective, spontaneous waves in our basal excitability levels and frequencies between 0.11 and 0.40 Hz did not take into account of past events as expected in a subexcitable state (Sagués et al. 2007). Under this condition, endogenous fluctuations of the activity in the Down state were expected to elicit in random locations the onset of different Up wavefronts explaining the memoryless renewal origin of spontaneous waves in our *in vitro* model of SO.

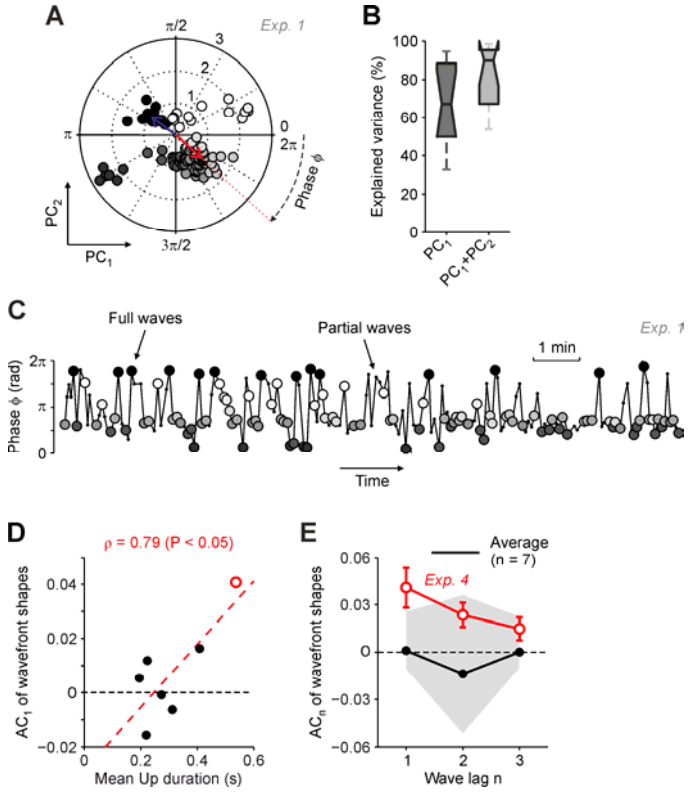

Figure 3. Past modes of propagation do not influence next Up wavefronts. **A**, First two principal components (PC_1 and PC_2) of the time lag matrix in Fig. 2B. Each circle is an Up onset wavefront (an array of time lags), whose gray shading indicates the wave cluster it belongs to (gray levels as in Fig. 2B). **B**, Box plot of variance explained by PC_1 and the first two PCs across all experiments. **C**, Time course of the phase ϕ in the (PC_1,PC_2) plane of full (filled circles) and partial (dots) waves.Gray filling and experiment as in A. **D,** Scatterplot of the autocorrelation AC_1 of the time lag arrays of consecutive waves *versus* the average duration of the Up state from a reference channel (that with the highest MUA in the Up state). Experiments included are those with a fraction of full waves greater than 80% (n = 7 out of 12). **E**, Autocorrelation AC_n of the time lag arrays of waves at lag *n*. Black line and gray shading, average and SD of AC_n across all experiments shown in D, respectively. Red line, average AC_n for a specific outlier experiment, not included in the average.

Structure has a role in shaping Up state and onset wavefronts

If SO in cortical slices arose as in a subexcitable medium, we might expect that activity reverberation did not completely overwhelm the underlying intracortical connectivity

structure. Under this hypothesis, spontaneous activity should be (at least partially) shaped by the structure and excitability distribution of the cortical network, such that wave propagation and SO in single electrodes should retain and share some of this information. To investigate such possible interplay between structure and spontaneous activity, we started looking for features of the excitation waves preserved across different modes of propagation. More specifically, following each travelling Up onset wavefront we identified an early propagation strip (EPS, see Materials and Methods), the most advanced tip of Up onset times along X direction of the MEA (Fig. 4A, dotted lines). This would likely represent the most excitable part of the slice, where neuronal pools reacted first to the synaptic input provided by nearby active cortical regions. Intriguingly, EPS extracted from excitation waves were remarkably similar in the same experiment, irrespective from their mode of propagation (Fig. 4B), further supporting the hypothesis that the underlying intracortical connectivity establishes preferred routes across the slice, modeling the shape of wavefronts independently of ignition site and direction of propagation.

A natural hypothesis is that EPS would correspond to sites of maximal excitability, which in turn led us to predict that also local SO properties would be different along the EPS. To test this hypothesis, we carried out the average Up state durations T_{Up} across the area covered by MEA, by interpolating the T_{Up} measured from the different MEA channels (Fig. 4C), similarly to what done for working out traveling wavefronts (see Materials and Methods). Another mean feature of SO related to the local excitability of neuronal assemblies was the maximum MUA during Up states (Fig.4D), computed as above by resorting to interpolation. Most excitable pools were expected to have the longest Up duration and maximum MUA, corresponding to a maximally stable Up state (Mattia and Sanchez-Vives 2012), we found them at sites composing continuous strips (green and cyan curves in Fig. 4C and D, respectively), which in turn displayed a remarkable overlap with the EPS estimated from wave propagation (Fig. 4E). This overlaps between excitable strips estimated from different features of slow wave activity in slice was apparent across all experiments, as the vertical distance between EPS (Y_{EPS}) and position of maximum MUA ($Y_{max.\ MUA}$ in Fig. 4F) and maximum T_{Up} ($Y_{max.\ Tup}$ in Fig. 4G) were not significantly different from 0 (average distances were 47 ± 140 μm and 10 ± 90 μm, respectively; Wilcoxon sign-rank test, $P > 0.05$; see Materials and Methods for details). As also EPS and the strips of maximum MUA and T_{Up} relied on the interpolation method introduced by commenting Fig. 2, we investigated the introduced error by measuring the differences when the extra electrode was or was not taken into account (see Materials and Methods, and

Supplementary Material). When computed as an average across all waves, EPSs estimated with and without the extra electrode (solid and dashed line in Fig.4H, respectively) widely overlapped. The average vertical distance had a narrow distribution across slices and extra electrode position (Fig. 4I), with a relatively small mean EPS location error of 39.5 ± 7.3 μm, approximatively about the 5% of the MEA vertical extension. Similar results were obtained for the strips of maximum MUA and T_{Up} (see Supplementary Material). Finally, it is important to remark that all population analyses were computed at the horizontal center of the electrode columns where misalignment between interpolation and real measures was the smallest.

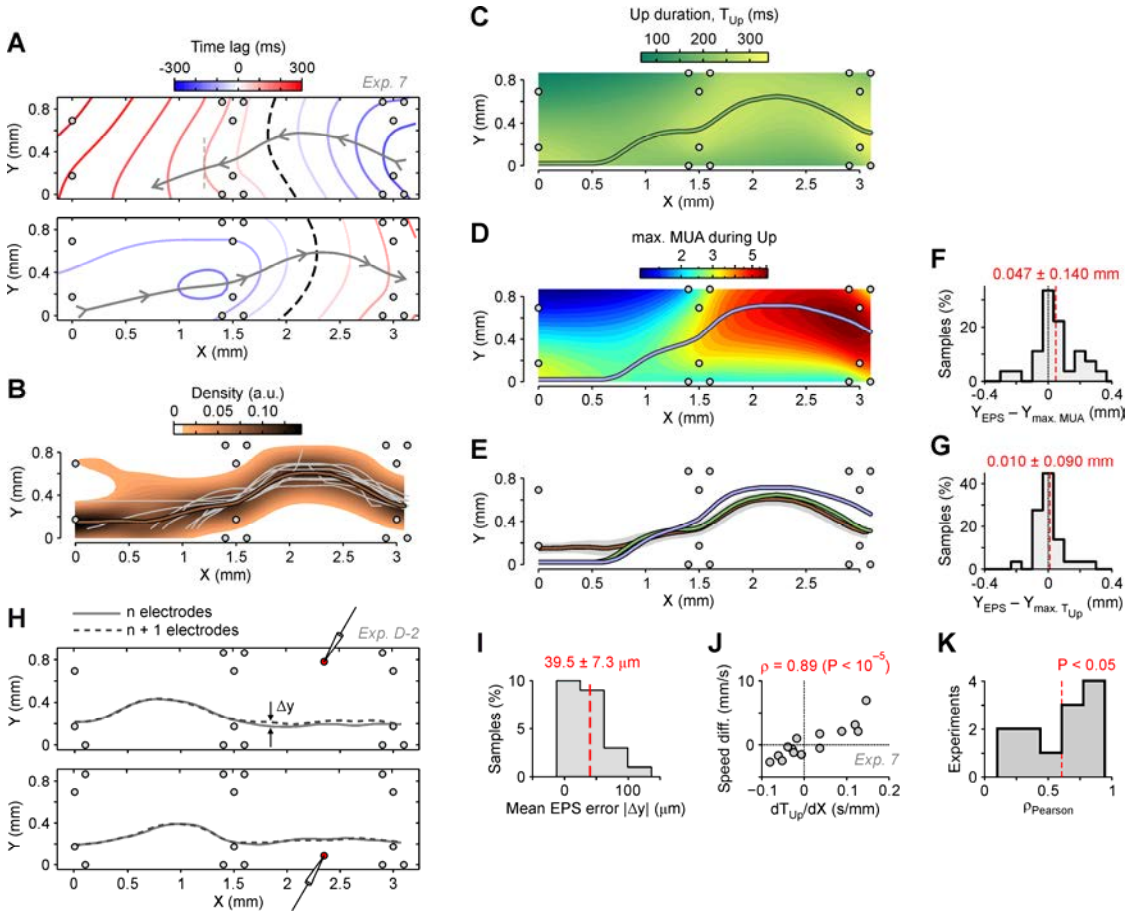

Figure 4. Global Up wavefront properties match local dynamical features of SO. **A**, Two example Up wavefronts propagating in opposite directions as in Fig. 2C, from another example experiment. Gray curves with arrows, early propagation strip (EPS). **B,** Density of EPS from all detected waves. Brown thick line, weighted average of EPS density along X direction. Gray lines, EPSs of each cluster of traveling waves computed as in Fig. 2. **C,** Average Up state duration (T_{Up}) interpolated across the slice

area covered by the matrix of electrodes (circles). Green thick line, maximum Up duration found at different X. **D**, Average maximum MUA during Up state interpolated as in panel C. Cyan thick line, maximum MUA found at different X. **E,** Superimposed weighted average of EPS, maximum Up state duration and MUA from panels B-D, respectively. **F-G,** Histograms of the vertical distance across all experiments (n = 12) between EPSs and line of maximal Up duration (F) or MUA (G). **H,** EPS estimated with and without the extra electrode (dashed and solid lines, respectively). Two example different positions of the extra electrode are showed (top and bottom panels, see Supplementary Material for details). **I,** Distributions of the average vertical error in interpolating the EPS across slice and extra electrode locations (n=24). **J,** Correlation between speed difference and dT_{Up}/dX, the change per unit length of Up state duration along the EPS, in the same example experiment of panels A-E. Speed difference is between median velocities of waves propagating in opposite directions (see Materials and Methods for details). **K,** Histogram of the Pearson correlation ρ as in panel H for all experiments (n = 12). To the right of the red dashed line, correlations ρ are significant ($P < 0.05$).

What shown here highlights a non-monotonic degree of excitability across the cortical depth (vertical Y direction of MEAs), displaying a maximum at intermediate layers where local populations emitted spikes at higher firing rates during Up state, compatibly with the leading role of Layer 5 in the generation of SO found in previous *in vitro* studies (Sanchez-Vives and McCormick 2000; Wester and Contreras 2012). On the other hand, a heterogeneous degree of excitability was also apparent along the direction parallel to the cortical surface (horizontal X direction of MEAs), as shown in Fig. 4C and D, as both maximum MUA and T_{Up} increased from left to right.

A gradient of maximum MUA and Up duration (T_{Up}) along the excitable strip (solid lines in Fig. 4C and D), would intuitively produce an acceleration of the waves traveling in the same direction, while a deceleration should be measured for those waves propagating towards less excitable region of the slice. These could imply different speed profiles depending on the propagation mode, as acceleration in one way can be higher than the absolute value of the deceleration in the opposite direction. Indeed, accelerating waves would find a more excitable tissue, while in the other way wavefront would be pushed ahead by less excitable cortical assemblies. According to this, a correlation is expected between the gradient of the excitability (the change of T_{Up} per unit horizontal length dT_{Up}/dX, see Materials and Methods) and the speed difference between leftward and rightward propagating wave (Fig. 4J). This correlation, related to the interplay between the spatiotemporal patterns and horizontal circuits of the cortex, was found in the majority of the experiments (Fig. 4K, 7 out of 12 experiments had significant correlation, $P < 0.05$ with a Pearson correlation $\rho > 0.5$), further supporting the evidence of an intimate relationship between spontaneous activity and underlying cortical organization.

Weakly stable Down states behind slow oscillations

The analysis described so far shows that cortical slices spontaneously express waves generated by nonlinear self-excitation; wave propagation exhibits a rich repertoire of spatiotemporal patterns, which we have shown to be related to the structural organization of the slice. Taken together, these observations suggest that the cortical network behaves as a nonlinear excitable system, that is balanced such that it avoids collapsing into stereotyped excited collective states (e.g. epileptic) while keeping sensitivity to the connectivity spatial structure.

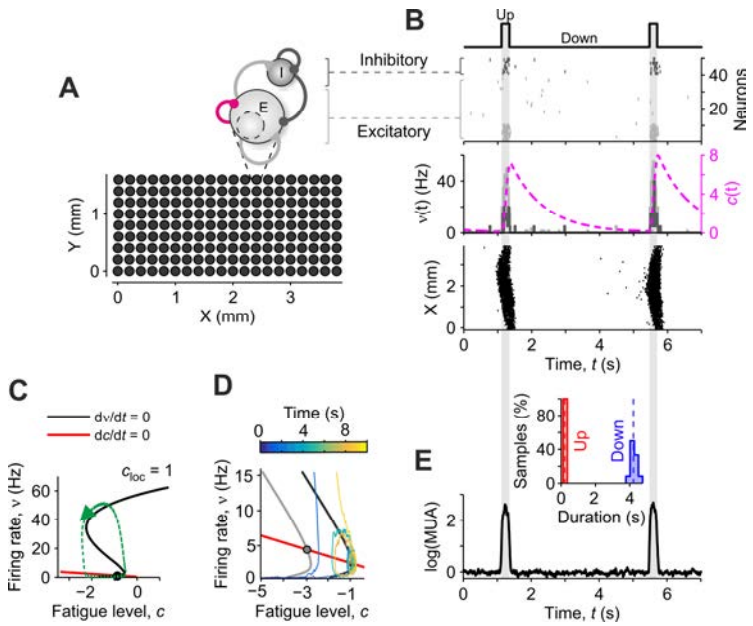

Figure 5. Slow-wave activity in a spiking neuronal network model of cortical slice. **A**, Simulated networks are organized as a lattice of interacting modules (small black circles). Top, each module is composed of two pools of excitatory (E) and inhibitory (I) LIF neurons. Excitatory neurons receive an additional state-dependent self-inhibition (purple link) modeling spike frequency adaptation (SFA). **B**, Example slow oscillation in a simulated module. Top raster plot displays a subset of emitted spikes. Recurrent connectivity between excitatory neurons is shaped in order to have only a subset of them firing during Up states (depicted in panel A-top as a dashed circle in the excitatory pool). Center, firing rates $\nu(t)$ of different pools, and fatigue level $c(t)$ proportional to self-inhibition inducing SFA. Bottom, raster of spikes emitted by neurons from different excitatory modules along X axis of the modeled slice. **C,** Nullclines (curves) and fixed-points (circles) of single module dynamics in the (ν,c) plane, under mean-field approximation. Green curve, example trajectory of the

module in the (ν,c) plane, with initial condition on the right of the ν-nullcline. **D,** Mean-field nullclines for the same module in (C) receiving two different inputs obtained increasing external rate of spikes by 7% (dark gray) and 20% (light gray). Superimposed are example trajectories for these two conditions, colored to encode time (see top color bar). **E,** MUA in logarithmic scale estimated from the firing rate ν(t) of the example cortical module in (B). Inset, histogram of Up and Down state durations detected from the modeled MUA with the same analytical tools used for *in vitro* recordings, as in Fig. 1C.

We therefore undertook to understand, in a theoretical model, the determinants of such interplay between excitability and sensitivity to structural features. For this purpose, we set up a large-scale model of cortical slice as a network of modules arranged uniformly on a lattice, each of them exciting nearby modules which intensity decreasing with distance (Fig. 5A, Materials and Methods). Modules were composed of 350 leaky integrate-and-fire (LIF) excitatory (80%) and inhibitory (20%) neurons each. SO occurred as the interplay between recurrent synaptic excitation and a history-dependent self-inhibition (Fig. 5B), analogously to previous works (Bazhenov et al. 2002; Compte et al. 2003; Holcman and Tsodyks 2006; Mattia and Sanchez-Vives 2012). During Down state activity fluctuations can drive the module through recurrent excitation towards a high-firing Up state, self-sustained in time by local synaptic reverberation involving a subset of both excitatory and inhibitory neurons (Fig. 5B-top). Each excitatory neuron possesses an activity-dependent inhibitory current modelling spike frequency adaptation (SFA) due to the influx of a hyperpolarizing potassium current proportional to a fatigue level $c(t)$, which increases each time a spike is emitted (Koch 1999). During periods of high firing rate $\nu(t)$, fatigue $c(t)$ accumulates (Fig. 5B-middle, purple line), eventually crossing a threshold level which destabilizes the Up state and determines the Up-to-Down transition and the beginning of the recovery phase during the Down state. Excitatory intermodular connectivity promotes a fast chain reaction following a local Down-to-Up transition, recruiting nearby inactive modules after recovery from previous active states, eventually generating global SO as in Figure 5B-bottom. A synthetic MUA from the firing rate of each module is computed by adding a Gaussian white noise unavoidably affecting electrophysiological recordings (Fig. 5E, Materials and Methods). This allow to analyze and compare experiments and simulations with the same tools, as those to work out state duration distribution (Fig. 5E, inset).

In order to quantitatively reproduce the statistics of experimental SO, two minimal requirements had to be met. Firstly, Down state should be weakly stable, such that Down-to-Up transitions can occur with non negligible probability due only to

fluctuations of local activity $\nu(t)$; alternatively, Down-to-Up transitions can be primed by the additional input due to the activation of nearby modules. Secondly, modules must be excitable, such that small supra-threshold inputs could elicit the onset of an Up state.

Cortical modules with these features can be designed by relying on mean-field theory, where the module nonlinear dynamics can be fully depicted in the phase plane (ν,c) (see Materials and Methods). Figure 5C shows the nullclines (loci of zero time derivative) for ν (black) and c (red), for a parameters choice meeting the above requirements: the (stable) Down state is the only intersection between the nullclines (i.e. the only point attractor of the dynamics), and the green curve describes an example trajectory followed by the system for an initial condition to the right of the ν nullcline. As the Down state is very close to the knee of the ν nullcline, its stability is weak and noise can promote an escape from this state. If endogenous fluctuations are taken into account, while the system approaches the Down fixed point, it can fluctuate for long time around it (Fig. 5D, colored curve), until a large enough fluctuation makes it jump towards the upper branch of the ν nullcline (the Up state). If, at parity of other parameters, the synaptic input from other modules is increased, the ν nullcline shifts to the left (Fig. 5D gray curve), and an almost deterministic Down-to-Up transition is elicited. The two illustrated scenarios address the requirements above, and would represent i) the modules which due to fluctuations prime the activation wave onset (black nullcline) and ii) those ones which receiving input from nearby active modules contribute to the wave propagation (gray nullcline).

Heterogeneous excitability shapes spatiotemporal activity patterns

As the next step, the cortical slice model was employed to investigate the mentioned interplay between local excitability and structural features suited to reproduce the spatiotemporal properties of propagating waves found in our experiments (Figs. 2, 3 and 4). For this purpose, we differentially modulated the excitability level of the cortical modules in the slice model, with the most excitable modules in a strip (dark inverted U strip in Fig. 6A, Materials and Methods). Following (Mattia and Sanchez-Vives 2012), the excitability of the cortical modules was regulated by changing the local connectivity c_{loc} (probability to establish a synaptic contact between two excitatory neurons in the same module) and/or the external input from other modules, here dependent on the global connectivity c_{glob} (probability of a connection with an excitatory neuron from nearby modules). Increasing c_{loc} raised the firing rate of the Up states and

strengthened its stability (upper branch of the ν nullcline became higher and wider, gray to black curves in Fig. 6B). At the same time, Down state stability was weakened as the corresponding attracting energy valley became shallower (in Fig. 6C-top, gray to black curves).

In this cortical slice model, synchronized SO across the lattice of modules collectively emerged as an activation wave (Fig. 6D). The spatiotemporal pattern started with the Up state onset in a neuronal assembly close to the most excitable strip (Fig. 6D, white dashed line), where modules with maximum c_{loc} were located (MCS, maximum connectivity strip). From there, the activation wave propagated horizontally following the maximally excitable modules. Maximum MUA (dark red) occurred along the MCS as the tip of the Up onset wavefront, consistently with what shown in Fig. 4. More specifically, we characterized activation waves resorting to the cluster analysis used for the experiments, recognizing also in simulation different modes of propagation (Fig. 6E). Similar to what found *in vitro*, the *in silico* cortical slice displayed a remarkable overlap between the MCS (dashed line), the EPS estimated from wave propagation and the strip where maximum MUA and T_{Up} were measured from SO of the single modules (Fig. 6F). This overlap did not depend on the particular shape of the MCS, as we tested by performing simulations with different strip shapes (not shown).

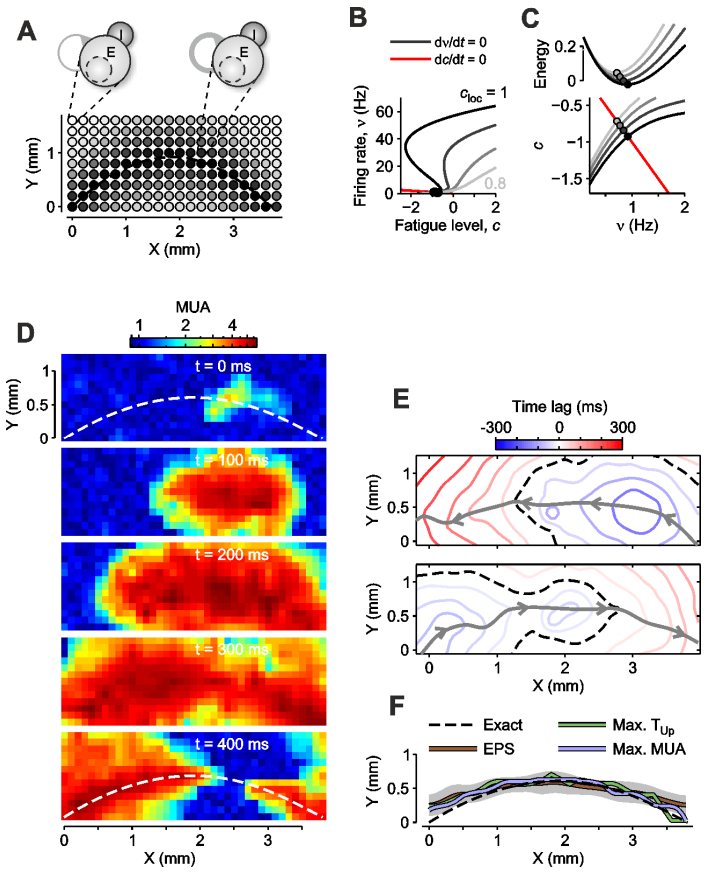

Figure 6. Spiking cortical model with non-homogeneous structure. **A**, Simulated networks have the same multi-modular arrangement as in Figure 5A, with the only difference that modules have a different degree of intra- (local) and intermodular (global) connectivity (see sketch above). Darkest circles (thickest synaptic link) are those with the highest connectivity. **B** Nullclines (curves) and fixed-points (circles) of single module dynamics in the (ν,c) plane, varying the connectivity level under mean-field approximation. Gray levels code for connectivity, same as in (A). **C,** Energy landscapes (top) around the fixed-points varying connectivity as in (C). Bottom, a (rotated) zoom of the (ν,c) plane in (C). **D**, Snapshots at different times of the propagation of an Up wavefront across the cortical slice model. White dashed line is the maximum connectivity strip (MCS) corresponding to the region of the most excitable modules as in (A). Color coded is the MUA from simulations. **E,** Two examples of Up wavefronts propagating in opposite directions from the same simulation, as in Fig. 4A. **F,** Comparison between estimated EPS (brown), and strips of maximum Up state duration (green) and MUA (cyan), together with the exact position of the MCS set in the modeled slice (black dashed line).

An optimal balance between short- and long-range connectivity

The capability to produce travelling waves of Up state onsets by assigning a pivotal role to a subset of maximally excitable neuronal assemblies, which in turn shape these spatiotemporal patterns does not offend intuition, and may appear as a rather straightforward expectation. With this in mind, we explored the sensitivity of the wave features expressed by the *in silico* slice to the choice of several key parameters of the network.

The uniqueness of the dynamical regime needed to reproduce the collected *in vitro* experimental evidence described in Fig. 5, emerged also by testing the model network under the modulation of another critical parameter known to modulate the nonlinear dynamics of networks expressing SO (Mattia and Sanchez-Vives 2012): the intensity of an external excitatory input I_{ext} modeling the incoming background activity produced outside the modeled neuronal field (see Materials and Methods). By increasing I_{ext}, SO in single modules displayed Up states with longer durations (Fig. 7D), which in turn positively correlated (Pearson correlation $\rho = 0.56$, $P < 0.001$) with the autocorrelation AC_1 between the time lag arrays representing wave propagation, the same as the one measured in experiments (Fig. 3): the larger the excitability, the longer the Up state and the higher the correlation between the mode of propagation of successive waves (wave lag 1). Similarly to what found in experiments, on average no memory was retained about the way waves propagated previously in time (Fig. 7E, black line at $AC_n \cong 0$). A positive autocorrelation of the time lag arrays occurred only for those simulations with large enough I_{ext} (red circles in Fig. 7D) representing the most excitable model networks. In this case average correlation (Fig. 7E, red line) was significantly different from 0 (Wilcoxon rank sum test, $P < 0.01$), in good agreement with what found *in vitro* (Fig. 3D).

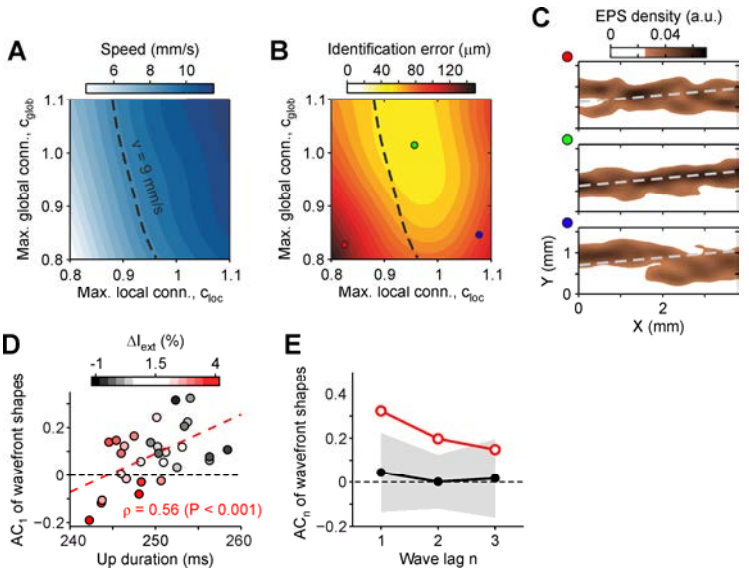

Figure 7. *In silico* optimal balance between global and local connectivity. **A**, Speed of traveling wavefronts in cortical slice models varying local (c_{loc}) and global (c_{glob}) connectivity in the MCS. Connectivity of modules outside the MCS are adjusted accordingly (see text for details). Dashed line, set of network parameters yielding to a constant speed of waves of 9 mm/s compatible with experiments. **B,** Identification error of MCS from EPS for the same parameter set as in (A). **C,** Comparison between EPS and MCS for three different example slice models corresponding to the filled circles in (B). **D,** Average Up state duration *versus* autocorrelation AC_1 between time lag arrays of consecutive Up wavefronts, computed as in Fig. 3. Each circle is a simulated network with a different external excitatory input I_{ext} to each excitatory neuron, modulating the module excitability. Filling color codes for the changes ΔI_{ext} of the reference external input I_{ext} in the network of panels (A-B) with $c_{\mathrm{loc}} = c_{\mathrm{glob}} = 1$. **E,** Autocorrelation AC_{n} of the time lag arrays at different wave lags, as in Fig. 3D. Black line and gray shading depicts the average and SD over all simulations. Red line, AC_{n} an outlier slice model with the highest I_{ext}.

Middle cortical layers lead wave propagation and SO

Our matching observations from experiments and in silico slices strongly suggest that the cortical slice structure determines the features of *in vitro* spontaneous SO and their propagation across the tissue. A natural question follows up: does the most excitable region of cortical slices inferred from their spontaneous activity correspond to a specific anatomical structure? Previous *in vitro* studies highlighted a leading role of L5 in the generation of SO (Sanchez-Vives and McCormick 2000). Neurons in this layer were the

first to activate with respect to the others located at different depths in the same cortical column. However, the columnar interactions between supragranular and infragranular layers (L2/3 and L5) were found to underlie the activity propagation of *in vitro* SO (Wester and Contreras 2012). Here, we addressed the question by matching the laminar organization characterized from histology and the excitable regions inferred from the spontaneous activity of the slices (Fig. 8A). More specifically, in the cortical slices where histology was available (n = 9 out of 12 experiments), we computed the area covered by the distribution of EPS estimated from recorded waves in different layers (see Materials and Methods for details). As a result, we found a major overlap between L4 and L5 and EPS distribution (Fig. 8B), and hence with the slice region where maximum MUA and Up duration were also found. Fractions of EPS in L2/3 and L6 was significantly lower than those in L4 and L5 (Wilcoxon sign-rank test, $P < 0.001$). Although EPS area overlapping with L4 was on average lower than the one on L5, the difference was not significant such that the functional identification of the most excitable region of cortical slice highlighted a shared role between these two layers.

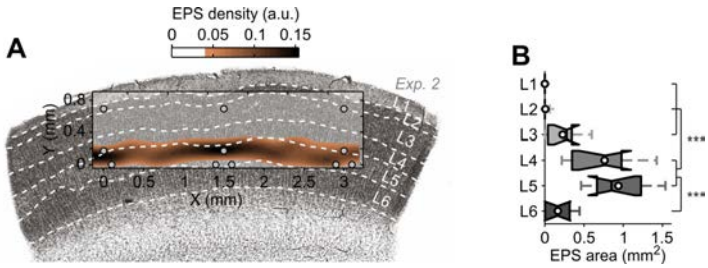

Figure 8. L4 and L5 overlap with the excitable cortical region predicted from spontaneous activity propagation of *in vitro* SO. **A**, EPS density and area covered by the MEA superimposed to the image of the corresponding cortical slice stained after electrophysiological recordings. Dashed lines, boundaries between layers. EPS density below 0.04 is not shown. **B,** Box plot of the area covered by EPS density higher than 0.04 in each layer of the cortical slices for which histological characterization was performed (n = 9 out of 12).

Discussion

Our cross-cutting study of the spontaneous alternation between Up and Down states propagating across cortical slices provides a novel perspective on the dynamical origin of such a multiscale phenomenon. We relayed on a dedicated experimental setup in which an array of multiple electrodes was arranged in small electrode clusters, thereby providing a multi-resolution probe to investigate at the same time both local and global network dynamics. By this means, we reproducibly found a rich repertoire of propagation modes all sharing three distinctive features. Firstly, activation waves systematically propagated parallel to the cortical surface, in agreement with previous works (Wu et al. 1999; Sanchez-Vives and McCormick 2000; Wester and Contreras 2012), although a wide distribution of speeds and ignition sites was found within each single experiment. Almost no local activity bumps were observed. Wavefronts of Up state onset were mildly curved, corresponding to a measured vertical speed, along columnar orientation, twice the horizontal one. Secondly, irrespective of their variability, wavefronts revealed *loci* across the slices which reproducibly led SO propagation, composing a longitudinal smooth strip. Upon checking against anatomical reconstruction, this strip largely overlapped L4/L5, compatibly with the evidence that the most excitable cell assemblies reside in L5 both *in vitro* (Sanchez-Vives and McCormick 2000; Wester and Contreras 2012; Krause et al. 2014) and *in vivo* (Sakata and Harris 2009; Chauvette et al. 2010; Amigó et al. 2015). Finally, wave onset was an almost memoryless process, i.e. no correlations were found between propagation modes of successive waves. Such composite evidence traced a narrow path for the theoretical model we developed to understand its determinants: the prominent excitable strip pointed towards a distribution of local excitability; the variability of wave modes and their lack of memory hinted at an important role of noise.

In fact, we found that a multi-modular large-scale *in silico* model of the slice, capable to reproduce all these features, must primarily incorporate a distribution of excitability in the form of heterogeneous synaptic self-excitation of the single modules. But we also found that local self-coupling must be optimally balanced with the mutual excitation between modules. These conditions ensured that our *in silico* slice acted as a structured sub-excitable medium in which each module displayed a marginally stable Down state from which, thanks to maximal sensitivity to endogenous finite-size noise and inter-modular input, relaxation oscillations could be generated. As a result, the most excitable strip overlapped the sites with maximal duration of the Up states, and with maximal firing during Up states, as confirmed by our experiments and further

highlighting the pivotal role of L4/L5 in leading SW activity. All findings support the hypothesis that this default mode spontaneously expressed by the cerebral cortex (Sanchez-Vives and Mattia 2014) is due to a privileged configuration of the network allowing both dynamical richness and sensitivity to underlying structure.

Comparisons with previous studies

Horizontal intracortical connections play an important role in determining the speed of activity propagation (Wadman and Gutnick 1993; Golomb and Amitai 1997; Sanchez-Vives and McCormick 2000; Wester and Contreras 2012), together with the excitability level modulated for instance by the balance between excitation and inhibition (Sanchez-Vives et al. 2010), as also described in theoretical models of SW activity (Bazhenov et al. 2002; Compte et al. 2003). In the specific framework of *in vitro* spontaneous SO, the horizontal speed of SWs we measured (5.5 ± 1.5 mm/s) well matches those from previous works which range from 7.2 mm/s (Sanchez-Vives et al. 2010) to 10.9 mm/s (Sanchez-Vives and McCormick 2000) in ferret cortical slices (same preparation adopted here), up to the 20 mm/s measured in rat brain slices (Wester and Contreras 2012). Note that, the high speed reported in the latter work may be due not only to the different animals, but also to the use of voltage-sensitive dyes (VSD) imaging, known to probe subthreshold membrane potential rather than the suprathreshold MUA we recorded. An even higher horizontal velocity of 30 mm/s was previously measured with VSD imaging in rat neocortical slices in low (0.1 mM) magnesium (Wu et al. 1999). SO frequency under these conditions was 7 – 10 Hz, significantly higher than that measured in our experiments (0.31 ± 0.12 Hz). If greater speed is attributed to greater excitability, the above theoretical argument would also imply: i) less variable wave propagation modes (due to reduced sensitivity to the underlying structure) and ii) more correlated successive propagation modes. Indeed, (Wu et al. 1999) also observed that waves usually propagated in the same direction. These predictions which might be ideally tested in experiments in which slice excitability is directly manipulated as in (Reig et al. 2010; Sanchez-Vives et al. 2010; Sancristóbal et al. 2016).

Relations with *in vivo* slow-waves

In anesthetized rodents SW activity is well documented, and reported to be similar to SWs during deep sleep (Alkire et al. 2008; Cirelli and Tononi 2008; Siegel 2008), thus raising a question as to their possibly similar dynamic origin to SWs *in vitro*. A first difference is that *in vivo* Down-to-Up wavefronts propagate faster, with a speed

tangential to the cortical surface which ranges from 25 to 40 mm/s (Fucke et al. 2011; Ruiz-Mejias et al. 2011; Stroh et al. 2013; Sheroziya and Timofeev 2014). This is irrespective on the adopted probe which in these works varied from intracellular and extracellular recordings to two-photon calcium imaging. What we measured in our slices experiments as the vertical speed of the Up state onset, *in vivo* was observed by directly probing cortical columns during SO (Sakata and Harris 2009; Chauvette et al. 2010). Columnar activation *in vivo* was more asymmetric as deep layers (L5 and L6) activated simultaneously, and the activity spreads towards superficial layers (L2/3) with a speed of about 30 mm/s, as a depth of 700 μm was covered in about 25 ms (Sakata and Harris 2009). Such quantitative differences in asymmetry and speeds may be plausibly related to the known lack of long-range cortico-cortical connections *in vitro* (Stepanyants et al. 2009; Schnepel et al. 2015), which is expected to be more pronounced along the direction tangential the cortical surface. This would explain why in the cortical slice the vertical speed is twice the horizontal one, while they are almost the same as in the intact brain. We also remark that the mentioned differences may affect the optimal balance between local excitability and inter-modular connectivity which we have shown here to be a major determinant of the kinematics of slow waves.

Limitations of this study

Here, activation and silencing of wavefronts were reconstructed relying on an interpolation procedure between the sparse electrodes of the MEA, and clustering together similar waves in order to improve the signal-to-noise ratio of the estimated state transition time lags. Under the assumption of reasonably smooth wavefronts, this method allowed to recover information about the wavefronts in slice regions where no electrodes were available. A failure of this assumption might imply a wrong identification of the depth of the strip leading wave propagation. To test its range of applicability, we performed simulations of the *in silico* slice with different shapes and slopes of the most excitable strip (not shown). As expected, the error in estimating the strip location from the measured EPS increased for steeper slopes. Nevertheless, its magnitude was always remarkably small. Of course, having denser arrays of electrodes would allow to relax the above assumption, without changing the analytic approach here introduced, which is independent from the MEA size. The flexibility of the approach would allow to apply it also to other experimental frameworks like the study of *in vivo* quasi-planar waves.

Another possible limitation of this study is that we did not sort single units (SU) from the MUA. Yet, we do not expect any qualitative change in the characterization of

in vitro SWs from relying on SU activity instead of MUA. Indeed, using rather different methodologies with different spatial and temporal resolutions ranging from intracellular and extracellular recordings, to calcium and VSD imaging, the observed propagating modes shared in all cases similar features both *in vivo* (Fucke et al. 2011; Ruiz-Mejias et al. 2011; Stroh et al. 2013; Sheroziya and Timofeev 2014) and *in vitro* (Wu et al. 1999; Sanchez-Vives and McCormick 2000; Sanchez-Vives et al. 2010; Wester and Contreras 2012).

Functional and dysfunctional implications

An appealing result of the modeling study was the recognition that for the model to match the experimental it was critical a proper balance between local and mutual modules excitation. This together with the need of a weakly stable Down state, establishes a "sweet spot" of the network parameters where structure is influential but at the same time allows for a wide variety of propagation modes. As travelling waves have been proposed to contribute both to process and transfer information across peripheral areas of the cerebral cortex (Rubino et al. 2006; Ferezou et al. 2007; Sato et al. 2012; Muller et al. 2014), from a computational standpoint an intriguing implication arises. It has been proposed that optimal sensitivity to structure can be a smart way to implement "self-organized instability" (Solé et al. 2002). Whenever the environment changes and new stimuli are sensed, the cortical network moves to a different working point, likely no longer optimal. To bring the system back to an optimal working regime a mechanism is needed allowing to recover the proper weak stability of the Down state. A simple unspecific modulation of the network excitability would serve this purpose. As a result, the variability of stimulus-evoked waves would not be purely random, but rather sensitive to the network structure (Rabinovich et al. 2008). If such a self-organization mechanism would exist, the emergence of a default mode made of propagating SO should appear as a direct consequence of it.

On the other hand, pushing the cortical tissue outside this sweet spot likely distorts the spontaneous activity yielding the network to display pathological dynamics, which can persist if optimality is not recovered. For instance, a wrong balance between excitation and inhibition is now known to influence the speed of the SWs travelling across the frontal cortex of Down's syndrome models (Ruiz-Mejias et al. 2016). An underexpressed synaptic inhibition seems to underlie the break of long-range coherence of SW activity in mouse models of the Alzheimer's disease (Busche et al. 2015). In these cases our analytical approach, combined with properly tuned *in silico* models, have a potential to help elucidate which combination of local excitability and

inter-modular synaptic coupling underlie SW activity changes, unraveling the mechanistic roots of pathological dynamics.

Acknowledgements

This work was in part supported by CORTICONIC (EC FP7 grant 600806), WaveScalES (EC FET Flagship HBP SGA1 720270), BFU2014-52467-R and FLAGERA-PCIN-2015-162-C02-01, MINECO (Spain).

References

Alkire MT, Hudetz AG, Tononi G. 2008. Consciousness and anesthesia. Science (80-). 322:876–880.

Amigó JM, Monetti R, Tort-Colet N, Sanchez-Vives M V. 2015. Layer 5 leads information flow during slow oscillations according to information directionality indicators. J Comput Neurosci. 38.

Amit DJ, Brunel N. 1997. Model of global spontaneous activity and local structured activity during delay periods in the cerebral cortex. Cereb Cortex. 7:237–252.

Bazhenov M, Timofeev I, Steriade M, Sejnowski TJ. 2002. Model of thalamocortical slow-wave sleep oscillations and transitions to activated States. J Neurosci. 22:8691–8704.

Benucci A, Frazor R a, Carandini M. 2007. Standing waves and traveling waves distinguish two circuits in visual cortex. Neuron. 55:103–117.

Bringuier V, Chavane F, Glaeser L, Frégnac Y. 1999. Horizontal propagation of visual activity in the synaptic integration field of area 17 neurons. Science (80-). 283:695–699.

Busche MA, Kekuš M, Adelsberger H, Noda T, Förstl H, Nelken I, Konnerth A. 2015. Rescue of long-range circuit dysfunction in Alzheimer's disease models. Nat Neurosci. 18:1623–1630.

Chauvette S, Volgushev M, Timofeev I. 2010. Origin of active states in local neocortical networks during slow sleep oscillation. Cereb Cortex. 20:2660–2674.

Cirelli C, Tononi G. 2008. Is sleep essential? PLoS Biol. 6:1605–1611.

Compte A, Sanchez-Vives M V, McCormick DA, Wang X-J. 2003. Cellular and network mechanisms of slow oscillatory activity (<1 Hz) and wave propagations in a cortical network model. J Neurophysiol. 89:2707–2725.

Cross MC, Hohenberg PC. 1993. Pattern formation outside of equilibrium. Rev Mod Phys. 65:851–1112.

Ermentrout GB, Kleinfeld D. 2001. Traveling electrical waves in cortex: insights from phase dynamics and speculation on a computational role. Neuron. 29:33–44.

Ferezou I, Haiss F, Gentet LJ, Aronoff R, Weber B, Petersen CCH. 2007. Spatiotemporal Dynamics of Cortical Sensorimotor Integration in Behaving Mice. Neuron. 56:907–923.

Fucke T, Suchanek D, Nawrot MP, Seamari Y, Heck DH, Aertsen A, Boucsein C. 2011. Stereotypical spatiotemporal activity patterns during slow-wave activity in the neocortex. J Neurophysiol. 106:3035–3044.

Golomb D, Amitai Y. 1997. Propagating neuronal discharges in neocortical slices: computational and experimental study. J Neurophysiol. 78:1199–1211.

Han F, Caporale N, Dan Y. 2008. Reverberation of recent visual experience in spontaneous cortical waves. Neuron. 60:321–327.

Holcman D, Tsodyks M. 2006. The emergence of Up and Down states in cortical networks. PLoS Comput Biol. 2:e23.

Illa X, Rebollo B, Gabriel G, Sánchez-Vives M V, Villa R. 2015. A SU-8-based flexible microprobe for close and distal recordings from the cortical network. In: SPIE Microtechnologies. International Society for Optics and Photonics. p. 951803.

Jancke D, Chavane F, Naaman S, Grinvald A. 2004. Imaging cortical correlates of illusion in early visual cortex. Nature. 428:423–426.

Koch C. 1999. Biophysics of Computation: Information Processing in Single Neurons. New York: Oxford University Press.

Krause BM, Raz A, Uhlrich DJ, Smith PH, Banks MI. 2014. Spiking in auditory cortex following thalamic stimulation is dominated by cortical network activity. Front Syst Neurosci. 8:1–24.

Lee S-H, Blake R, Heeger DJ. 2007. Hierarchy of cortical responses underlying binocular rivalry. Nat Neurosci. 10:1048–1054.

Luczak A, Barthó P, Harris KD. 2009. Spontaneous events outline the realm of possible sensory responses in neocortical populations. Neuron. 62:413–425.

Mascaro M, Amit DJ. 1999. Effective neural response function for collective population states. Network. 10:351–373.

Massimini M, Huber R, Ferrarelli F, Hill SL, Tononi G. 2004. The sleep slow oscillation as a traveling wave. J Neurosci. 24:6862–6870.

Mattia M, Del Giudice P. 2000. Efficient event-driven simulation of large networks of spiking neurons and dynamical synapses. Neural Comput. 12:2305–2329.

Mattia M, Pani P, Mirabella G, Costa S, Del Giudice P, Ferraina S. 2013. Heterogeneous attractor cell assemblies for motor planning in premotor cortex. J Neurosci. 33:11155–11168.

Mattia M, Sanchez-Vives M V. 2012. Exploring the spectrum of dynamical regimes and timescales in spontaneous cortical activity. Cogn Neurodyn. 6:239–250.

Mohajerani MH, McVea D a, Fingas M, Murphy TH. 2010. Mirrored bilateral slow-wave cortical activity within local circuits revealed by fast bihemispheric voltage-sensitive dye imaging in anesthetized and awake mice. J Neurosci. 30:3745–3751.

Muller L, Reynaud A, Chavane F, Destexhe A. 2014. The stimulus-evoked population response in visual cortex of awake monkey is a propagating wave. Nat Commun. 5:3675.

Rabinovich MI, Huerta R, Laurent G. 2008. Transient dynamics for neural processing. Science (80-). 321:48–50.

Reig R, Mattia M, Compte A, Belmonte C, Sanchez-Vives M V. 2010. Temperature modulation of slow and fast cortical rhythms. J Neurophysiol. 103:1253–1261.

Rubino D, Robbins KA, Hatsopoulos NG. 2006. Propagating waves mediate information transfer in the motor cortex. Nat Neurosci. 9:1549–1557.

Ruiz-Mejias M, Ciria-Suarez L, Mattia M, Sanchez-Vives M V. 2011. Slow and fast rhythms generated in the cerebral cortex of the anesthetized mouse. J Neurophysiol. 106:2910–2921.

Ruiz-Mejias M, Martinez de Lagran M, Mattia M, Castano-Prat P, Perez-Mendez L, Ciria-Suarez L, Gener T, Sancristobal B, García-Ojalvo J, Gruart A, Delgado-García JM, Sanchez-Vives M V, Dierssen M. 2016. Overexpression of Dyrk1A, a Down Syndrome Candidate, Decreases Excitability and Impairs Gamma Oscillations in the Prefrontal Cortex. J Neurosci. 36:3648–3659.

Sagués F, Sancho JM, García-Ojalvo J. 2007. Spatiotemporal order out of noise. Rev Mod Phys. 79:829–882.

Sakata S, Harris KD. 2009. Laminar structure of spontaneous and sensory-evoked population activity in auditory cortex. Neuron. 64:404–418.

Sanchez-Vives M V, Mattia M. 2014. Slow wave activity as the default mode of the cerebral cortex. Arch Ital Biol. 152:147–155.

Sanchez-Vives M V, Mattia M, Compte A, Perez-Zabalza M, Winograd M, Descalzo VF, Reig R. 2010. Inhibitory modulation of cortical up states. J Neurophysiol. 104:1314–1324.

Sanchez-Vives M V, McCormick DA. 2000. Cellular and network mechanisms of rhythmic recurrent activity in neocortex. Nat Neurosci. 3:1027–1034.

Sancristóbal B, Rebollo B, Boada P, Sanchez-Vives M V., Garcia-Ojalvo J. 2016. Collective stochastic coherence in recurrent neuronal networks. Nat Phys. 12:1–8.

Sato TK, Nauhaus I, Carandini M. 2012. Traveling waves in visual cortex. Neuron. 75:218–229.

Schnepel P, Kumar A, Zohar M, Aertsen A, Boucsein C. 2015. Physiology and Impact of Horizontal Connections in Rat Neocortex. Cereb Cortex. 25:3818–3835.

Sheroziya M, Timofeev I. 2014. Global Intracellular Slow-Wave Dynamics of the Thalamocortical System. J Neurosci. 34:8875–8893.

Siegel JM. 2008. Do all animals sleep? Trends Neurosci. 31:208–213.

Solé R V, Alonso D, McKane AJ. 2002. Self-organized instability in complex ecosystems. Philos Trans R Soc London Ser B. 357:667–671.

Stepanyants A, Martinez LM, Ferecskó AS, Kisvárday ZF, Ferecsko AS. 2009. The fractions of short- and long-range connections in the visual cortex. Proc Natl Acad Sci USA. 106:3555–3560.

Stroh A, Adelsberger H, Groh A, Rühlmann C, Fischer S, Schierloh A, Deisseroth K, Konnerth A. 2013. Making Waves: Initiation and Propagation of Corticothalamic Ca2+ Waves In Vivo. Neuron. 77:1136–1150.

Wadman WJ, Gutnick MJ. 1993. Non-uniform propagation of epileptiform discharge in brain slices of rat neocortex. Neuroscience. 52:255–262.

Wester JC, Contreras D. 2012. Columnar interactions determine horizontal propagation of recurrent network activity in neocortex. J Neurosci. 32:5454–5471.

Wilson HR, Cowan JD. 1972. Excitatory and inhibitory interactions in localized populations of model neurons. Biophys J. 12:1–24.

Wu J-Y, Guan L, Tsau Y. 1999. Propagating activation during oscillations and evoked responses in neocortical slices. J Neurosci. 19:5005–5015.

Xu W, Huang X, Takagaki K, Wu J. 2007. Compression and reflection of visually evoked cortical waves. Neuron. 55:119–129.

Title: Ohmic quasistatic models fail to describe the electromagnetic propagation of slow oscillations and epileptiform activity in cortical tissue

Abstract

Macroscopic models ofthe propagation of electromagnetic fields in neural tissue (from electroencephalography to local field potentials) assume the validity of the quasistatic approximation (QSA) of the Maxwell equations. Upon this approximation, which is extensively applied in both clinical (e.g. deep brain stimulation, electrical neuroimaging) and experimental neuroscience (e.g. current source density computation via Laplacian of Potentials), electromagnetic fields travel nearly instantaneously from the sources to the sensors. Yet, recent estimates suggest that the propagation speed of epileptiform activity within the hippocampal tissue is too low (~0.1m/s) to justify quasistatic assumptions. We tested the assumptions of the QSA by studying the electromagnetic propagation of slow wave oscillations (SWO) and epileptiform activity in neocortical slices after isolating synaptic from electromagnetic transmission. Contrary to the damped, undistorted, instantaneous propagation of SWOs (<1Hz) and epileptiform activity predicted by QSA over short distances, we observed substantial deformations and delays compatible with dispersion arising from ionic diffusion and/or polarization. Our results suggest that accurate macroscopic models of propagation of electromagnetic fields in neural tissue must consider the dispersive properties that account for the laminar and columnar microstructure of the cortex.

Introduction

Macroscopic models of the propagation of electromagnetic fields (local field potential, LFP; electroencephalography, EEG; magnetoencephalography, MEG) in neural tissue assume the validity of the quasistatic approximation (QSA) of the Maxwell equations (1). In these models, the gray matter is typically considered as a homogeneous conductor described by a constant conductivity and therefore, dispersion, i.e. frequency-dependent dielectric parameters (conductivity and permittivity), which is inherent to good conductors (2), is ignored. With dispersion, the propagation speed of electromagnetic phenomena varies with frequency; therefore, delays and distortion characterize signal propagation.

In contrast, the most salient property of quasistatic in ohmic (resistive) conductors is the absence of delays assuming that electric and magnetic fields travel instantaneously from their sources to the sensors. Consequently, under the QSA, electromagnetic fields are memoryless as they neither depend on their past values nor those of their sources. In this view, electromagnetic signals propagating in neural tissue can only afford damping (attenuation of the wave's amplitude) but not delays or distortion.The QSA is not only relevant for computational macroscopic models but also for clinical and experimental neuroscience. Indeed, the design (3) and understanding of the effects of deep brain stimulation devices (4) or the models underlying non-invasive electrical neuroimaging (5) all rely on the QSA. Electrophysiological data analysis estimates the Current Source Density by calculating the Laplacian of the measured potentials (6). This approach might be invalid if the QSA is violated (7).

Several reasons cast doubts on the validity of such a simplified model to estimate the behavior of electromagnetic fields in highly heterogeneous ionic conductors such as neural tissue. First, the neural tissue preferentially filters some frequencies more than others

(8)and LFP/EEG/MEG signals show a 1/f spectrum that is compatible with the existence of dispersion (9, 10). Second, ionic conductors are lossy materials in which absorption is important. As a consequence of causality (2), lossy materials are necessarily dispersive. Third, nearly all dielectric spectroscopy studies of cortical tissue report substantially high dielectric permittivity values at low frequencies, which isincompatible with the purely resistive (ohmic) model, as well as important low-frequency dispersion (11, 12). Noticeably, the lack of dispersion reported by Logothetis (13) in vivo seems to contradict the universal low-frequency dispersion that was experimentally observed and modeled by Jonscher (14), Ngai (15) and Dissado and Hill (16) in non-biological materials with ionic conductivity. Fourth, epileptiform activity in the hippocampus has been recently observed to propagate by electric field effects at a speed of 0.1 m/s (17), which is far too slow to justify the instantaneous propagation of the effects predicted by the QSA in the absence of dispersion. Fifth, a recent experimental study from Gomes et al. (18) indicates the necessity of revisiting the assumption of the extracellular space as a purely ohmic medium.

Obtaining reliable estimates of the dielectric parameters in neural tissue via "broadband dielectric spectroscopy" (19) would readily inform about the accuracy of QSA models to describe electrophysiological phenomena. Unfortunately, the accuracy of dielectric spectroscopy is substantially compromised in the low-frequency range of interest to study neural rhythms. This compromise is a consequence of electrode polarization effects appearing at the electrode-electrolyte interface that subsist (20) even if a four-electrode system is used for estimation (13). Removal of polarization effects typically requires theoretical or phenomenological assumptions on the specific behavior of the polarization impedance (21, 22). Polarization effects, therefore, compromise the accuracy of dielectric estimates below 100Hz (21) rendering them unavailable below 10Hz (21, 22).

An alternative approach is to evaluate whether substantial delays and distortion accompany the propagation of the signals that we are interested in modeling, for instance,those obtained in neural tissue using standard LFP recordings in vitro. Rather than relying on current injection, which often enhances parasitic effects, one can inspect the propagation of spontaneously occurring neural activity such as slow wave oscillations (SWO), which are neural signals consistingof interspersed Up (with active neuronal firing) and Down (silent) states, and which are similar to those observed during slow-wave sleep and deep anesthesia(27). Alternatively, one can pharmacologically evoke natural signals such as epileptiform activity or SWO. Also, it is possible to considerably reduce distortions of artifactual origin by carefully avoiding filtering and by choosing the recording electrodes and the amplifiers, making sure that electrode impedance remains negligible relative to amplifier input impedance over the frequency range of interest (23). Ifdespite these precautions,delays, and distortions still accompany the electromagnetic propagation of natural signals, then cortical tissue should be treated as the lossy dispersive dielectric that is predicted by the causality principle (24), which would be in agreement with the behavior observed for ionic conductors (25).

We investigated the validity of the QSA by dissociating the electromagnetic from the synaptic contributions to the propagation of slow wave oscillations and epileptiform activity in cortical tissue. For this, we used ferret neocortical slices that spontaneously generate SWO (26). SWO and epileptiform activity provide an excellent testbed since they belong to the lowest frequency range of the electromagnetic spectrum where the QSA should be most accurate.To test whether the electromagnetic propagation of SWO and epileptiform activity can be explained by the QSA, we completely sectioned the cortical slice into two pieces by making an entire cut perpendicular to the white matter but allowing contact between the tissue on both sides. Three aspects of this electromagnetically propagated neural activity were characterized: the attenuation with

distance of the signal (damping), the propagation speed, and the possible existence of signal distortion.

Materials and Methods

General approach: Our main goal was to characterize how fields associated with physiologically relevant activity (SWOs or epileptiform discharges) propagate in the cortical tissue. We wanted to evaluate if distortion and delays accompany propagation independently of synaptic transmission. Indeed, if the neural tissue can be assumed as an ideal conductor operating under the QSA, then signal delays and distortions should be absent during extrasynaptic (field-mediated) propagation to source-free regions. On the contrary, substantial delays and distortion would provide indications of the need to account for dispersion to model signal propagation. Dispersion, arising from either ionic diffusion or polarization, would require replacing Poisson by Helmholtz equation (8) in current models and considering frequency varying dielectric parameters as discussed next.

1. Theory

The Maxwell equations allow describing the propagation of electromagnetic fields in biological tissue. For simplicity, we express here all equations in the frequency domain. All fields are complex valued functions that depend on space (r) and frequency (w). Temporal derivatives $\frac{\partial}{\partial \mathrm{t}}$ in the time domain are replaced by the multiplicative factor iw where $\mathrm{i} = \sqrt{-1}$and w is measured in rad/s. With this convention, the Maxwell equations read:

$$\nabla \mathrm{x} \mathrm{E}(\mathrm{r},\mathrm{w}) = -\mathrm{iw}\mathrm{B}(\mathrm{r},\mathrm{w}) \qquad (1)$$

$$\nabla \mathrm{x} \mathrm{H}(\mathrm{r},\mathrm{w}) = \mathrm{iw}\mathrm{D}(\mathrm{r},\mathrm{w}) + \mathrm{J}_{\mathrm{f}}(\mathrm{r},\mathrm{w}) \qquad (2)$$

$$\nabla . \mathrm{D}(\mathrm{r},\mathrm{w}) = \rho_{\mathrm{f}}(\mathrm{r},\mathrm{w}) \qquad (3)$$

$$\nabla . \mathrm{B}(\mathrm{r},\mathrm{w}) = 0 \qquad (4)$$

where E is the electric field vector [V/m], H the magnetic field vector [A/m], D the electric flux density (displacement) vector [As/m^2], B the magnetic flux density (displacement) vector [Tesla], $J_f$the current density vector [A/m^2], and ρ the scalar charge density [As/m^2]. The subscript f is used to indicate free charges and currents, i.e., to distinguish (ionic) charges that can move freely within the medium from bound charges. The current density J_f consists of two parts:$J_f = J_c + J_p$, with $J_p$denoting a primary or impressed source, independent of the field and delivering energy to carriers (ions), and $J_c$denoting the conduction current.

The constitutive relations linking the flux densities (D and B) to the fields (E and H) for linear isotropic materials read as:

$$D(r,w) = \epsilon_0\big(1 + x_e(r,w)\big)E(r,w) = \epsilon(r,w)E(r,w) \qquad (5)$$

$$B(r,w) = \mu_0[H(r,w) + x_m(r,w)H(r,w)] = \mu(r,w)H(r,w) \qquad (6)$$

$$J_c(r,w) = \sigma(r,w)E(r,w) \qquad (7)$$

Wherex_e and x_m are the electric and magnetic susceptibilities and $\underline{\epsilon}$, μ and σ are the permittivity, permeability, and conductivity, respectively. Since neural tissue is non-magnetic, its permeability can be considered identical to empty space permeability, i.e., $\mu = \mu_0$.

To relate the Maxwell equations to electrophysiological measurements, it is more convenient: 1) to express the electric and magnetic fields in terms of the auxiliary potentials φ and A respectively, where A is the vector potential, and φ the scalar potential of interest to electrophysiology; and 2) to rely on a formalism in which electric and magnetic fields are uncoupled via the wave equation in the frequency domain, i.e., the Helmholtz equation. In the most general case of anisotropic and heterogeneous

materials,the Helmholtz equation can be writtenin terms of a complex permittivity ϵ_c defined as: $\epsilon_c = \epsilon_0\epsilon_r - j\frac{\sigma}{w} = \epsilon - j\frac{\sigma}{w}$, with ϵ_r being the relative permittivity (dielectric constant) $(F.m^{-1})$ of the material at frequency w. With this definition, the Helmholtz equation reads (28):

$$\nabla.[\epsilon_c(r,w)\nabla\varphi(r,w)] + jw\nabla.[\epsilon_c(r,w)A(r,w)] = \frac{\nabla.J_p(r,w)}{jw} \qquad (8)$$

Eq. 8 is not easily solvable for arbitrary materials. In practice, it is common to approximate materials as if their dielectric parameters ϵ and σ are piecewise constants in spacewhile keeping their frequency dependency.Electric properties, which fluctuate over space in neural tissue, are averaged over microscopically large-volume elements and summarized in the form of effective dielectric properties. These engineered variables, which summarize fields due to neuronal boundaries and structural details, are determined from dielectric spectroscopy as in Gabriel's database (21). In this case, the problem is reduced to the following non-homogeneous Helmholtz equation:

$$\nabla^2\varphi(r,w) + \frac{w^2}{v_p^2}\varphi(r,w) = \frac{\nabla.J_p(r,w)}{jw\epsilon_c(r,w)} \qquad (9)$$

The term $\frac{w^2}{v_p^2} = -\gamma^2$, with $\gamma = \alpha + j\beta$, is the so-called propagation constant, a frequency-dependent complex valued function expressed in terms of the attenuation $(\alpha, Np/m)$ and the phase $(\beta, rad/m)$ constants given by (29):

$$\alpha = \frac{w\sqrt{\mu}}{\sqrt{2}}\left[\sqrt{1+\left(\frac{\sigma}{w\epsilon}\right)^2} - 1\right]^{\frac{1}{2}} \text{ and } \beta = \frac{w\sqrt{\mu\epsilon}}{\sqrt{2}}\left[\sqrt{1+\left(\frac{\sigma}{w\epsilon}\right)^2} + 1\right]^{\frac{1}{2}} \qquad (10)$$

The attenuation constant defines the rate at which the different frequency components of the signal attenuate during propagation. The phase constant defines the rate at which the phase changes as the signal propagates.

In neural tissue, it is standard to compute the fields using the quasistatic approximation (1), which practically amounts to:

1) Quasistatic: Neglects the second term on the left side of Eq. 9, which amounts to assume that the propagation constant $\gamma = 0$.

2) Ohmic or resistive: Neglects capacitive effects, i.e., neglects the term $jw\epsilon$ *on the denominator on the right-hand term in Eq. 9.*

These assumptions lead to the Poisson equation with a frequency-independent real-valued conductivity, which is solved in EEG/LFP modeling using appropriate boundary conditions (but see (30)). Importantly, despite the generalized use of the term *quasistatic* in the bioelectricity literature to refer to the Plonsey and Heppner approximation, it must be noticed that the Poisson equation in ohmic conductors describes static fields rather than electro-quasistatic phenomena. Nevertheless, for consistency with the literature in the domain, we will continue to refer to this approximation as the quasistatic approximation (QSA).

Assuming $\gamma = 0 \text{ in Eq. } 9$ is applicable for the low frequencies of interest to electrophysiology if, and only if, the phase velocity v_p, were sufficiently large so that the second term becomes negligible. A common confusion is to imagine that the propagation speed of electromagnetic phenomena is always very high, approaching the speed of light. Indeed, this is true in a lossless dielectric medium, where the conductivity is assumed zero and the propagation constant equals the phase constant (see e.g., (31)). In this case of

lossless dielectrics, the phase velocity is defined by $v_p = \frac{1}{\sqrt{\mu\epsilon}}$, coinciding with the speed of light in the material. If the permittivity does not vary with frequency, the group and phase velocity coincide and dispersion is absent.

Things are different in good conductors, in particular in the low-frequency range where $\frac{\sigma}{w\epsilon} \gg 1$. Substitution in Eq. 9 of the attenuation and phase constants defined by Eq. 10 in good conductors leads to:

$$\alpha \approx \sqrt{\frac{w\mu\sigma}{2}} \text{and } \beta \approx \sqrt{\frac{w\mu\sigma}{2}} \qquad (11)$$

In good conductors, the real and imaginary parts of the propagation constant are approximately equal both depending on frequency. Therefore, even if the dielectric properties (ϵ and σ)per se are relatively constant over a broad band of frequencies, a good conductor is always dispersive.

In effect, the phase velocity v_p, i.e., the speed at which each frequency component of the original source travels, is given by:

$$v_p = \frac{w}{\beta} \approx \frac{w}{\alpha} \approx \frac{1}{\sqrt{\mu\epsilon}} \sqrt{\frac{2w\epsilon}{\sigma}} = \sqrt{\frac{2w}{\mu_0\sigma}} = w\sqrt{\frac{2}{w\mu_0\sigma}} = w\delta \left[\frac{m}{s}\right] \qquad (12)$$

where δ is the skin depth, i.e., a measure of the depth at which the electric field and the current density fall to 1/e of their value at the interface between the membrane (source) and the extracellular space. For example, in copper at 10 Hz, the skin depth is just 21mm, and the phase velocity is only 21 mm/s. With these estimates, it is hard to neglect the second term on the left-hand side in Eq. 9 as to justify the so-called QSA in neuroscience which, as previously mentioned, corresponds to static. Since in the most general case dielectric parameters can vary with frequency, we will use, from now on, the term

electromagnetic (*EM)* propagation to refer to the dynamic aspects of the propagation of fields in tissue that can be described by solutions to the Helmholtz (8) or approximated by static solutions to the Poisson equations.

Under quasistatic, electrophysiological signals propagate unaltered in shape and with infinite speed. The situation is completely different outside quasistatic. The lower frequencies will travel further in a good conductor albeit at lower speeds than the high frequencies. Thus, good conductors will always exhibit frequency-dependent propagation speeds and will, therefore, show distortion and filtering even if the dielectric parameters themselves do not vary with frequency.

1.1 Physical causality forces dispersion in good conductors

The causality principle describes the temporal relationship between cause and effect stating that no effect can precede its cause. In electrodynamics, causality expresses that the response of a material to an electromagnetic perturbation must be zero before the onset of the perturbation. As a property specific to the material, causality cannot be directly inferred from Maxwell equations (1-4). Developing causality-compliant electromagnetic models implies that the dielectric parameters (conductivity and permittivity) are linked by the dispersion or Kramers-Kronig (KK) relations. Dispersion relations relate the imaginary part of ε, which characterizes the absorptive (damping) properties of the medium in conductors (24), to the real part of ε, which characterizes its dispersive (frequency-shifting) properties.

Intuitively, dispersion relations are analogous to linear filters. Causal filters, which suppress some frequency components without leak of the signal into the past, lead to distortions and delays. Likewise, in conductors, because of causality, electromagnetic absorption of certain frequencies must be accompanied by phase shifts of other

frequencies. As phase shifts in the frequency domain imply delays in the time domain, some of the components of the signal should propagate at lower speeds than others (dispersion) to comply with causality. This results in distortions in the shape of the temporal wave of the propagated signal. The filtering analogy, nicely illustrated in Toll (24), reflects that in practice it is impossible to envision a physical system that is at the same time strongly absorptive, causal and dispersionless (2).

Clearly, modeling dispersion effects is impossible under the QSA as the equations resulting from neglecting propagation effects ($\gamma^2 = 0$) are the static equations of Poisson/Laplace, which assume instantaneous and distortionless propagation. Consequently, if signal propagation in neural tissue is accompanied by distortion and delays, this would require a description based on the Helmholtz equation (Eq. 9).

2. Experimental procedures

Slice preparation: In vitro experiments were carried out on 400-µm-thick slices from the ferret occipital cortex, including primary visual cortical areas. Adult ferrets (5–8 months old, male) were anesthetized with sodium pentobarbital (40 mg/kg) and decapitated. The entire forebrain was rapidly removed and placed in oxygenated cold (4-10^{o}C) bathing medium. Ferrets were cared forin accordance with the European Union guidelines on the protection of vertebrates used for experimentation (Strasbourg 3/18/1986), and the experiments were approved by the local ethical committee. Details on the preparation can be found in (32). The bath temperature was constantly monitored and maintained at 34-36°C.

Complete vertical cut of the cortical slice (Fig. 1): To separate the synaptic from the electromagnetic (EM) propagation, we performed a complete cut of the slice perpendicular to cortical layers using a scalpel blade. The cut was done while the slices were in the interface chamber. The recordings were carried out in the following solution

{Sanchez-Vives, 2000 #34}(in mM): NaCl, 126; Na_2HPO_4, 1; $NaHCO_3$, 26; KCl, 4; $MgSO_4$, 1; $CaCl_2$, 1; dextrose, 10; and aerated with 95% O_2, 5%CO_2 to a final pH of 7.4 . The two sides of the cut remained in close contact as could be seen through the microscope (Fig. 1C), where no discontinuity was seen. This was allowed by maintaining the cut slices in an interface chamber, where the slices remained mechanically stable and firmly adhered at the bottom of the chamber consisting of filter paper.

Then, the recording grid was placed on top of the sectioned slice, and simultaneous recordings were obtained from both sides by the same array for every experiment. Once the experiment was finished, we removed the two sections of the slice from the filter paper, confirming that they were indeed completely separated, which was the case in all the experiments (n= 22, 15 control and glutamate-induced waves and seven epileptiform activity induced by blocking $GABA_A$-mediated inhibition with bicuculline).

Extracellular recordings (Fig. 1): Extracellular local field potential (LFP) recordings were obtainedusingarrays containing 16 gold electrodes plated with platinum black disposed on a recording grid (Fig. 1A). A microprobe including an array of holes was designed and fabricated using SU-8 negative photoresist. The holes were used to allow oxygenation of the slices, to provide mechanical stability and to allow other electrodes or pipettes to reach the slice. In each of the recording points, we had 2-3 closely spaced electrodes(separated by 200 μm) positioned such that they would record from supra and

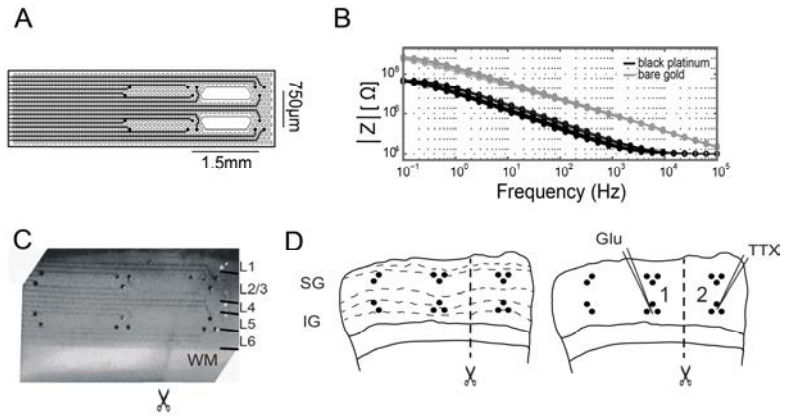

Figure 1. **Extracellular recordings from a** 16**-electrode array positioned in a visual cortex slice**. **A.** Customized microprobe consisting of 16electrodes (black dotsorganized into six groups of 2 to 3 closely placed electrodes (black dots; 50µm diameter, separated by 200µm). Holes in between the electrodes allow the contact between the slice and the oxygenated and humidified environment. **B.** Impedance characterization of the array. Electrode-electrolyte impedance modulus shift measured in 0.9% NaCl before (gray line, bare gold sensors) and after (black line) modification of the sensors using platinum black. **C.** Flexible microprobe array positioned in a sectioned cortical slice, with eight electrodes aimed at supragranular layers (SG) and eight electrodes at infragranular layers (IG). **D.** Schematic of the recording configuration from a sectioned cortical slice. (Left) Ten electrodes recording from the left part of the slices and six from the right part.Dashed lines display layer limits. (Right) The scheme represents a situation where glutamate was locally applied to one part of the slice while applying TTX at the other part. Glu, glutamate; IG, infragranular layer; L1-L6, layers 1 through 6; SG, supragranular layer; TTX, tetrodotoxin; WM,white matter; Z, impedance.

infragranular layers (750 µm apart) and from what should correspond to 3 different cortical columns (1.5 mm apart) (Fig.1A and 1C). In the array, ten electrodes recorded from one side of the cut and six electrodes from the other side (Fig. 1C and 1D). The electrodes were 50 µm in diameter, which resulted in high impedance values (at 1 kHz, |Z|~10 MΩ). We further decreased the impedance by electrochemically coating the electrode with a veryrough layer of black platinum. With this coating, a 2-fold decrease in the impedance values was achieved (Fig. 1B), resulting in electrode impedance values being two orders of magnitude below the amplifiers' input impedance over the whole frequency range. Neural activity was referenced to an electrode placed at the bottom of

the chamber in contact with the artificial cerebrospinal fluid (ACSF). To exclude the possibility of phase delays or distortion induced by differences in electrode coating, electrode impedances and phases were tested with known signals before the recordings for each recording grid (Fig. 1B). Unfiltered signals were acquired with Multichannel System amplifier (> 10^{12} Ω paralleled by ten pF input impedance) and digitized at 10 KHz with a Power1401 interface and Spike2 software (CED, Cambridge, UK). No filters were added during the recording stage to avoid signal distortion.

Drug application: Glutamate (0.5mM) and tetrodotoxin (TTX)(30μM) were delivered using a brief pulse of nitrogen to a drug-containing micropipette (volumes of 10–20 pl, (26)), as indicated in the text (Fig. 1D). Glutamate was released into different positions within the slice every 4, 6 or 8 seconds, while TTX was applied to one specific location. The average response triggered by the release of glutamate was then computed at each position to cancel out spontaneous activity that was not synchronized to this event. Bicuculline methiodide (bicuculline) ($GABA_A$ blocker; 2.4-3 μM) was bath applied to evoke epileptiform activity.

3. Signal analysis and statistics

The analysis was based on the raw, unfiltered signals and was done using custom-built Matlab functions (Matlab R2007b, The Mathworks, Natick, MA). The smoothing seen in the figures is due to the process of averaging over stimulus repetitions.

Slow wave onset: The onset of the spontaneous SWO was determined following a previously describedapproach (33). The onset was considered at the moment where the first derivative of the low-pass (<100 Hz) filtered extracellular potential crossed the zero line. The end was considered at the moment where the derivative of the signal crossed the zero line after reaching its maximum. This is the only analysis where off-line filtering was necessary, and filtering was based on zero-phase forward and reverse digital

filteringto minimize signal distortion or time delays. The slow wave onset determined from this approach was then used to align the unfiltered responses.

Statistics: Both parametric and their equivalent non-parametric tests were used in all statistical comparisons. All samples were tested for normality using the Lilliefors test (34). When the test provided clear evidence for rejecting the null hypothesis of normality ($p<0.01$) we relied on the nonparametric version of the two-samples t-test, the Mann–Whitney U. Paired comparisons were preceded by ANOVA and its nonparametric version (Friedman test) to assess overall differences between groups. Values are presented as mean ± S.D.

Assessing the presence of response: Mean responses created by time-averaging the unfiltered data in individual electrodes were tested for significant changes from baseline (2s) values usingtwo samples, two-tailed t-test. Electrodes that showed a significant ($p<0.01$) increase/decrease in signal power, defined as the square of the raw voltage values with respect to the baseline distribution, were consideredto have a significant mean response. To identify periods where mean responses significantly deviated from baseline, we applied a sample-by-sample t-test comparing the distribution of values after glutamate stimulation with the distribution of all values during the baseline interval. The periods where the t-test was significant ($p=0.001$) were defined as periods of significant responses. The same test was used to compare the responses before and after TTX, and the responses after TTX were additionally compared to the baseline period.

Peak fitting to characterize damping, distortion, and delays: Statistics on the mean slice responses evoked by glutamate were estimated from the position, height (amplitude) and width (duration) of peaks by using an iterative least-square curve fitting. Curve fitting was performed using the Peak Fitter toolbox (version 5), available from the Matlab user-contributed section. For each electrode, we iteratively fitted the 2.5 s signal following

glutamate release with an increasing number of peaks, varying from two to five, until the fitting error reached a minimum. Electrodes with poor fitting, indicated by fitting errors above 10%, were discarded from the statistical analyses.

To evaluate distortion, we introduced a measure of peak compression (PC) defined as the difference between the width estimated at the electrode with the largest response in the stimulated triode (reference, Wr) and the width at all other electrodes (We), and all divided by the reference width, i.e., PC=(Wr-We)/Wr. Note that positive values of the peak compression denote peaks that are narrowed with respect to the reference, while negative values denote peak widening. Delays were measured from the difference in latency between the first peak detected at the reference electrode and the latency of the first peak at all the other electrodes. The propagation speed of SWOs was computed by dividing the inter-electrode distance by the estimated delay. To investigate the impact of the laminated neural geometry on electromagneticpropagation, we computed population statisticson the fitted peak parameters after splitting the data into four groups according to the layer onto where glutamate was released (supra/infragranular) and the layer from which the EM waves were recorded (supra/infragranular).

Results

We recorded from a total of 15 cortical slices that displayed spontaneous slow oscillatory activity, each oscillation cycle consisting on an Up (active) and a Down (silent) state (as in 26). All of the slices were cut vertically (across layers) and the activity was recorded from both sides of the cut, whichremained in physical contact.

Electromagnetic propagation of slow oscillations

Cutting the slice resulted in two independent networks on each side, each of them with its slow oscillatory pattern of spontaneous oscillations (SWOs). We consistently observed that

the spontaneous SWOs that originated and propagated within one side of the slice could be recorded across the cut albeit with strongly reduced amplitudes (Fig. 2A). Mean Up states on one side of the cut, once aligned with the onset of spontaneous Up states on the other side, were significantly different from baseline in 86% of the cases ($p<0.01$, t-test; n= 13 out of 15). Mean results on the 15 slices where spontaneous SWO were investigated indicate that spontaneous SWOs lost on average more than 50% of their initial energy (51.2 ± 34 % S.D.) over distances as short as 1.5 mm when propagated by EM effects without synaptic connectivity. Averaging across repetitions was necessary to minimize the impact of the spontaneous activity on the side where we assumed that time-locked events were uniquely determined by EM propagation. In the next sections, we resorted to evoked rather than spontaneous Up states for these reasons.

Signal distortion and delays characterize the propagation of activity

Triggered events such as Up states induced by local glutamate application (Fig. 2B) or glutamate responses *per se* (Fig. 2C) presented the advantages of providing a well-defined time window allowing to measure larger amplitudes across the cut. Moreover, pharmacological stimulation has advantages over electrical stimulation, since it reduces the risk of contaminating the data with capacitive electrode artifacts.

Local application of glutamate in this preparation has been previously proved to be useful for evoking SWOs in a reliable way (26). The difference between Up states and glutamate responses is that Up states are based on local synaptic reverberation (26, 35) while glutamateresponses are a postsynaptic response of a local neuronal population. Spontaneous epileptiform events induced by addition of the $GABA_A$ blocker bicucullineto the bath led to rather large EM-propagated responses traveling across the cut (Fig. 2D).

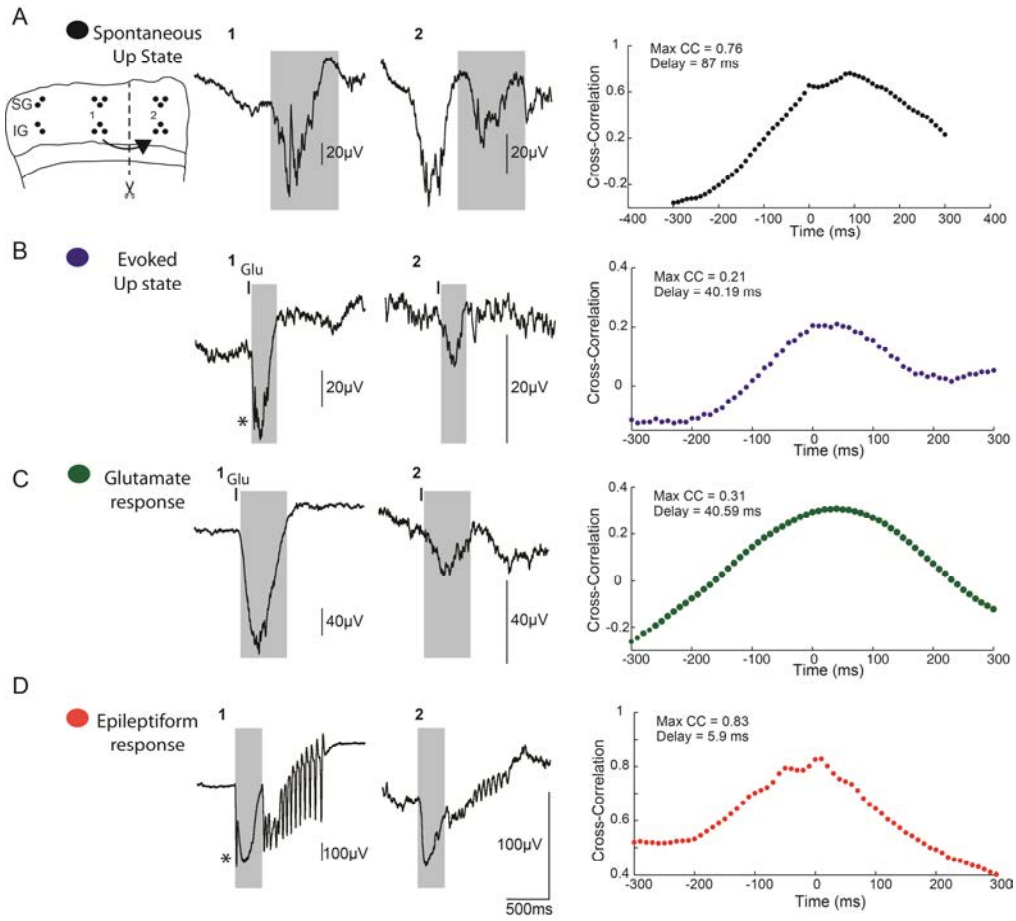

Figure 2. Damping, delays, and distortion characterize the electromagnetic (EM) propagation of both spontaneous and evoked activity.A-D. Four different recording examples of activity originated at position 1 (IG) and its simultaneous EM activity recorded at position 2 (IG). From top to bottom: **A**: spontaneous Up state (black); **B**: Up state evoked with glutamate (blue); **C**: glutamate response (green); **D**: spontaneous (not triggered) epileptiform discharge under 2.4μM bicuculline methiodide bath application. The rightmost panels show the cross-correlations between the voltages at positions 1 and 2 computed over the periods shadowed in A-D: 800ms, 300ms, 550ms, and 320ms, respectively. Asterisk on B and D, fast frequency components. IG, infragranular layer; SG, supragranular layer; CC, cross-correlation.

Damping was a shared property ofall EM-propagated events, independently ofthem being spontaneous or evoked, physiological or epileptiform. For instance, epileptiform discharges occurring by blocking inhibition withbicucullinewere large events (Fig. 2D) that

were well detectable across the cut. Yet, the slow component of epileptiform responses lost on average more than 90% of itsamplitude during propagation across the cut, passing from 500 μV at the site with the largest amplitude to 50 μV at the closest contact across the cut (n=7 events, recorded under $GABA_A$ receptor blockade with bicuculline).

Cross-correlations between the propagated and the original signals never reached their maximum at zero lag; instead, they clearly showed perceptible delays (Fig. 2A-D, rightmost panels). Moreover, the strong filtering of the initial fast frequency components propagating over 1.5 mm is evident from the traces, indicating distortion (asterisks in Fig. 2B and 2D).While the examples illustrated in Figure 2 correspond to the propagation of single events, the presence of delays was systematic across repetitions. The delays estimated from the mean cross-correlations (250 ms after event onset) over the seven slices where propagation of epileptiform events was investigated (more than 191 events) were on average 28.5 ± 20ms (i.e. 52 mm/s). Mean cross-correlation values of the seven slices were relatively low (mean max CC = 0.33±26), suggesting that propagated signals were distorted versions of the original epileptiform signal.

Ruling out potential confounds between synaptic and EM propagation

In Figure 3A we illustrate four examples of EM propagation of mean glutamate-induced responses (black traces with asterisk)and their respective EM propagation across the cut (red traces). Even though the responses are obviously damped across the cut, when expanded, the shape of the responses can be observed (Fig. 3A, center).Glutamate-induced responses and their EM-propagated signals across the cut were different depending on the site where they had been generated (Fig. 3A), illustrating the asymmetries present across cortical layers and suggesting an impact of the local cortical structure on the EM propagation.

EM propagation across the cut was sometimes large enough to recruit the local neuronal population and eventually generate enough local reverberation, resulting into a full-blown Up state (e.g. Fig. 3B1). This is interesting in itself since it illustrates an interaction between EM and synaptic propagation that probably takes place physiologically. However, to properly quantify EM propagation, we need to separateEMfromsynaptic propagation. To do this, we locally applied 30 μM TTX to the recording area on one side ofthe cut (n=7 slices; Fig. 3C, green). By doing this, we ensured that the observed response in this location strictly corresponded to the EM-transmitted signal given that TTX blocks synaptic transmission. We then evaluated the impact of TTX application on the EM-propagated response across the cut, specifically, the impact on its amplitude as well as on any existing delays or distortions.

Damping and delays in the propagated signals before (Fig. 3B) and after (Fig. 3C) blocking the activity of local networks by TTX were comparable. TTX abolished spontaneous oscillations and multiunit activity in the channels surrounding its application (Fig. 3C, green) but it did not abolish the mean glutamate response significantly different from zero ($p=3e-4$, t-test) on the other side of the cut (Fig. 3C, gray). Response timing and amplitudes were assessed before and after TTX in the 2 s following the release of glutamate. TTX application did not change the main negative component of the EM-propagated response (response peak) (mean $p=0.21$, t-test). The cross-correlations between the mean responses before and after TTX were highly significant (mean 0.91 ± 0.6, $n=7$, $p=2.5e-5$) and peaked at zero lag. These findings suggest that the neural response evoked by glutamate propagated across the cut even though synaptic propagation was blocked, thus resulting in an EM-propagated signal.

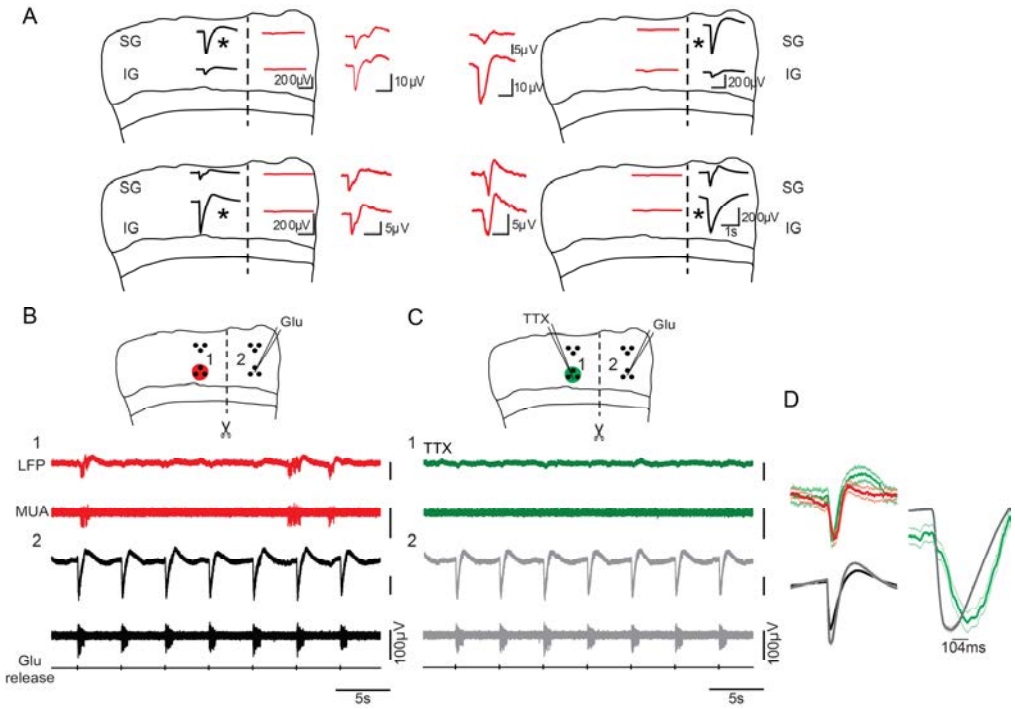

Figure 3. Distortion and propagation delays measured on averaged responses are not due to synaptic delays. A. Black traces depict the mean responses evoked by periodic releases of glutamate (n=130) at different positions within the slice (indicated by an asterisk). Red traces show the mean responses computed after EM propagation across the cut;expanded vertical scale outside the slice schemes. **B**. Raw LFP (top traces) and MultiUnit activity (MUA, bottom traces) recorded at IG layers on both sides of the cut (contact 1 and 2) in response to glutamate release every 4 s on the right part (black). **C**. Local application of TTX at contact 1 blocking synaptic activity (spontaneous SWO, green), but not glutamate responses (gray). **D**. (Left) Superposition of the mean responses (standard errors overlaid) to glutamate before (red) and after (green) blocking synaptic transmission with TTX at contact 1 and across the cut at contact 2, before (black) and after(gray) TTX. (Right) Peak to peak delays are seen between contacts 1 and 2 after TTX.Abbreviations as in Fig. 2.

The mean response of the non-stimulated side of the cut was similarly damped before and after TTX application (Fig. 3D). In this particular example, damping was accompanied by a delay of the propagated signal by 104 ms (Fig. 3D, right). Overall, signal delays between the stimulated site and the closest contacts on the other side of the cut before and after TTX were nearly identical (mean delay=92.2 ±17ms before TTX and mean delay=96.4±23ms

after TTX, p=0.23, t-test). Such similarities in peak to peak delays before and after TTX rule out synaptic conduction delays as a potential explanation for the low propagation speed of the EM effects on cortical tissue. In the shown example (Fig. 3D, right), the speed at which the envelope of the signal propagated over the 1.5mm separating both contacts resultedin a modest value of 14 mm/s. This speed is more than five orders of magnitude lower than the one estimated (equation 12) from available dielectric parameters (12) for 10 Hz (~200000 mm/s) but similar to the speed at which SWO typically propagate under intact synaptic connectivity (26).

Distortion and delays characterize EM propagation

Local application of glutamate evokes neural activity generated by the postsynaptic activation of glutamate receptors plus the subsequent recruitment of local networks. Predicting the potential patterns to be measured at a source-free location (e.g., the non-stimulated side of the slice) as a function of all potentials recorded in the stimulated site would require knowing: 1) the currents arising everywhere, 2) the local geometry and 3) dielectric parameters below 10 Hz (36). However, as illustrated in Figures 4 and 5, the mean responses to glutamate, on which we based estimates of distortion and speed given next, tended to be very local to the stimulated triode with amplitudes quickly decaying at contacts potentially connected to the stimulated site (Fig. 4B, bottom row, and Fig. 5B top row). Therefore, responses estimated at electrodes on the other side of the cut were dominated by the responses at the stimulated contacts. In cases like this one, with a relatively simple spatial pattern of potentials, delays and distortions were still observed (Fig. 5B), suggesting that they progressively appearedbecause ofEM propagation in a dispersive tissue.Similarly, during the propagation of epileptiform events spontaneously generated in the left sectionof the cut, all electrodes on the left side showed the initial fast component that was missing on the right side of the cut.

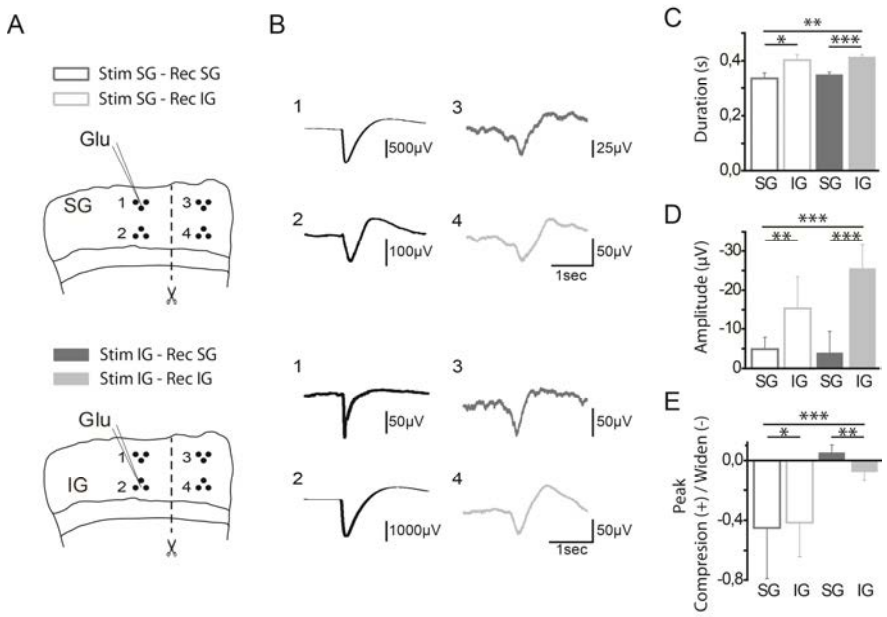

Figure 4. Damping, Compression, and Widening of the EM propagated responses in 12 slices. A. Scheme showing the spatial distribution of channels and the corresponding cortical layers stimulated by local application of glutamate. **B.**Event-triggered average waveforms obtained from 102 repetitions of glutamate application to the location indicated in A. The location of the recordings is indicated by the number. **C, D, and E** illustrate population statistics of the damping and distortions of the EM-propagated waves. Statistics were computed from the fitting of event-triggered average peaks using a minimum of 50 repetitions to compute each average. Population statistics (Mean & Standard Error) summarize results from 64 releases of glutamate at one of the triodes/diodes on 12 different slices. *p<=0.05, **p<=0.01, ***p<=0.001 using t-test or Mann–Whitney U test. Stim (stimulation), Rec (recording electrode), 1-4 (electrode position for each recording), Hollow/full bars correspond to the application of glutamate at SG/IG, respectively. Dark/light gray, SG/IG recording, respectively.Other abbreviations as in Fig. 2.

We also investigated if the presence of the cut played a major role in the observed delays and distortions. To do so, we blocked synaptic transmission on the leftmost pairs of electrodes (diodes) in five slices by locally applying TTX over them. This allowed us to explore how the responses to glutamate locally applied to the contacts in the middle of the slice propagated to a pharmacologically "synaptic-disconnected" rather than to a

physically “synaptic-disconnected” tissue. Delays and distortion during EM propagation to TTX-blocked areas (not shown) were like those observed in the presence of the cut, indicating that the artificial interface created by the cut was not the main source of delays and distortion.

Propagation of glutamate-evoked slow waves as a function of local microstructure

Cortical microstructures are expected to play a major role in shaping LFP propagation (37). We, therefore, evaluated if and how different parameters of the glutamate-evoked mean propagated peaks (duration, amplitude, peak compression/widening and propagation speed) varied as a function of both the stimulated and the recorded cortical layers (Fig. 4 and 5). The plots summarize results of 62 cases, with each case defined as the release of glutamate at a given triode (12 slices/6 triodes, 10out of 72 cases were discarded because peak fitting errors were above 10%). Only sites not synaptically connected to the stimulated site are summarized in the statistics. The responses were divided according to the layer where the electrode recording the EM-propagated response was positioned and the layer where the glutamate was released (Fig.4A,B, and 5A,B).

We observed significant differences in the EM propagation as a function of the layer. In comparison to contacts within infragranular layers, those at supragranular layers showed significantly narrower (Fig.4B,C, $p<0.01$, t-test) and smaller peaks ($p<0.01$, t-test) upon both supragranular and infragranular stimulation. We quantified distortion using a measure of the peak widening/compression (Fig. 4E) that provided information specific to the nature of the distortion, positive values indicating compression and negative values indicating widening(see Materials and Methods). Overall, we observed that distortion was sensitive to the positions of the source (stimulated site) with respect to the receiver; andhighlysensitive to the layers traversed by the signals during their propagation.

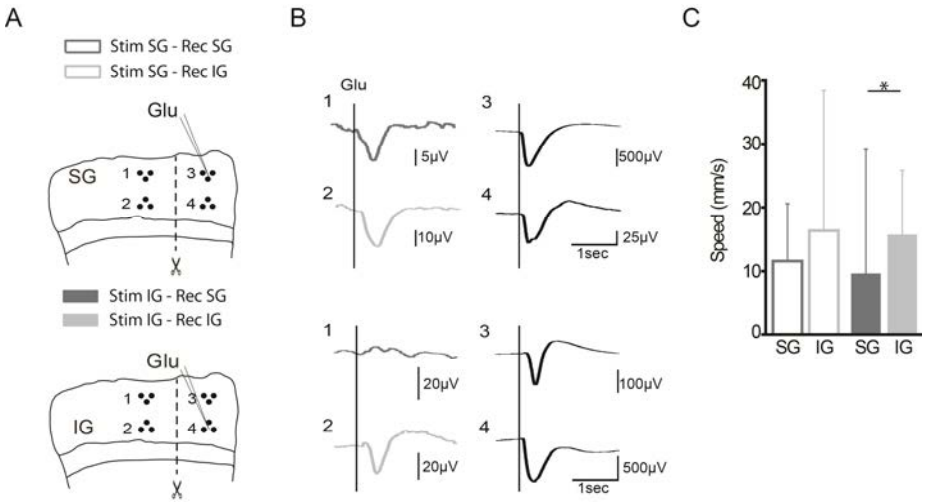

Figure 5. EM propagation speeds of glutamate responses are too slow to justify the quasistatic approximation (QSA).A-B. Same as figure 4A-B. In this case, the onset of the glutamate application is depicted. **C**. Mean EM propagation speeds computed as a function of the stimulated layer (Stim). Electrodes such as 1 in the bottom plot in B where no significant responses above/below baseline were detected (t-test)were excluded. Speed was computed as the difference in latency between the peak fitted to the stimulated site and the IG and SG sites on the other side of thecut divided by the distance between the stimulated electrodes. Abbreviations as in Fig. 2 and Fig. 4 (*$p<0.05$ using t-test).

Application of glutamate to supragranular layers (Fig. 4E) led to significant peak widening recorded in infragranular layers ($p=0.046$, U-test). On the contrary, application of glutamate to infragranular stimulation led peak compression ($p=0.0002$, U-test) while propagating across the columns to supragranular layers (Fig. 4E). In short, signal distortion (peak widening/compression) was overall less severe when glutamate responses propagated from supra to infragranular layers than when traveling from infra to supragranular layers. The similar deformation of the responses between intact synaptic connectivity and absent connectivity suggests a role for cortical microstructure in shaping LFP responses.

Regarding propagation speed, the horizontal propagation speed was relatively stable across layers since no significant differences were observed as a function of the stimulated

site (p=0.13, U-test) (Fig. 5). Propagation speeds were slightly faster when EM signals propagated through infragranular layers (Fig. 5C). EM propagation speed was significantly slower than propagation speed under intact synaptic connectivity (Mean intact connectivity: 13.6 ± 2.70 SD mm/s, Mean EM: 18.3 ± 2.85 SD; p=0.0006, Mann-Whitney U-test).

Discussion

In this study,we found that electromagnetic propagation of SWO and epileptiform activity cannot be explained by the QSA.For this, we experimentally assessed the main assumptions underlying macroscopic models currently in use in the neuroscience literature (assumptions 1 and 2 in the theoretical section of the Methods) to describe the propagation of LFP and EEG/MEG signals in cortical tissue. It is often assumed that neural tissue behaves as an homogeneous ohmic conductor (i.e., neurons, membranes and extracellular space taken as mixed into a continuous model characterized by a frequency-independent unique conductivity value). In this model, signals with different frequency content propagate without distortion and at infinite speeds from the sources to the sensors. This assumption seems at odds with theoretical predictions for good conductors (see equation 12) or with recent measurements of the dielectric properties (3, 21), which attribute large permittivity values and strongly dispersive properties to neural tissue within the electrophysiological range of interest in agreement with the theory (equations 11 and 12). Experimental evidence against low-frequency dispersion was later provided by an in vivo study from Logothetis *et al.*(13), although results from Gomes et al. (18) which considered the low-frequency range under 10 Hz seem to contradict this finding. Directly estimating dielectric properties is particularly problematic within the low-frequency band where the parasitic polarization effects at the interface between tissue and electrodes seriously decrease the reliability of the estimates (20, 36), even if the four-electrode system is used (20). These effects are particularly acute during electrical stimulation.

To partially overcome these limitations, we investigated here the propagation of signals naturally evoked in neural tissue during physiological (SWOs) or pathological (epileptiform activity) cortical activity. Noteworthy, the use of the term "wave" to refer to SWOs does not refer to the physical concept of electromagnetic waves, but rather to the neuroscience concept of wave cycle of neural oscillations. We searched for unequivocal signs of low-frequency dispersion (signal distortion and delays) using pharmacological manipulations and recording settings aimed at minimizing artifactual contributions from the electrode-tissue interface. To isolate synaptic transmission (also responsible for signal delays) from electromagnetic (which we call here electromagnetic—EM) propagation, we performed a complete section of the cortical slice perpendicular to the cortical layers while ensuring that both sides of the cut remained in contact.

In agreement with previous studies (18), we observed important deviations from predictions of the non-dispersive quasistatic approximation (QSA), which is often used to model the propagation of low-frequency SWO from intracranial, LFP and scalp (EEG/MEG) recordings. Instead of the expected undistorted and nearly instantaneous propagation predicted by the Poisson equation, SWOs underwent considerable distortion and delays during their propagation across the interrupted cortical tissue. Non-synaptic propagation speeds were strikingly low, approaching the values at which slow waves travel under intact horizontal synaptic connections (26, 38-40). Our estimated EM mean propagation speeds (~18mm/s) were, however, closer to the propagation speeds (~100mm/s) reported in hippocampal tissue (17) during the electric propagation of epileptiform activity than to quasistatic predictions. The large delays and the fact that our conclusions are based on comparing unfiltered signals within the same frequency band using the same instrumentation (23) makes it unlikely that electrode polarization was the source of the distortions.

Propagation speeds between non-synaptically connected areas were too slow to justify the QSA if cortical tissue were to be considered homogeneous. If there should be any difference because of the cut, this would be that any remaining space with no contact should be filled with the artificial cerebrospinal fluid (ACSF) in which the slice was immersed. Contact with ACSF would provide a more conductive interface forthe propagating waves, which would better mimic the purely resistive (ohmic) volume conductor model. Moreover, the comparison of the delays and distortions between symmetric contacts at both sides of the cut upon blockade of synaptic transmission by TTX on intact tissue revealed no differences, suggesting the little impact of the cut on the observed delays and distortions.

Our obtained mean propagation speeds (~18mm/s) are six orders of magnitude lower than the speed predicted by dielectric estimates in Gabriel's database (using equations 11 and 12) and well below the instantaneous propagation speed assumed by the QSA. These very low propagation speeds for low frequencies are, as discussed in theMethods (*1. Theory*), in agreement with propagation speeds in excellent conductors and with the small but non-zero penetration (skin) depths (see Eq. 12) that can be attributed to ionic diffusion (41). Indeed, the strong absorption (damping) of the EM-propagated slow wave accompanied by signal distortions and delays that we observed is not a surprising but instead a well-characterized property of heterogeneous ionic conductors (25, 42) and a predictable consequence of the causality principle (2, 24).

Most macroscopic models of the EEG/MEG and the LFP signal aim to characterize a highly heterogeneous tissue using dielectric properties that assume that the material is homogeneous. The cortical tissue is highly heterogeneous and consists of domains of different phases and materials (e.g., capacitive membranes alternating with conductive electrolytes as in the extracellular space). The tissue is then heterogeneous at a 'microscopic' scale. While, under such circumstances, the heterogeneous material can be

viewed as a continuum on the microscopic scale and can be ascribed macroscopic or 'effective' properties (42), a proper theoretical formalism to do so is currently lacking. It is however known from dielectric spectroscopy studies in heterogeneous media (42) that water membrane heterogeneity exhibits a typical dispersive dielectric behavior characterized by 1) a power law dependence of the effective electric conductivity at low frequencies (called alpha dispersion), often ascribed to the longitudinal and tangential diffusion of ions in the electrical double layer that surrounds charged membranes (43), and 2) large effective permittivity values at very low frequencies that are seen when interfaces with aqueous ionic substances are involved (44). Consequently, the large permittivity values reported by Gabriel (1996) and confirmed in vivo by Wagner (22)and the dispersion effects are neither unique to animal tissue nor necessarily artefactual in origin. Instead, they are more likely a general property of the microstructure of heterogeneous materials with ionic conduction and aqueous interfaces (45, 46). In support of this view, detailed LFP models (47) that restrict the QSA to the extracellular space in a purely ohmic medium, while incorporating neuronal geometries and membrane capacitances into the cable model, can reproduce signal delays and distortion comparable to ours (although see (48)). According to previous simulations that use a synaptic current as input and a non-quasistatic modeling framework (cable equation), delays and distortion are due to the intrinsic-dendritic filtering effect and therefore to tissue heterogeneities (Torbjørn V Ness, Gaute Einenvoll, personal communication).

The modeling and simulation studies from Bedard et al. (49) or Lindén et al. (47) link the heterogeneous microstructure of neural tissue with its filtering properties. As shown by Bedard et al. (48), spatial gradients in the conductivity and permittivity induced by neural microstructures results in the filtering of the high-frequency components of the extracellular signals with distance. As previously discussed, filtering of some components should result in phase shifts and delays of other components, hence leading to signal

delays and distortion. Therefore,our observations of distortion and delays seem in line with previous modeling studies specific to neural tissue (47, 49), being in agreement with the causality principle and likely reflectinga universal property inherent to highly heterogeneous materials (42). These effects cannot be accountedfor within the homogeneous quasistatic modeling framework currently in use in many macroscopic models.

The experimental findings of the current study are compatible with the necessity to rely on dispersive models (i.e., frequency varying dielectric properties) to build homogeneous macroscopic models of cortical tissue. We describe the propagation of the electromagnetic fields in a homogenized macroscopic model of neural tissue using effective parameters (permittivity and conductivity), a situation in which there are no divisions between cell membranes and extracellular space. As shown in the theoretical section, dispersion is a property inherent to conductors rather than capacitors (dielectrics). Consequently, the dispersive properties of neural tissue cannot be solely ascribed tothe capacitive properties of the neuron membrane which is typically considered as frequency independent. The microscopic origin of these dispersive properties within the low-frequency range is probably influenced by multiple physical and physicochemical effects including transport or ionic diffusion and polarization phenomena (37, 50, 51). Unfortunately, appropriate models able to describe the universality of ionic conduction laws in disordered materials (52) in the presence of aqueous charged interfaces are still absent. Currently, theoretical models attribute low-frequency dispersion (below 1kHz) to the longitudinal and tangential diffusion of ions within the electrical double layer that surrounds charged particles or membranes (43). Ionic diffusion is one of the likely microscopic mechanisms that can explain low propagation speeds and distortion (18), thereby leading to a distribution of relaxation times and therefore to frequency-dependent dielectric parameters (dispersion). Furthermore, since our cut slices are in

contact, we cannot rule out certain contribution of ionic diffusion e.g. potassium ions traveling across the cut, to the described phenomena. However, further investigation on the microscopic mechanisms underlying dispersion is required since alternative mechanisms to ionic diffusion have been proposed(14, 50).

Overall, the observation of delays and distortions during the propagation of physiological signals bears implications for the modeling, analysis, and interpretation of the LFP, intracranial data or scalp-recorded EEG/MEG signals. The approach taken in this study to investigate capacitive effects and dispersion for frequencies below 10 Hz (18, 22) is unable to provide concrete estimates for the permittivity and conductivity needed to build detailed macroscopic models. Therefore, it is not possible to fully appreciate the magnitude of errors incurred by quasistatic ohmic considerations. However, the studies by Wagner (22) or Butson and McIntyre (53), which evaluated the importance of including capacitive effects (permittivity) within models for transcranial magnetic stimulation (TMS) or deep brain stimulation (DBS) models, detected substantial differences.

While Butner or Wagner and McIntyre ignored dispersion, our results confined to the extremelylow-frequency range below 10Hz are not necessarily relevant for DBS, which typically relies on higher frequencies. However, the situation is different for TMS or scalp/intracranial EEG models. In light of our study, modeling errors are to be expected as well for head models used in electrical neuroimaging and particularly for those aimed at localizing epileptic activity or SWOs given their frequency content below 10Hz.

Although a full quantitative assessment of the errors needs to await for more reliable dielectric data, we can already anticipate some of methodological and clinical approaches that might be impacted by our results. First, the fact that EMpropagationis delayed and signals are distorted bears consequences on the qualitative assessment of electrophysiological data. For instance, scalp measured epileptic spikes or slow waves are

not necessarily the instantaneous reflect of their intracerebral sources but might indeed reflect generators acting a few milliseconds before. Consequently, epileptic source localization needs to account for a temporal window preceding the scalp event to identify betterthe epileptic focus. Second, delays between intracranially recorded events cannot be anymore readily interpreted as neuronal transmission delays between circuit elements. Third, causality or connectivity studies based on spectral features derived from LFPs, intracranial recordings or scalp EEG signals should probably need to account for the strong variation in frequency filtering properties of brain tissue that translates into delays and eventual phase reversals of the propagated signals. At a certain distance from the source generating the pulse, these combined effects (selective frequency filtering and phase changes) might be wrongly interpreted as interrelationships between the phase and the power of different oscillations or as some rhythms causally driving others. Fourth, we observed phase reversals between contacts that were not synaptically connected in the absence of any underlying source/sink. Therefore, the possibility that phase changes or reversals arise from cortical microstructures (e.g., dendritic filtering or extracellular impedances), rather than from current sources and sinks, needs to be considered in cases where the goal is to localize the epileptic focus. In fact, with dispersion, a direct relationship between the Current Source Density (CSD) and the Laplacian of the measured potential cannot be anymore guaranteed, and new approaches to CSD estimation are thus required (7).

Author Contributions:

SLGA, MVSV, BR and RGPM designed the study and wrote the paper. BR and MVSV performed the experiments. RGPM, SLGA, and BR contributed analytic tools and analyzed data. XV contributed analytic tools.

Acknowledgements:

SLGA and RGPM weresupported by the 3R Research Foundation Grant 119-10. The experimental work was funded by Spanish Ministerio de Ciencia e Innovación (BFU2014-52467-R) and by PCIN-2015-162-C02-01 (FLAG-ERA) and WaveScales #604102 (Human Brain Project) to MVSV. BR had an FPI fellowship from the Spanish Ministerio de Ciencia e Innovación. SAF2012-40227- C02-02, and IPT-2012-0438-010000 from Spanish Ministry of Economy and Competitiveness and the European Regional Development Fund.

References

1. Plonsey, R., and D. B. Heppner. 1967. Considerations of quasi-stationarity in electrophysiological systems. Bull Math Biophys 29:657-664.

2. Yuffa, A. J., and J. A. Scales. 2012. Linear response laws and causality in electromagnetics. Eur J Phys 33:1635-1650.

3. Wagner, T., A. Valero-Cabre, and A. Pascual-Leone. 2007. Noninvasive Human Brain Stimulation. Annual Review of Biomedical Engineering 9:527-565.

4. Bossetti, C. A., M. J. Birdno, and W. M. Grill. 2008. Analysis of the quasi-static approximation for calculating potentials generated by neural stimulation. Journal of Neural Engineering 5:44-53.

5. Grave de Peralta Menendez, R., M. M. Murray, C. M. Michel, R. Martuzzi, and S. L. Gonzalez Andino. 2004. Electrical neuroimaging based on biophysical constraints. NeuroImage 21:527-539.

6. Nicholson, C., and J. A. Freeman. 1975. Theory of current source-density analysis and determination of conductivity tensor for anuran cerebellum. Journal of Neurophysiology 38:356-368.

7. Bédard, C., and A. Destexhe. 2011. Generalized theory for current-source-density analysis in brain tissue. Physical Review E 84:041909.

8. Buzsaki, G. 2004. Large-scale recording of neuronal ensembles. Nat Neurosci 7:446-451.

9. Bedard, C., and A. Destexhe. 2009. Macroscopic models of local field potentials and the apparent 1/f noise in brain activity. Biophys J 96:2589-2603.

10. Bazhenov, M., P. Lonjers, S. Skorheim, C. Bedard, and A. Dstexhe. 2011. Non-homogeneous extracellular resistivity affects the current-source density profiles of up-down state oscillations. Philos Trans A Math Phys Eng Sci 369:3802-3819.

11. Gabriel, S., R. W. Lau, and C. Gabriel. 1996. The dielectric properties of biological tissues: II. Measurements in the frequency range 10 Hz to 20 GHz. Physics in Medicine and Biology 41:2251-2269.

12. Gabriel, S., Lau, R.W. , Gabriel, C. . 1996. The dielectric properties of biological tissues: III. Parametric models for the dielectric spectrum of tissues. Phys. Med. Biol. 41:2271-2293.

13. Logothetis, N. K., C. Kayser, and A. Oeltermann. 2007. In vivo measurement of cortical impedance spectrum in monkeys: implications for signal propagation. Neuron 55:809-823.

14. Jonscher, A. K. 1995. An electrochemical model of low-frequency dispersion. J Mater Sci 30:2491-2495.

15. Ngai, K. L., A. K. Jonscher, and C. T. White. 1979. On the origin of the universal dielectric response in condensed matter. Nature 277:185-189.

16. Dissado, L. A., and R. M. Hill. 1984. Anomalous low-frequency dispersion. Near direct current conductivity in disordered low-dimensional materials. Journal of the Chemical Society, Faraday Transactions 2: Molecular and Chemical Physics 80:291-319.

17. Zhang, M., T. P. Ladas, C. Qiu, R. S. Shivacharan, L. E. Gonzalez-Reyes, and D. M. Durand. 2014. Propagation of Epileptiform Activity Can Be Independent of Synaptic Transmission, Gap Junctions, or Diffusion and Is Consistent with Electrical Field Transmission. The Journal of Neuroscience 34:1409-1419.

18. Gomes, J.-M., C. Bédard, S. Valtcheva, M. Nelson, V. Khokhlova, P. Pouget, L. Venance, T. Bal, and A. Destexhe. 2016. Intracellular Impedance Measurements Reveal Non-ohmic Properties of the Extracellular Medium around Neurons. Biophysical Journal 110:234-246.

19. Feldman, Y., A. Puzenko, and Y. Ryabov. 2005. Dielectric Relaxation Phenomena in Complex Materials. In Fractals, Diffusion, and Relaxation in Disordered Complex Systems. John Wiley & Sons, Inc. 1-125.

20. Sverre, G., and G. M. Ørjan. 2007. Sources of error in tetrapolar impedance measurements on biomaterials and other ionic conductors. Journal of Physics D: Applied Physics 40:9.

21. Gabriel, S., Lau, R.W., Gabriel, C. 1996. The dielectric properties of biological tissues: II. Measurements in the frequency range 10 Hz to 20 GHz. Phys. Med. Biol. 41:2251-2269.

22. Wagner, T., U. Eden, J. Rushmore, C. J. Russo, L. Dipietro, F. Fregni, S. Simon, S. Rotman, N. B. Pitskel, C. Ramos-Estebanez, A. Pascual-Leone, A. J. Grodzinsky, M. Zahn, and A. Valero-Cabre. 2014. Impact of brain tissue filtering on neurostimulation fields: a modeling study. NeuroImage 85:1048-1057.

23. Nelson, M. J., P. Pouget, E. A. Nilsen, C. D. Patten, and J. D. Schall. 2008. Review of signal distortion through metal microelectrode recording circuits and filters. J Neurosci Methods 169:141-157.

24. Toll, J. S. 1956. Causality and the Dispersion Relation - Logical Foundations. Phys Rev 104:1760-1770.

25. Jonscher, A. K., C. LÉOn, and J. Santamaria. 1998. Dynamic transport in ionic conductors. J Mater Sci 33:4485-4490.

26. Sanchez-Vives, M. V., and D. A. McCormick. 2000. Cellular and network mechanisms of recurrent rhythmic activity in neocortex. Nat Neurosci 3:1027-1034.

27. Steriade, M. 1993. Sleep oscillations in corticothalamic neuronal networks and their development into self-sustained paroxysmal activity. Rom J Neurol Psychiatry 31:151-161.

28. Grave de Peralta Menendez, R., and S. Gonzalez Andino. 2015. Electrical Neuroimaging with Irrotational Sources. Computational and Mathematical Methods in Medicine 2015:801037.

29. Ida, N. 2004. Engineering electromagnetics. Springer, Berlin.

30. Reimann, Michael W., Costas A. Anastassiou, R. Perin, S. L. Hill, H. Markram, and C. Koch. 2013. A Biophysically Detailed Model of Neocortical Local Field Potentials Predicts the Critical Role of Active Membrane Currents. Neuron 79:375-390.

31. Someda, C. G. 2006. Plane waves in isotropic media. In Electromagnetic Waves, Second Edition. CRC Press. 89-131.

32. Sanchez-Vives, M. V. 2012. Spontaneous rhythmic activity in the adult cerebral cortex in vitro. In Isolated Central Nervous System Circuits. H. Press, editor. 263-284.

33. Amzica, F., and M. Massimini. 2002. Glial and Neuronal Interactions during Slow Wave and Paroxysmal Activities in the Neocortex. Cerebral Cortex 12:1101-1113.

34. Lilliefors, H. W. 1967. On the Komogorov-Smirnov test for normality with mean and variance unknown. Journal of the American Statistical Association 62:399-402.

35. Compte, A., R. Reig, V. F. Descalzo, M. A. Harvey, G. D. Puccini, and M. V. Sanchez-Vives. 2008. Spontaneous high-frequency (10-80 Hz) oscillations during up states in the cerebral cortex in vitro. J Neurosci 28:13828-13844.

36. Gabriel, C., Peyman, A., Grant, E.H 1. 2009. Electrical conductivity of tissue at frequencies below 1 MHz. Phys. Med. Biol. 54 54:4863–4878.

37. Barsoukov, E., MacDonald, J.R. . 2005. Impedance Spectroscopy: Theory, Experiment, and Applications, 2nd Edition. Wiley, New York.

38. Massimini, M., Huber, R., Ferrarelli, F., Hill, S., Tononi, G. . 2004. The sleep slow oscillation as a traveling wave The Journal of Neuroscience 24:6862-6870.

.

39. Ruiz-Mejias, M., Ciria-Suarez, L., Mattia, M., & Sanchez-Vives, M. V. . 2011. Slow and fast rhythms generated in the cerebral cortex of the anesthetized mouse. Journal of Neurophysiology 106:2910-2921.

40. Stroh, A., H. Adelsberger, A. Groh, C. Rühlmann, S. Fischer, A. Schierloh, K. Deisseroth, and A. Konnerth. 2013. Making Waves: Initiation and Propagation of Corticothalamic Ca2+ Waves In Vivo. Neuron 77:1136-1150.

41. Hirose, A., Lonngren, K.E. 1995. Introduction to Wave Phenomena. Wiley Interscience, New York.

42. Torquato, S. 2002. Random heterogeneous materials : microstructure and macroscopic properties. Springer, New York.

43. Chew, W. C. 1984. Dielectric enhancement and electrophoresis due to an electrochemical double layer: A uniform approximation. The Journal of Chemical Physics 80:4541-4552.

44. Chelidze, T. L., Gueguen, Y. 1999. Electrical spectroscopy of porous rocks: a review.-I. Theoretical models. Geophys. J. Int 137:1-15.

45. Bedard, C., Destexhe, A 2012. Modeling local field potentials and their interaction with the extracellular medium. In Handbook of Neural Activity Measurement. R. Brette, Destexhe, A, editor. Cambridge University Press, Cambridge. 136-191.

46. Martinsen, O. G. G., S.; Schwan, H. P. 2002. Interface phenomena and dielectric properties of biological tissue. . In Encyclopedia of Surface and Colloid Science. A. T. Hubbard, editor. Taylor & Francis, CRC Press. 2643-2652.

47. Lindén, H., E. Hagen, S. Leski, E. S. Norheim, K. H. Pettersen, and G. T. Einevoll. 2014. LFPy: A tool for biophysical simulation of extracellular potentials generated by detailed model neurons. Frontiers in Neuroinformatics 7.

48. Bedard, C., S. Rodrigues, N. Roy, D. Contreras, and A. Destexhe. 2010. Evidence for frequency-dependent extracellular impedance from the transfer function between extracellular and intracellular potentials: intracellular-LFP transfer function. J Comput Neurosci 29:389-403.

49. Bedard, C., H. Kroger, and A. Destexhe. 2004. Modeling extracellular field potentials and the frequency-filtering properties of extracellular space. Biophys J 86:1829-1842.

50. Klösgen, B., C. Rümenapp, and B. Gleich. 2011. Bioimpedance Spectroscopy. In BetaSys: Systems Biology of Regulated Exocytosis in Pancreatic ß-Cells. B. Booß-Bavnbek, B. Klösgen, J. Larsen, F. Pociot, and E. Renström, editors. Springer New York, New York, NY. 241-271.

51. Martinsen, Ø. G., Grimnes, S., Schwan, H.P.:. 2002. Interface phenomena and dielectric properties of biological tissue. In Encyclopedia of Surface and Colloid Science. 2643-2652.

52. Dyre, J. C., and T. B. Schrøder. 2000. Universality of ac conduction in disordered solids. Reviews of Modern Physics 72:873-892.

53. Butson, C. R., and C. C. McIntyre. 2005. Tissue and electrode capacitance reduce neural activation volumes during deep brain stimulation. Clinical neurophysiology : official journal of the International Federation of Clinical Neurophysiology 116:10.1016/j.clinph.2005.1006.1023.

54. Fröhlich, F., and D. A. McCormick. 2010. Endogenous electric fields may guide neocortical network activity. Neuron. 67:129-143.